Sascha Ranftl, BSc

Ultrafast Photoinduced Ejection Dynamics of Indium Atoms inside Superfluid Helium Nanodroplets

MASTER'S THESIS

to achieve the university degree of

Diplom-Ingenieur

Master's degree programme: Technical Physics

submitted to

Graz University of Technology

Supervisor

Ass.-Prof. Dipl.-Ing. Dr.techn. Markus Koch

Institute for Experimental Physics

Graz, November 2017

EIDESSTATTLICHE ERKLÄRUNG

AFFIDAVIT

Ich erkläre an Eides statt, dass ich die vorliegende Arbeit selbstständig verfasst, andere als die angegebenen Quellen/Hilfsmittel nicht benutzt, und die den benutzten Quellen wörtlich und inhaltlich entnommenen Stellen als solche kenntlich gemacht habe. Das in TUGRAZonline hochgeladene Textdokument ist mit der vorliegenden Masterarbeit/Diplomarbeit/Dissertation identisch.

I declare that I have authored this thesis independently, that I have not used other than the declared sources/resources, and that I have explicitly indicated all material which has been quoted either literally or by content from the sources used. The text document uploaded to TUGRAZonline is identical to the present master's thesis/diploma thesis/doctoral dissertation.

_____ _____

Datum / Date Unterschrift / Signature

Abstract

Photoinduced ultrafast dopant ejection dynamics of indium atoms confined in helium nanodroplets (He_N) have been investigated. In this work, to the author's knowledge, the very first femtosecond time-resolved photoelectron spectra obtained inside doped droplets are presented, providing the proof of principle that femtochemistry inside this cryogenic nano-testbed is possible and thus enabling a rich manifold of experiments to come. Further, a temporal limit for photochemistry experiments in this inert container is determined to be about 50 ps. The element chosen for these fundamental experiments, indium, was shown to exhibit ground states located both in the center and on the surface of the drop.
Helium nanodroplets, containing of a few thousand helium atoms and spanning a few nanometres, are an almost ideal spectroscopic matrix for trapping atoms and molecules in a weakly perturbing, cryogenic and transparent environment. The droplets further facilitate some astonishing properties such as superfluidity, motivating for the commonly used term 'quantum fluid'.
The presented experiments apply time-resolved photoelectron and -ion spectroscopy. A femtosecond pulse exciting higher He_NIn states is followed by a femtosecond ionisation probe pulse, mapping the current state of the system onto the cation continuum, i.e., the electron kinetic energy measured determines the state from which the ionisation took place. Ion detection provides information about molecular fragmentation and formation processes.
Within this work a He_N source, resistively heated doping facilities, a quadrupole mass spectrometer used as a diagnostics tool and an ultrahigh vacuum system have been constructed, assembled and connected to an existing time-of-flight spectrometer. Detailed documentation on the apparatus and characterisations of the setup and the investigated system itself are provided. In the experimental part, the spectral contributions of He_NIn surface and center states as well as He_NIn_2 states are disentangled and dynamics of In atoms are observed and interpreted by means of ion yield and photoelectron spectra. Competing processes of exciplex formation before and after ionisation are suggested, the latter occurring only in a short time window. Existing He_NIn potential energy surfaces are used for a simple molecular dynamics simulation in a purely classical approach. The theory suffices to qualitatively describe the main features of the spectral properties and the dynamic behaviour, but also provides some insight into the state of the system prior to excitation.

Kurzfassung

Es wurden photoinduzierte ultraschnelle Dynamiken von in Helium-Nanotröpfchen (He_N) gefangenen Indiumatomen untersucht. In dieser Arbeit werden, nach bestem Wissen und Gewissen des Autors, die allerersten femtosekundenzeitaufgelösten Photoelektronenspektren aus dem Inneren von dotierten Tropfen präsentiert. Diese liefern den Machbarkeitsbeweis, dass Femtochemie in dieser kryogenen Nano-Testumgebung möglich ist und eröffnen damit eine große Vielfalt an möglichen Experimenten. Weiters wurde auch eine zeitliche Schranke für Photochemie in diesem kryogenen Container auf 50 ps festgelegt. Es ergab sich, dass das Element, welches für diese fundamentalen Experimente ausgewählt wurde, nämlich Indium, Grundzustände sowohl im Inneren als auch auf der Oberfläche des Tropens aufweist.
Helium-Nanotröpfchen bestehen aus mehreren tausend Heliumatomen und sind wenige Nanometer gross. Sie sind eine nahezu ideale spektroskopische Matrix und eine Atom- und Molekülfalle mit einer nur schwach störenden, kryogenen und transparenten Umgebung. Weiters weisen sie erstaunliche Eigenschaften auf wie etwa Supraflüssigkeit, was auch den Begriff "Quantenflüssigkeit" motiviert.
Die vorgestellten Experimente verwenden zeitaufgelöste Photoelektronen- und Photoionenspektroskopie. Ein Femtosekundenpuls regt höhere Zustände an, gefolgt von einem Ionisierungspuls der den momentanen Ensemblezustand auf das kationische Kontinuum abbildet, d.h. die gemessene kinetische Energie der Elektronen legt den Zustand fest aus dem ionisiert wurde. Ionendetektion hingegen gibt Aufschluss über molekulare Fragmentations- und Formationsprozesse.
Im dieser Arbeit wurden eine He_N-Quelle, resistiv geheizte Dotierungsvorrichtungen, ein Quadrupolmassenspektrometer als Diagnostik und ein entsprechendes Ultrahochvakuumsystem aufgebaut, dokumentiert und mit einem bestehenden Flugzeitspektrometer verbunden. Die experimentelle Arbeit umfasst die Entschlüsselung der spektralen Beitrage von Zuständen vom Inneren und von der Oberfläche der Tropfen sowie von Indiumdimeren, weiters die Beobachtung und Interpretation von Dynamiken mit Ionenausbeuten und Photoelektronenspektren. Konkurrierende Prozesse der Exciplexformation vor und nach der Ionisation werden vorgeschlagen, wobei Letzteres nur während eines kurzen Zeitfensters in delikatem Gleichgewicht auftritt. Existierende Potentialenergieflächen von He_NIn wurden für eine einfache Molekulardynamiksimulation mit einem rein klassischen Ansatz benutzt. Die Theorie genügt der qualitativen Beschreibung der Hauptmerkmale der spektralen Eigenschaften und des dynamischen Verhaltens, gibt aber auch Aufschluss über den Zustand des Systems vor der Anregung.

Contents

List of Figures

Listings

List of Tables

Abbreviations & Symbols

ADC	Analog-digital converter
BBO	Barium borate
CB	cross-beam
CH	cold head
CL2	Cluster Lab 2
CP	counter
DFT	density functional theory
DPS	differential pump stage
EP	electrometer
HV	high voltage
IS	ion source of the QMS
IP	ionisation potential
LBE 11/11/2011	Lab book entry on 11/11/2011
MC	main chamber
MCP	micro-channel plate
MD	molecular dynamics
MPI	Multi photo ionisation
OPA	optical parametric amplifier
PDF	probability density function
PE	photoelectrons
PEPICO	photo-electron-photo-ion-coincidence spectroscopy
PES	potential energy surface
PES	photoelectron spectrum
PID	proportional-integral-derivative controller
PP	prevacuum pump
PSU	power supply unit
PU	pickup chamber
QMA	analyser of the QMS
QMC	controller of the QMS
QMG	controller of the QMS
QMH	RF-generator of the QMS
QMS	quadrupole mass spectrometer
RF	radio freguency
SC	source chamber
SEM	secondary electron multiplier

SEV	Sekundärelektronenvervielfacher
SHG	second harmonic (generation)
TC	thermocouple
TDDFT	time-dependent density functional theory
THG	third harmonic (generation)
TOF	time-of-flight spectrometer
TP	turbo pump
VX	valve number X
p_{He}	helium stagnation pressure
T_{CH}	nozzle temperature
T_{PU}	pickup temperature
v_L	Landau velocity

CHAPTER 1

Introduction

1.1 Superfluid Helium nano-droplets

helium nanodroplets (He_N) are a powerful technique for the synthesis of atoms, molecules or clusters, [1, 2] providing an inert, ultracold container with a temperature of 0.37 K [3]. They are a well established tool of spectroscopy as they are transparent up to photon energies of 20 eV [2] and allow to realise a microsolvation environment, bridging from gas phase to solvation in liquids as single or multiple atoms or molecules of different species may be doped in a controlled manner and their interactions, e.g. chemical reactions, studied.
One example is polymers which are fundamental to the advancement of science and technology. Photoexcitation of photoinitiator monomer molecules triggers ultrafast formation of radical states which start a polymerisation chain reaction. The He_N confinement character will allow to identify the intramolecular radical-generating step and the subsequent intermolecular polymerisation reaction. Another example is that fundamental questions about nature arise with the photoprotection mechanism in nucleobase molecules, the constituents of DNA. Ultrafast non-radiative relaxation upon photoexcitation prevents nucleobases from damaging photochemical reactions. Furthermore, the confinement character of the droplets will allow to investigate how these dynamics are affected by co-doping water molecules or even forming complementary base pairs. In 1999 Ahmed Zewail won the Nobel prize [4] for laying the foundations of femtochemistry. In this work, the proof of principle for femtochemistry of single, confined particles is provided.

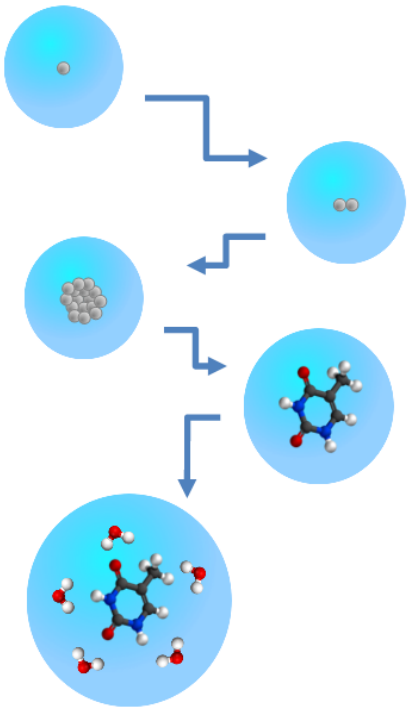

Figure 1.1: Roadmap for He_N as a tool for photo-, cryo- and femtochemistry. With kind permission by Bernhard Thaler.

1.2 Photoinduced dynamics of doped He_N

The ideas presented in this chapter give some insight into photoinduced dynamics of doped He_N for a better understanding of the results presented and discussed in chapters 3 and 4.

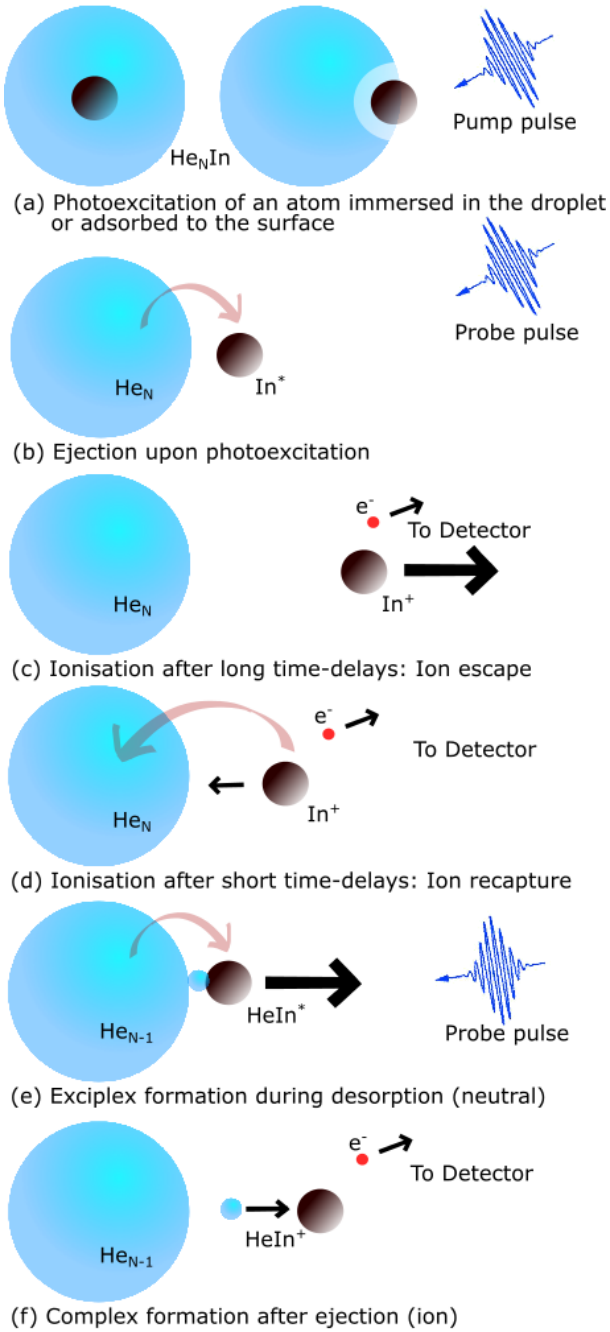

Figure 1.2: Photoinduced dynamics of indium in helium nanodroplets. The processes in (e) and (f) are a mere suggestion and must be verified yet.

While this superfluid environment acts only weakly perturbing on an embedded species in the electronic ground state, [5] it was found to be severe after electronic excitation, leading to either desorption or ejection depending on whether the dopant is confined in the drop at the center or located in a dimple on the surface of the droplet. The latter scenario is a typical behaviour of alkali metal atoms and has been studied intensively this far. [6–10] Quite in contrast positive ions tend to get locked inside the drop due to the strong interaction. [9, 11] On the other hand interactions of helium droplets with transition metal atom range between these two extremes. [12–14] In this work femtosecond time-resolved studies of single indium atoms inside He_N have been carried out to investigate the influence of the quantum solvent on the photoexcitation dynamics and the photoionisation process of dopants located inside He_N . While several experiments in various groups have been devoted to photoexcitation and photoionisation dynamics, time-resolved studies of electronic excitations have been carried out on either bare He_N [15] or on surface located dopants [6, 7, 10]. Some most simple dynamics triggered by photoexcitation and -ionisation are depicted in fig. 1.2. In the ground state the dopants reside in the center of the He_N (a, left) or adsorb to the surface (a, right). The latter case is typical for alkali metals and their dynamics have been investigated so far. In this work it was found that indium exhibits both center and surface ground states. The first pump pulse brings the dopant into a typically repulsive excited state that leads to dopant ejection (b). The probe pulse brings the

dopant into the highly attractive ionic ground state. If the dopant is ionised sufficiently far away from the drop, i.e. long time delays between pump and probe pulses, it remains unbound and can be detected (c). In contrast, if the dopant is ionised in proximity to the droplet, i.e. short time delays between pump and probe pulse, the dopant tends to rebind to the droplet center (d). Apart from these basic ejection and rebinding dynamics, InHe molecules or so-called exciplexes and complexes may form in two different processes. On the one hand, leaving dopants may 'drag' a He atom from the droplet with them on their way out (e), on the other hand ionisation in the small transition regime between ejection (c) and rebinding (d) may cause the leaving dopant to look back and rip out and bind a He atom from the droplet surface (f). These exciplexes and complexes have also been observed with multiple He atoms, i.e. He_nIn molecules.

As traditional absorption spectroscopy cannot cope with the optical densities provided by the droplet beam and induced fluorescence is non-directional, the well established technique of photoelectron spectroscopy (PES) is employed. [16,17] Furthermore this allows to study not only atom but also ionic processes. Although above described dynamics occur on the picosecond time-scale, the response of the droplet itself is expected to happen in the femtosecond time-regime, such as the bubble expansion, i.e. the deformation of the droplet upon the dopant emerging. Because of their 'delayed visibility', one may only make limited conclusions about the atomic motion from sole ion mass spectroscopy. In fig. 1.3 the energy level diagram corresponding to the dopant ejection in fig. 1.2(b-d) shows the various steps in the process. After pumping the He_NIn into the first excited states, the probe identifies the state the ensemble was in at the moment of ionisation, i.e. at different time delays, via the residual kinetic energy of the photoelectrons. Accordingly, two peak shifts in the photoelectron spectra with different time scales are expected, one in the femtosecond regime due to the bubble expansion and the other in the picosecond regime due to the escape of the dopant. Additionally the ionisation potential (IP) is decreased in solvation relative to the free atom.

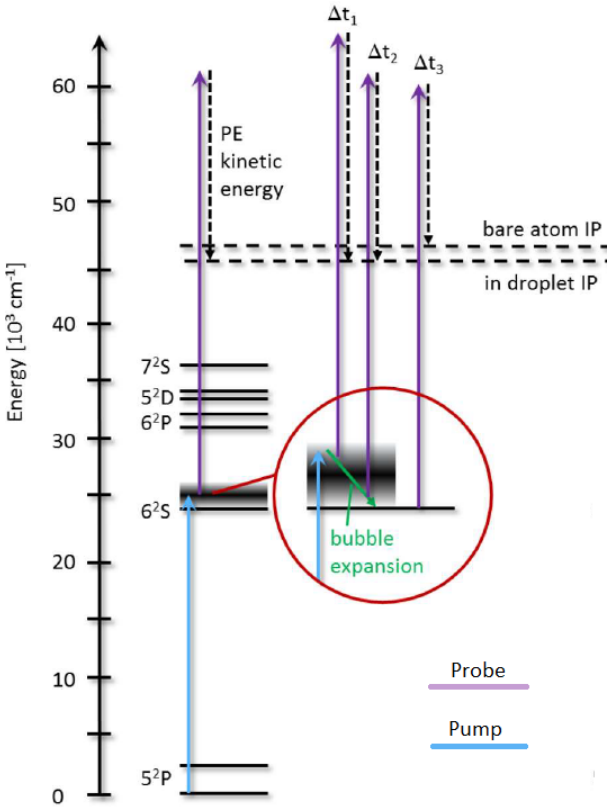

Figure 1.3: Energy level diagram of indium ejection or recapture respectivley in fig. 1.2 (b-d)

In chapter 2, the He_N beam apparatus' construction is documented and characterised with indium and the laser setup. The results are for are presented and discussed in chapter 3. These interpretations are supported by simulations outlined in chapter 4. In chapter 5 encountered experimental issues and open questions are addressed.

CHAPTER 2

Experimental

2.1 Overview

Ultracold He_N droplets are generated in the source chamber (SC) and doped with different atoms or molecules in the pickup chamber (PU). The droplets pass into the main chamber (MC) with a time-of-flight spectrometer (TOF) and are excited and ionised upon crossing the laser beam. The ionisation products are collected and analysed in the TOF. Mounted to the end of the droplets' trajectory is a quadrupole mass spectrometer (QMS), which is used as a diagnostic tool. The PU, QMS and vacuum system will be described in detail within this work in sections 2.3, 2.5 and 2.6. Detailed sketches of the He_N beam apparatus are shown in fig. 2.1 and 2.2. A schematic drawing of the optical setup is shown in fig. 2.3. For detailed descriptions of the optical setup read the Master's theses of Bernhard Thaler [18], Stefan Cesnik [19] and Paul Maierhofer [20]. Documentation of the TOF is provided in those of Paul Maierhofer [20] and Markus Bainschab [21]. Further details regarding the SC and coldhead (CH) can be found in the Dissertation of Markus Koch [22].

A 2-stage-compression procedure, one in the compressor, one in the CH, cools extremely pure (99.9999 %) helium down to a minimum temperature of 10.2 K, which is quite above the helium boiling point of 4 K. For more precise temperature control, a resistive heater is implemented in the nozzle. Upon supersonic expansion of cold high pressure He gas (typically 17 K, 40 bar) through the nozzle ($\varnothing$ 5 μm) superfluid He nanodroplets with a temperature of 0.37 K form. A first aperture at the connection of SC to PU collimates the divergent He_N beam. After passing another aperture the He_N pass through a gas or vapour cloud of the dopant and pick up particles statistically. After passing the aperture of the cooling shield, the beam passes yet another aperture and enters the differential pump stage (DPS). While the apertures are apparently implemented to further collimate the beam, they reduce undesired effusion of bare atoms or molecules into the MC additionally to the cooling shield and the DPS. Despite effusion causing undesired background signal, it does provide a useful tool to determine time-zero and reference peaks in photoelectron spectra (PES). The future PU upgrade with a second oven will give access to controlled doping of two different solid species, further enabling the study of their interaction inside the He_N .

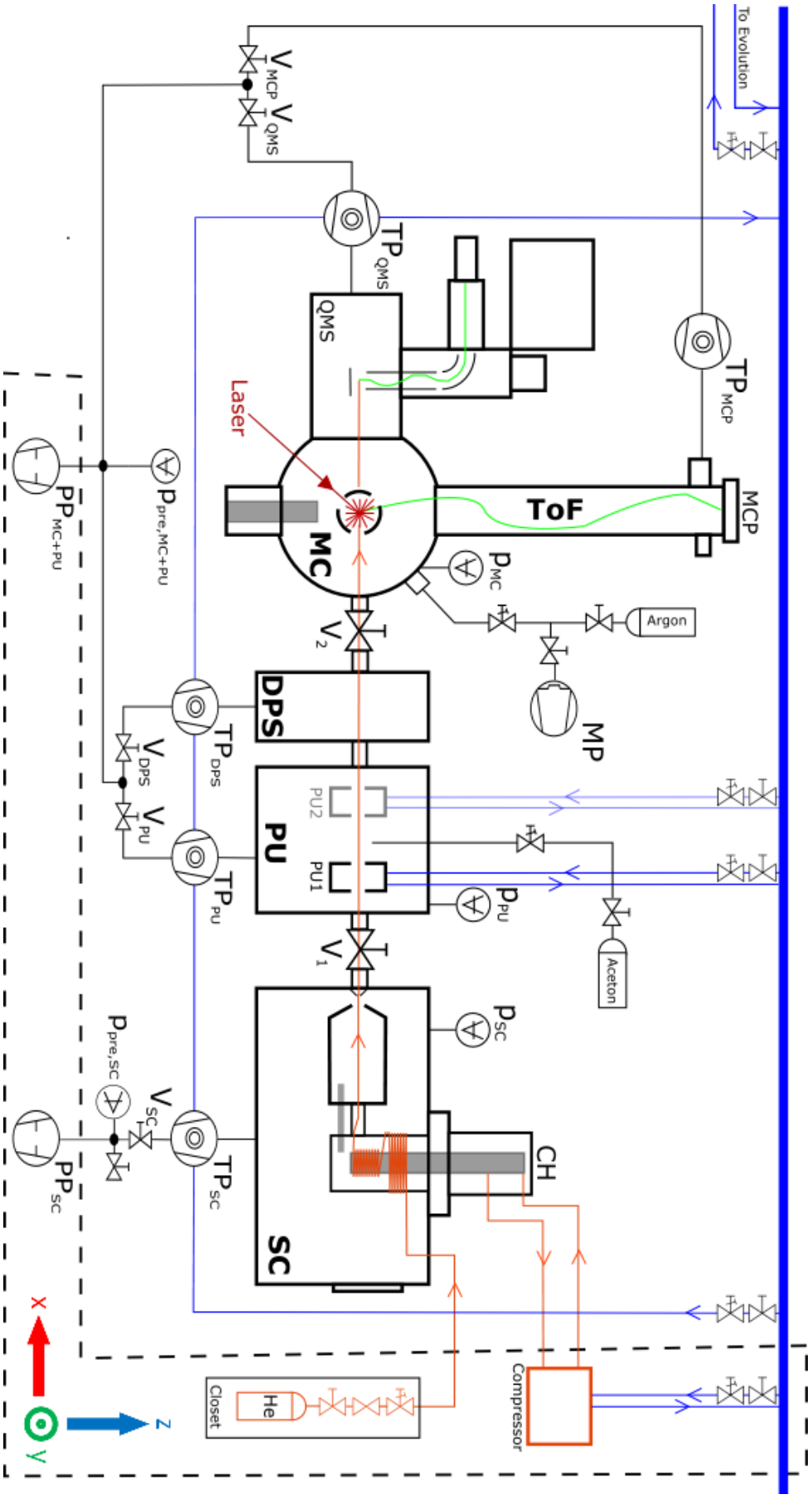

Figure 2.1: Setup overview, general MCP...Micro channel plate, ToF...Time-of-Flight Tube, MC ...Main chamber, DPS...Differential pump stage, PU ...Pickup chamber, SC ...Source chamber, CH ...coldhead, V1 ...valve connecting SC and PU, V2 ... valve connecting DPS and MC. Pre-vacuum (PP, MP), turbo pumps (TP) and pressure gauges (p) are further specified in tab. 2.9 and tab. 2.7. Blue lines indicate water hoses, black lines indicate vacuum pipe lines, orange lines indicate He high pressure pipe lines and He_N trajectories. The red line indicates the laser beam and the green lines depict the ionisation product trajectories. The dashed line indicates which objects are set up in the neighbouring room.

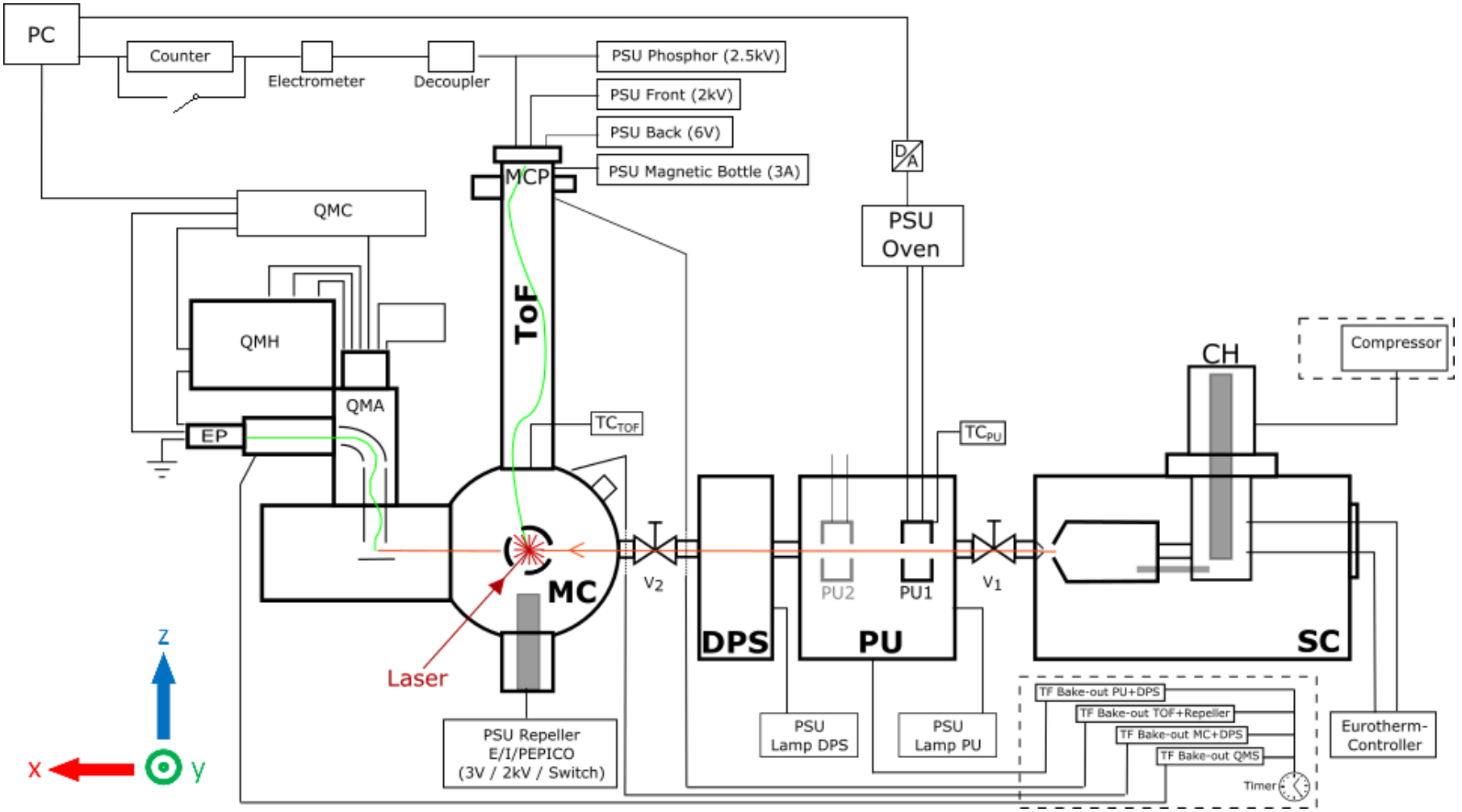

Figure 2.2: Setup overview, electrical wiring
MCP...Micro channel plate, ToF...Time-of-Flight Tube, MC ...Main chamber, DPS...Differential pump stage, PU ...Pickup chamber, SC ...Source chamber, CH ...coldhead, V1 ...valve connecting SC and PU, V2 ... valve connecting DPS and MC, TC_{PU}...thermocouple attached to outer surface of porcelain cup, TC_{TOF}...thermocouple attached to solenoid, EP/QMA/QMH/QMC are the components of the quadrupole mass spectrometer described in sec. 2.5. PSU ...power supply unit, TF ... transformer for heating bands. The orange line indicates He_N trajectories. The red line indicates the laser beam and the green lines depict the ionisation product trajectories. Dashed lines indicate the objects set up in the neighbouring room.

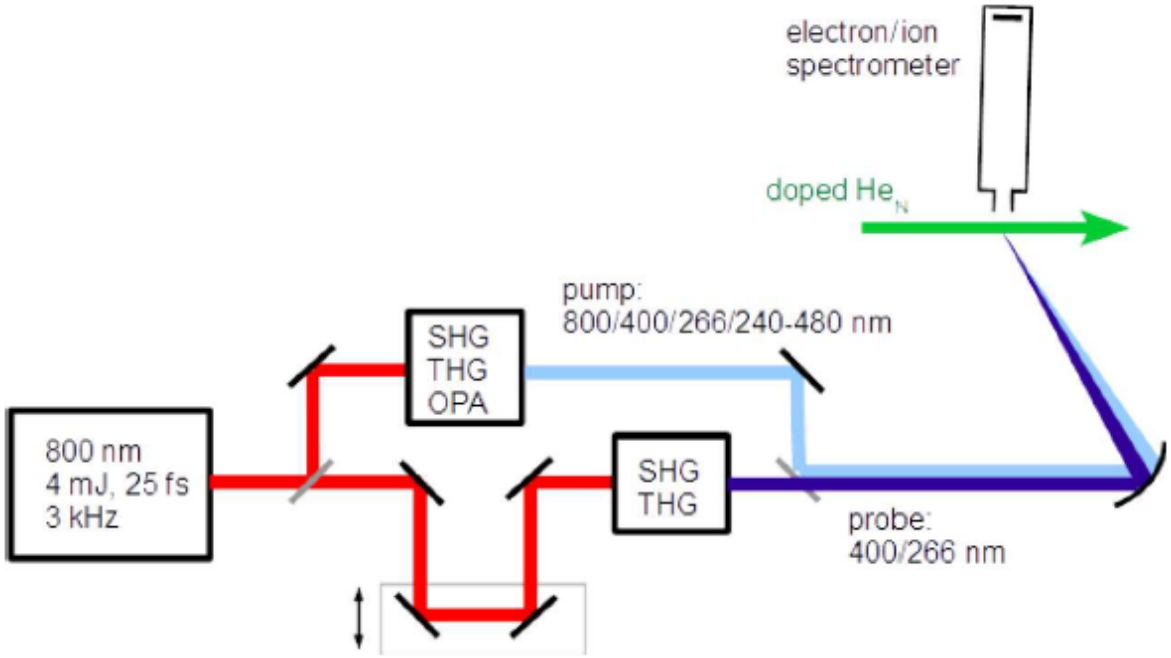

Figure 2.3: Schematic drawing of the optical setup to study photoinduced dynamics in helium nanodroplets, with kind permission by Markus Koch.

2.2 Source chamber

In this section issues of the day-to-day operation are addressed. A detailed documentation of the Source chamber is provided in the Dissertation of Markus Koch. [22]

- The CH and nozzle have to be mounted onto the SC under atmosphere. A pre-alignment, with the help of a dental mirror, of the nozzle ($\varnothing$ 5 μm) to the skimmer ($\varnothing$ 500 μm) is necessary, the exact alignment in y- and z-direction though is done via two screws, lead through to the outside, during operation under observation of the 8u-signal (He_2) in the QMS.
- The compressor should not be operated without water cooling with at least 1 bar pressure in the hose
- The SC should not be operated without a minimum He pressure of 5 bar, as otherwise air might leak into the pipe line and further freeze up and clog the nozzle
- Reaching a minimum temperature of 10.2 K takes approximately two hours. Although, the SC takes another two hours to reach thermodynamic equilibrium. This affects the He gas in the supply pipe line, observable at the pressure reducer manometer on the low pressure side. But more importantly mechanical strain is induced onto the nozzle. The CH still contracts after reaching the final temperature, especially in the non-symmetric z-direction. Because the nozzle is of 5 μm outlet diameter and the skimmer of 500 μm entrance diameter minor misalignment is apparently crucial to the He flow into the skimmer. This means that after some time reduced amounts of He will pass to the QMS if the nozzle optimisation is performed before reaching thermodynamic equilibrium.

- The nozzle alignment can be optimised via the total signal of He_2 (8u) in the QMS. As we are not interested in the gas phase but the droplets, the sole He signal can be used to check whether the He beam alignment is sufficient in principle, but not of further interest.
- A cool-down curve over time can be found in the Disseration of Markus Koch [22].
- The CH is typically operated at 40 bar, a thorough characterisation of the signal yield depending on the He pressure was not conducted until now.
- The droplet size distribution depends heavily on the nozzle temperature. Generally, a colder nozzle temperature causes droplets of larger size and vice versa. Larger droplet sizes directly trade off to a decreased number of droplets generated, impacting the pickup volume and thus the pickup statistics and optical density.
- The helium tank exchange procedure is straightforward but does have some unanswered questions. It was observed that 1-2 days after the tank exchange the pressure in the SC dropped below typical values during full and equibrilated operation of the CH. A possible reason is that that the tank exchange opened a leak at the pressure reducer or pressure release valve right afterwards. The air would freeze up and clogg the CH nozzle, reducing the He flow into the SC and effectively reducing the pressure. A thorough investigation of the whole high pressure pipe line with the leak tester yielded no conclusive picture. The problem was solved by stopping the compressor and letting the CH thermalise with the atmosphere. The pressure drop did not occur afterwards. This suggests that the actual explanation is that air flowed into the He high pressure pipe during the tank exchange, mixed with He and took one whole day to pass through the whole pipe line until arriving at the cold nozzle, freezing it up an clogging it.

2.3 Pickup chamber

2.3.1 Description

The pickup chamber, of which a CAD model is shown in fig. 2.5 on p.12, consists of

- a resistively heated oven consisting of
  - an aluminium oxide coated tungsten cup (6 in fig. 2.5) purchased from FiAS (Firsching Analytical Systems), subsequently called porcelain cup for short, with an electrical feedthrough (2a, 2b) connected to a current source outside. The interconnection is realised with copper clamps (8).
  - a thermocouple attached to the outer surface of the cup
  - the mentioned current source which is controlled remotely with a computer via an interface described below
  - one aperture (⌀ 1 cm) each before and after the porcelain cup
  - a cooling shield with a water supply feedthrough (1a, 1b)
- an optional upgrade to a second oven
- a gas valve
- a differential pump stage (DPS)
- two more apertures (⌀ 1 cm) between the interfaces PU-SC and PU-DPS

The oven and the gas valve respectively are used to form an atomic or molecular cloud through which the He_N pass. While the gas valve simply works with a gas inlet placed right above the He_N beam line, the oven melts and evaporates solid species placed inside the porcelain cup right beneath the He_N beam line. The apertures collimate the He_N beam and reduce effusion of bare atoms or molecules into the MC. Apart from that, further measures of reducing effusion were taken, explicitly being the cooling shield and the DPS. The cooling shield is operated with a simple water hose which is typically operated with 1-2 litres/min. The diminutions connecting the hoses of different diameter, inevitable due to the provided armatures, are custom made at the institute's workshop.

Attention - possible dangers

The cooling shield MUST be operated with sufficient water flux during standby and operation of the oven, as otherwise residual water inside the cooling shield most certainly will boil and squirt through the diminutions' connections, threatening electronic circuitry.

Hardware

The resistive heater consists of the following parts:

Table 2.1: Part list of the resistive heater

part	type
current source	FUG NTN 2800-20
remote control cable	custom made
AD converter (ADC)	EA-UTA 12
heating cables	⌀ 25 mm^2, copper

The current source is operated with currents of up to 120 A. Control of the current is provided via conventional current and voltage limiters operated at the front panel or remotely. The remote control is realised with a custom made cable connecting the current source's LEMO outlet and an ADC especially designed for this type of current source. The ADC in turn is connected via USB to the PC. The pin assignment of the remote cable, both LEMO and D-Sub plug, is as follows:

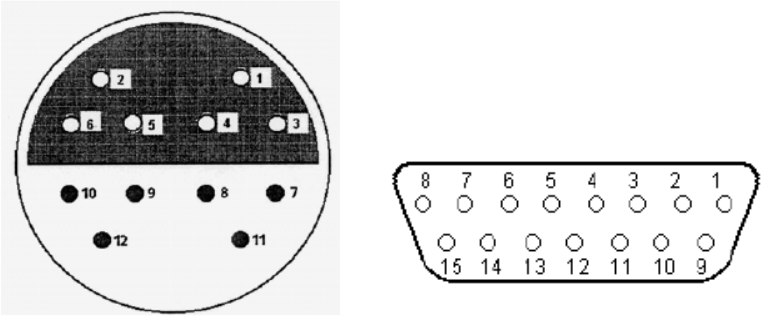

Figure 2.4: Pin numbering of the current source's remote control cable, solder side. See pin assignment in tab. 2.2

Table 2.2: Resistive heater FUG PSU LEMO and ADC D-Sub plug solder side pin assignment. Pin numbering see fig. 2.4. For further information see ref. [23] and app. B.1

D-Sub pin	assignment	LEMO pin	assignment	strand color (LEMO pin numbers)
1	output channel 1 (Uset, 0-10V)	1	0V	black
2	output channel 2 (Iset, 0-10V)	2	+10 V reference	brown
3	n.c.	3	Output I/O (On if connected to 0V)	red
4	analog ground	4	current monitor (Imon, 0-10V)	orange
5	n.c.	5	voltage monitor (Umon, 0-10V)	yellow
6	n.c.	6	n.c.	green
7	n.c.	7	voltage set (Uset, 0-10V), s.c. with +10V	blue
8	n.c.	8	n.c.	violet
9	input channel 1 (Umon, 0-10V)	9	n.c.	grey
10	input channel 2 (Imon, 0-10V)	10	n.c.	white
11	digital ground	11	current set (Iset, 0-10V)	pink
12	n.c.	12	n.c.	turquoise
13	n.c.			
14	n.c.			
15	n.c.			

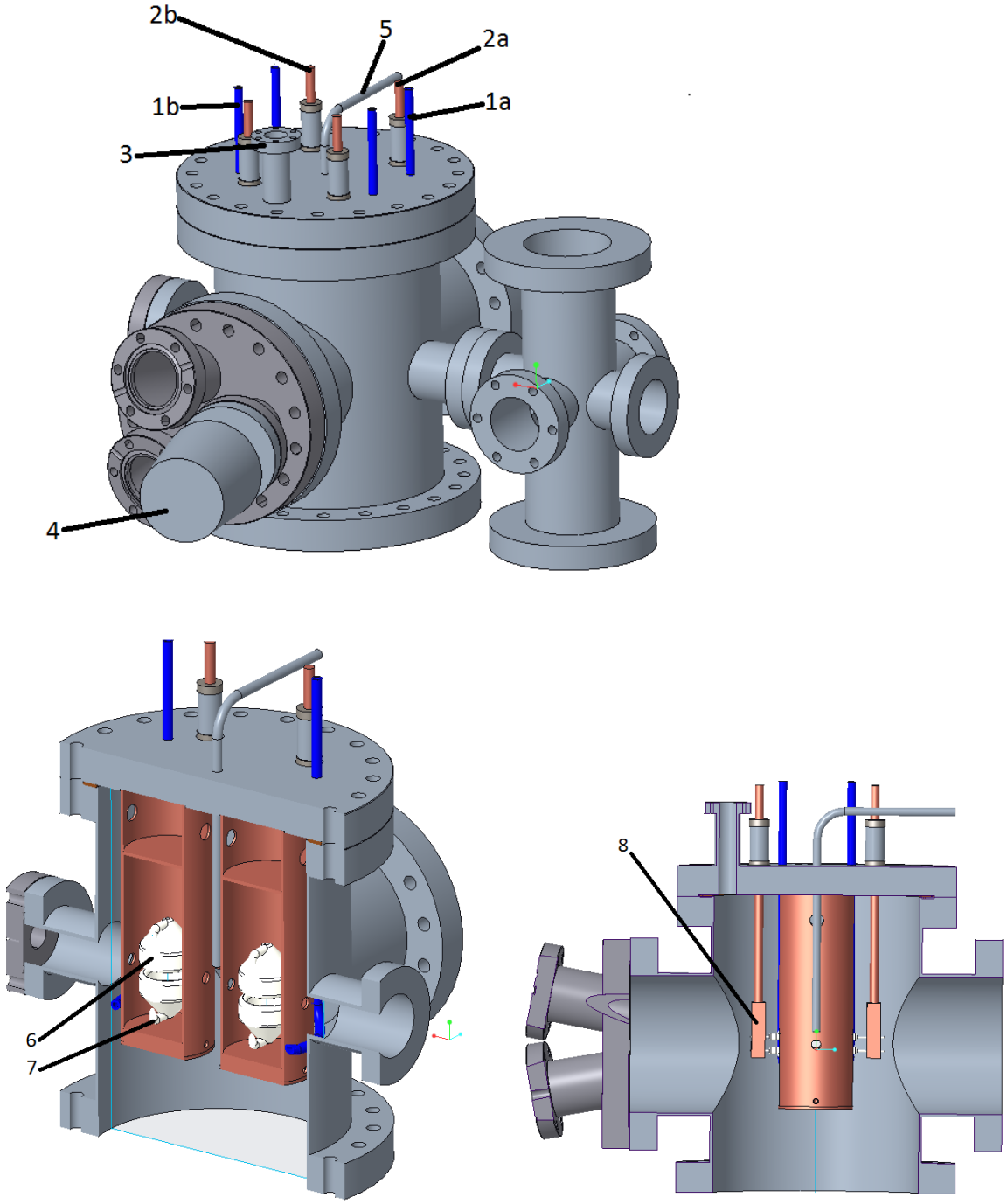

Figure 2.5: PU and DPS CAD models, with kind permission by Philipp Thaler. 1a...water hose 1, 1b...water hose 2, 2a...current supply line 1, 2b...current supply line 2, 3...lead-through of the thermocouple, 4...pressure gauge, 5...gas inlet, 6...porcelain cup, 7...tungsten wire, 8...clamps

Software - communication between ADC and PC

This section is an excerpt of the corresponding ADC user manual [23]. The ADC translates the analog signals into a hex number which has a structure as documented in fig. B.1., and also needs input of the same form. The corresponding command and reply lists are documented in the appendix on p.79 and p.80. After conversion to decimal numbers, the values still do not represent physical values. To this end, the physical measurement values have to be calculated from the signal upon receiving. In return the physical values have to be converted into measures of the ADC upon sending.
Physical measurement values are calculated AFTER translation from hex to dec according to the formula

$$I^{dec}_{actual}[A] = \frac{I^{dec}_{signal}}{15565} \cdot I_{max}[A]$$
$$U^{dec}_{actual}[V] = \frac{U^{dec}_{signal}}{15590} \cdot U_{max}[V]$$

On the other hand, digital signal sent from the computer BEFORE translation from dec to hex is translated according to the formula

$$I^{dec}_{signal}[V] = \frac{I^{dec}_{actual}[A]}{I_{max}[A]} \cdot 62228$$
$$U^{dec}_{signal}[V] = \frac{I^{dec}_{actual}[V]}{U_{max}[V]} \cdot 62066$$

where I stands for current, U for voltage, the superscript dec indicates that all values are in decimal system, the subscript $signal$ corresponds to the physical value, with subscript $actual$, converted to measures of the ADC, which are represented by the numerically denoted parameters. The subscript max refers to the physical limits of the current source's output being 120 A and 20 V in case of the device used as noted in tab. 2.1.
Due to historical reasons, both steps of the translation (number system and physical values) are effectively carried out in the sub-routines i2m.m and v2m.m respectively for the direction PC-to-ADC, and directly in the general operation scripts (preheater.m, postheater.m, temp_control_gui_II_pickup_femtolab_v2.m) in the case of ADC-to-PC. A code example of both directions is provided in lst. B.1, the translation parameter read-out in lst. B.2.

2.3.2 Operation

In this section the handling of the hardware and software to operate the oven are outlined. Further, a current-temperature-curve (fig. 2.6) and the discrepancy of the two temperature measurement methods (tab. 2.3) are depicted.
When switching from front panel to remote control, it is advised to first activate the remote control via the mechanical red switch at the front panel, and second to execute the software. Vice versa, it is advised to first end the file execution (e.g. press 'end control' in the PID-controller's GUI), and second deactivate the remote control mechanically. This advise is due to possible residual voltages in the ADC. In the latter case one must also set the front panel's configuration accordingly for a continuous current supply to avoid discontinuous temperature changes.
In general the PID-controller implemented in the routine
temp_control_gui_II_pickup_femtolab_v2.m is the tool of choice for the temperature control of the pickup, with a guide value for fastest heating being ± 1200°C/h **above** 200°C. Yet at temperatures below 200°C the resistance measurement employed in said controller is highly inaccurate due to a high sensitivity to small measurement errors of low currents, thus leading to a loss of control of the temperature evolution. High and sudden temperature fluctuations might damage the porcelain cup. To tackle this, the scripts preheater.m and prostheater.m were developed for the regime of 21-200°C which abandon the resistivity measurement and follow a fixed empirical current-temperature ramp within four hours instead.

preheater.m

The preheater is a script used to ramp up the temperature in the PU from room temperature up to ca. 200°C at a moderate pace. This is required as the porcelain cup is likely to crack upon too sudden temperature changes, even more so when cooling down. The script consists of a 2nd order polynomial fitted to empirical values of the current-temperature-curve (see fig. 2.6). The controller sets the current in discreet equally spaced steps after a specified, empirically determined amount of time. E.g. the script sets the current to 5.0 A upon file execution. After holding the current constant for 50 sec, it is changed to 5.1 A for another 50 sec and to 5.2 A after another 50 sec. For high currents, the time between two current steps is doubled. This measure is related to the current-temperature-curve being non-linear. When the maximum current is reached, the preheater enters an endless loop maintaining the maximum current. It is generally advised to start the preheater with 5 A as non-observable heating takes place below. Further, one should switch to the much faster PID-controller for temperatures above 200°C (temp_control_gui_II_pickup_femtolab_v2.m).

postheater.m

The postheater is of exactly the same structure and functionality as the preheater, but is used to cool down the PU in a controlled, not too sudden manner. Note that the empirical current-temperature-curve slightly differs from the one in the preheater. The hysteresis arises from the procedure not being quasi-stationary.

temp_control_gui_II_pickup_femtolab_v2.m

The PID-controller was originally developed by Philipp Thaler and refined by several members of the Ernst group over the years. The basic idea is to calculate the temperature-dependent resistance via voltage and current measurements and then calculate the temperature increment from proportionals, integrals and differentials (PID) of the resistance. It is generally used for ramping the temperature of the PU in the range of above 200°C. The controller also monitors and visualises current, voltage, power and temperature. Despite rumours of heating ramps too high causing the porcelain cup to crack, we did not experience any problems with ramps in both directions of up to ± 1200°C / h in the range of 200°C to 600°C.
Due to the wiring of the current source, one is advised not to change the value of *U_max* in the GUI. Furthermore, one is advised to set the variable *I_test* to *I_min* in the case of heating up from 200°C and to set the variable *I_test* to *I_max* in the case of cooling down to 200°C.
Because the PID-controller's resistively measured temperature might drastically deviate from the directly measured value, it is advisable to set the temperature way beyond the desired point and actually limit the controller with the maximum and minimum current values, which in turn are empirical values too. E.g. set *I_max* to the point of operation and *I_min* to the standby value (typically 20 A at 200°C). Then one can set the temperature to way above the actually desired value in case of heating up, and way below when cooling down.
Note that the temperature, measured with the thermocouple (TC) at the outer surface of the porcelain cup, is merely a reference value. Theoretical considerations suggest that the TC measurement underestimates the interior vapour pressure by two orders of magnitude, resulting in a temperature being actually 100°C higher than measured. This discrepancy seems to occur only at high temperature way above 200°C.

Table 2.3: Oven temperatures during operation in steady state measured resistively and with a thermocouple. The discrepancy increases with higher temperatures.
T_{PID}...resistively measured temperature
T_{TC}...temperature measured with thermocouple

T_{PID} / °C	T_{TC} / °C
90	99
120	128
150	160
190	195
200	206
200	204
340	320
450	406
500	440
700	580

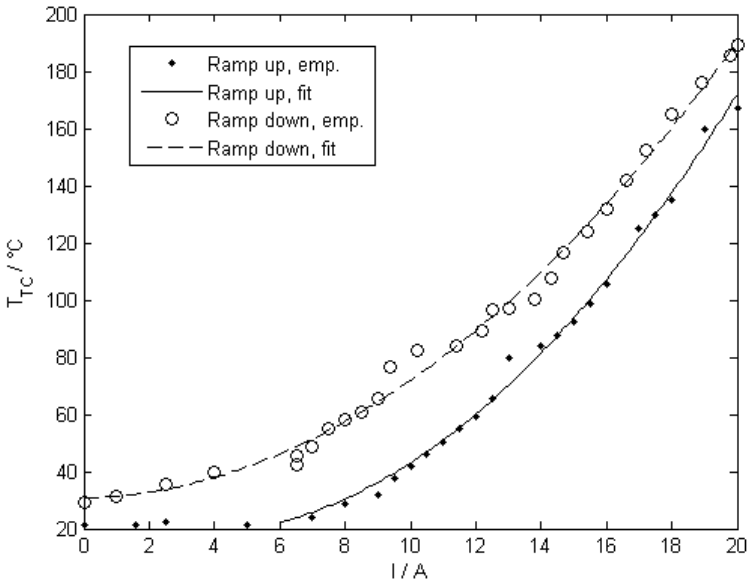

Figure 2.6: Current-temperature curve for heating up and cooling down in the regime of 20-200°C in a controlled manner

2.3.3 Refill procedure

The refill procedure takes one day, provided the procedure is started in the morning. Important steps possibly leading to damage to the setup are marked with an asterisk. Major risks are excess pressure in the PU and accidentally venting the MC via the prevacuum line.

Characteristic behaviour prior to material depletion

Upon material depletion the corresponding TOF and QMS signals vanish within seconds. Further, it was observed that the necessary current to achieve a temperature as measured with the thermocouple increases continuously over time. The temperature inside the cup is suspected to be way higher than on the outer surface. This could be due to suppressed heat radiation inside the cup due to a smaller surface of the molten mass. As the material depletes, the radiating surface increases, effectively cooling the porcelain cup at a given current. Another explanation would be that the porcelain's residual conductance links the total volume of material in the cup to the total resistance. The most important effect though is a decrease in melt surface upon material depletion due to the conical shape of the porcelain cup. At a given temperature, a decreased melt surface accounts for a lower vapour pressure. To compensate this effect, one must increase the temperature or the current respectively to achieve the same pickup conditions realised a few days earlier. According to the vapour pressure curves in fig 2.7, a difference of 50°C in temperature corresponds to a difference of one whole order of magnitude of the vapour pressure. For this reason one might want to avoid the maximum working point in fig. 2.19 and rather work at lower temperatures to effectively increase measurement time until a refill is necessary. Apart from that, possibly undesired multi-pickup is increased at higher temperatures.

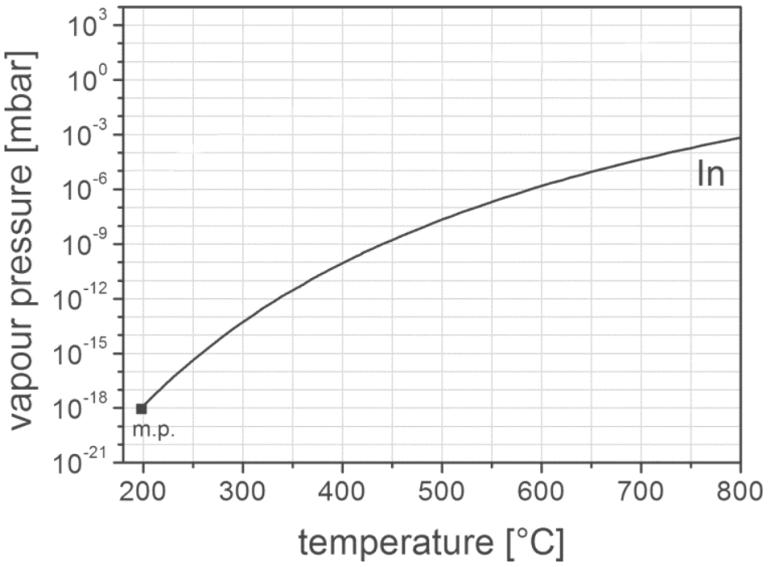

Figure 2.7: Indium vapour pressure curve [24]. The typical background pressure measured in the PU during operation with ca. 600°C as measured with the TC is typically in the range of a few E-07 mbar. Theoretical considerations about the pickup statistics suggest that the actual vapour pressure is in the regime of E-04 mbar, indicating the true temperature to be underestimated by the TC by up to 100°C, which is actually close to the resistive measurements as can be seen in tab. 2.3. 'm.p.' indicates the melting point.

Step-by-step manual

The actual refill takes about 1 hour, the step-by-step recommendation is as follows:

1. Ramp down the oven to room temperature using the scripts described in sec. 2.3.2. This step usually takes 3-4 hours.
2. Remove top flange aluminium foil cover.
3. Document top flange alignment with markers and photos.
4. Close valves V_1 and V_2.
5. Turn off turbos TP_{DPS} and TP_{PU}, be aware that these two pumps are on the same prevacuum line as the MC. Simultaneously close valves V_{DPS} and V_{PU}.
6. Wait until turbos are standing still.
7. Untighten the screws of the top flange for safety reasons. The pressure difference will prevent uncontrolled venting. This specifically works best with Viton gaskets, but proved applicable with copper gaskets too.
8. One may want to let the electrical and water circuitry on the top flange be connected.
9. *Slowly vent with an inert gas (Ar, He, N_2) using either the turbo's venting valve or the gas inlet while observing the pressure gauge. The loose top flange will slowly rise and release excess pressure. Be aware that the pressure gauge is not calibrated to pressures above high vacuum (> 10E-4 mbar). For the turbo's venting valve an additional excess pressure safety valve is planned in the near future.
10. Carefully lift the oven attached to the top flange out of the chamber. It turned out to be practical to put it onto the laterals of an upside down stool on the optical table. One should cover the laterals with aluminium foil beforehand.

11. Detach the thermocouple.
12. Demount the cup. Be careful to not apply any strain to the cup as it may crack.
13. Fill in desired material.
14. Mount the cup.
15. Attach the thermocouple, perform a quick test of functionality
16. Exchange copper gasket ring.
17. Lift oven into chamber.
18. Make sure the alignment markers both of the chamber and the flange match.
19. Tighten screws.
20. ∗Close valves V_{QMS} and V_{MCP} as well as the gas inlet valve on the PU top flange.
21. ∗Open valves V_{DPS} and V_{PU} while observing the pressure.
22. Wait until a prevacuum suitable for the turbos is reached
23. Turn on turbos TP_{DPS} and TP_{PU}.
24. ∗Open valves V_{QMS} and V_{MCP} while observing pressure.
25. Cover top flange in aluminium foil again.
26. Simultaneously start preheater and bake-out procedures as described in sec. 2.3.2 and in sec. 2.6.5. It is sufficient to limit the bake-out to the PU+DPS subsystem. Further, it turned out to be sufficient to end the bake-out and let start the cool down on the very same evening or during the night using a time switch.
27. The PU is ready again for operation the next morning.

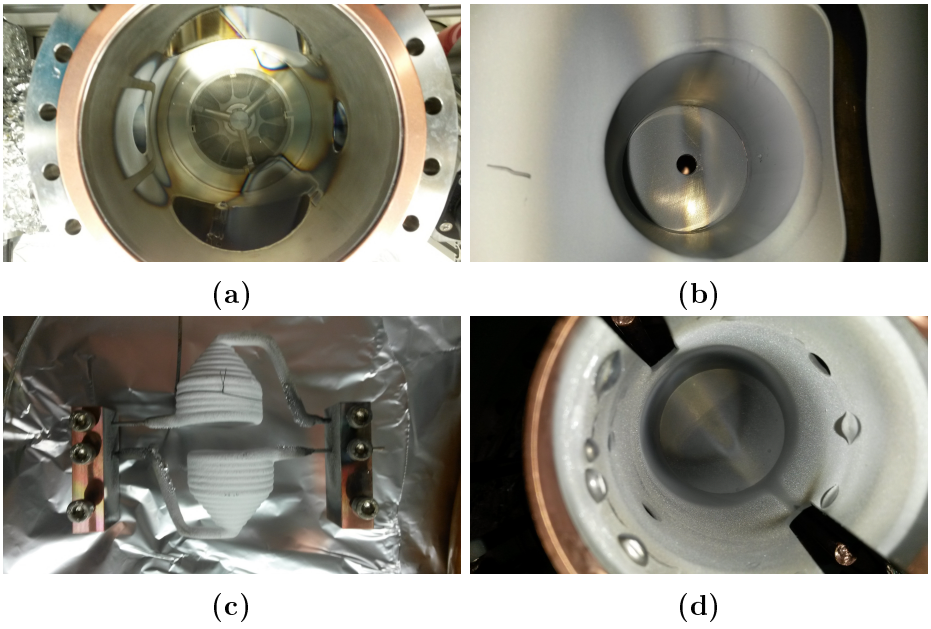

Figure 2.8: The PU chamber's interior after ca. 45 effectively operating days.
(a) PU, angle from above, the left side points into the direction of the MC. White effusively caused In film adsorbed to the wall and its shadows are visible. (b) The lead-through from the PU to the MC and its aperture. The high contrast shadow originates from the second cooling shield's water hose, the low contrast shadow slightly below the aperture from the first cooling shield. This becomes reasonable by considering that only few atoms are expected to have a momentum pointed in the direction of the He beam. (c) Massive In droplets have formed on the arms. (d) Angle from below into the cooling shield. Also on the inside wall of the cup's containment massive In droplets have formed.

2.4 Time-of-Flight spectrometer (Main chamber)

The TOF can measure the electron kinetic energy or ion charge-to-mass ratio via measuring the time of flight. Documentation of the TOF and its circuitry depicted in fig. 2.9 can be found in the Master's theses of Markus Bainschab [21] and Paul Maierhofer [20]. In contrast to gas phase experiments, it is non-trivial that the laser beam crosses the He beam. As the He_N beam alignment can only be done under atmosphere, one is limited to adjusting the laser beam path in z-direction (definition of coordinate system see fig. 2.1). Tests suggest that the He beam has a diameter of 2-3 mm. In combination with the laser focus being typically of 0.5 mm diameter or even less, adjusting the ionisation volume to the He beams centre is apparently crucial to the total signal yield. Because the laser focus' extent in x-direction is quite large for the currently used lens of 1 m focal length, the ionisation volume and therefore signal yield is only weakly sensitive to alignment in x-direction. At last it is obvious that the signal yield only depends on alignment in the y-direction such that it affects the collection efficiency of the magnetic bottle. It was found that the He beam's centre is in the proximity of z=-7.5 mm as measured via the repeller, meaning the laser focus being at ca. z=-7.5 mm and the repeller adjusted to z=-9.5 mm. These values refer to the total electron signal yield and the measurement is documented in the characteristics sec. 2.9.1.

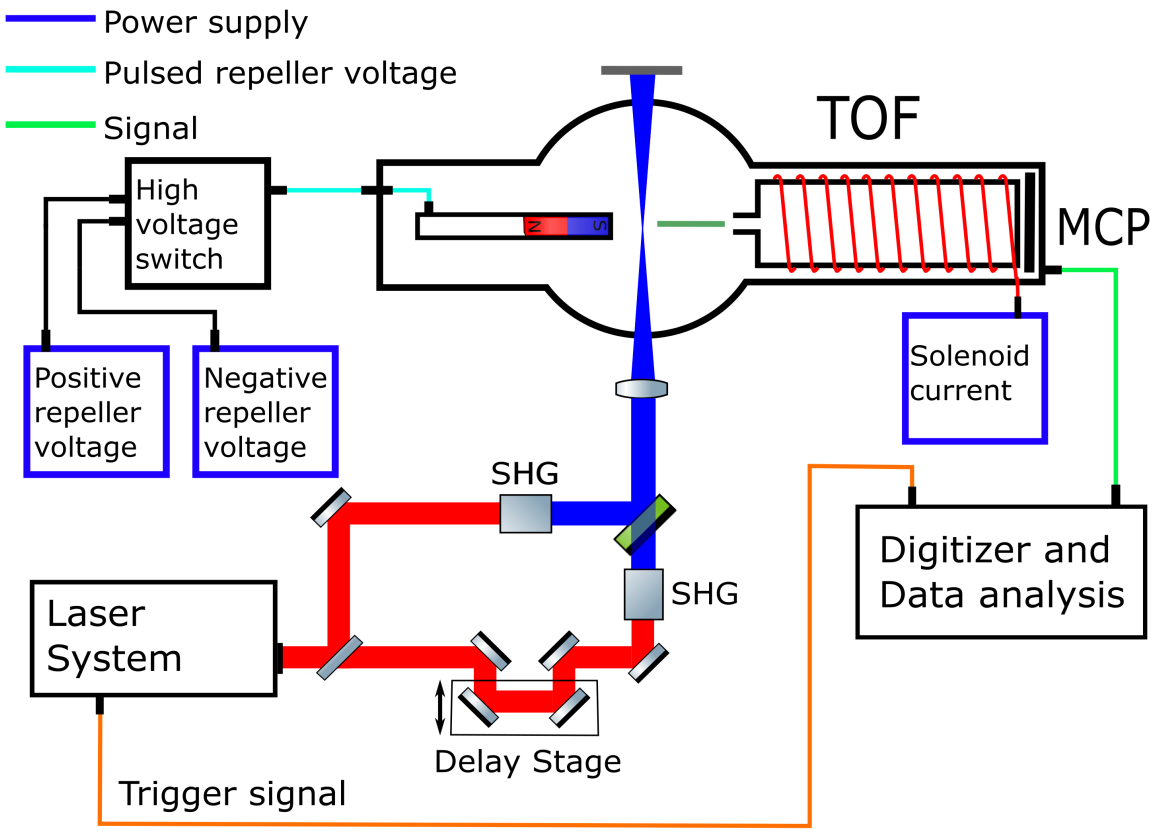

Figure 2.9: Time-of-Flight Spectrometer, with kind permission by Paul Maierhofer [20]

2.5 Quadrupole mass spectrometer

In this section two different operation modes, using a secondary electron multiplier (SEM) or a Faraday cup, and two different detection schemes, using an electrometer or a counter, are described. Further guidelines for handling the original software Quadstar 422 and some features of the RS232 communication for custom-made software are presented. Additionally, some basis debugging strategies are advised. Most of this section is an excerpt of detailed documentations and manuals provided by Balzers Instruments or Pfeiffer Vacuum GmbH respectively. [25–28]

2.5.1 Description

A system part list is provided in tab. 2.4 and a schematic drawing of their wiring is depicted in fig. 2.10, followed by detailed discussions of aspects of the analyser and the controller.

Table 2.4: Equipment list of the QMS

part	type	Inv. no
Controller (original)	QMG 422	-
Controller (IF)	QMG 422	0029084
RF-Generator	QMH 400-5	-
Analyser	QMA 400	-
Counter	CP 400	-
Electrometer	EP 422	-

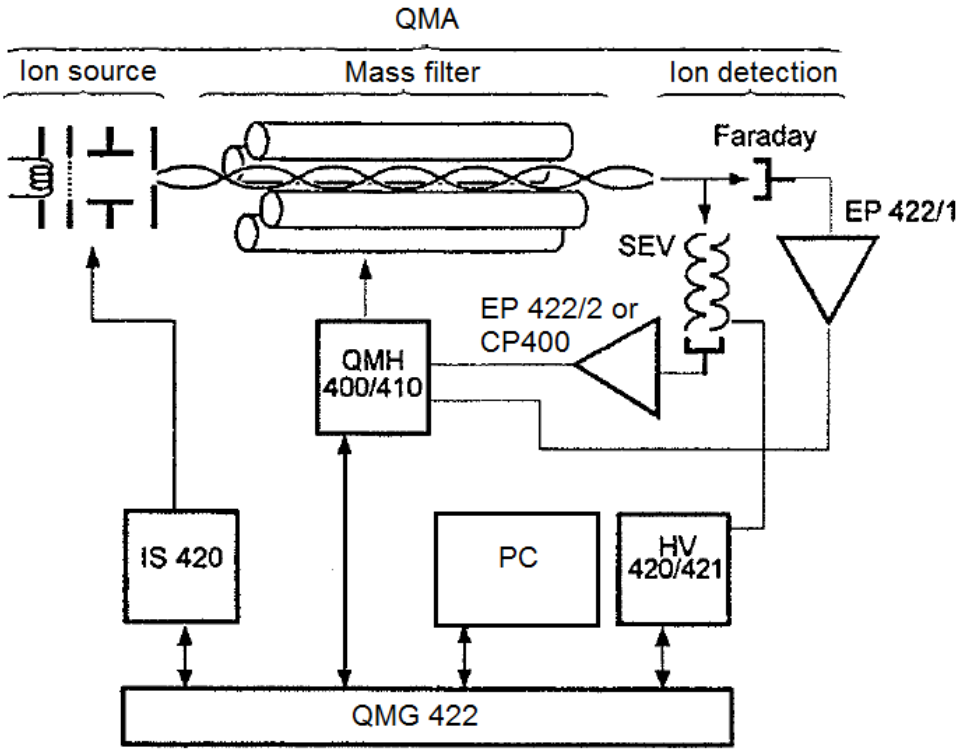

Figure 2.10: Overview of the quadrupole mass spectrometer system

Analyser [25, 26]

Schematic drawings of the setup and corresponding circuitry for the different operation modes are shown in fig. 2.11 and 2.12. Sensitivities are compared in tab. 2.5. The rod potentials referred to in this section are listed in tab. 2.6 and with a corresponding plot in fig. 2.13.

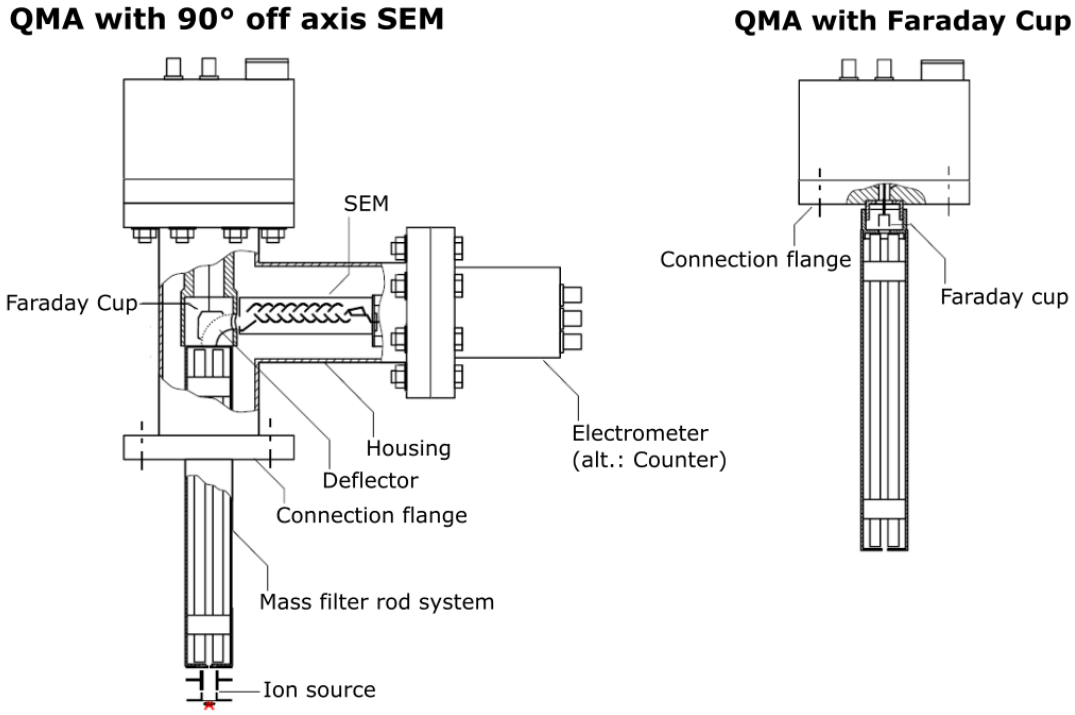

Figure 2.11: Quadrupole mass analyser (QMA) with its two different operation modes and two different detection schemes. The circuitry is sketched in fig. 2.12.

The ionisation is achieved by electron impact. Electrons are thermally emitted by a cathode and focused by electrical extraction fields so that they reach the ionisation area. V1 IonRef is the nominal potential on which the ions are formed. In general, the IonRef should be set slightly higher than the electron energy (V2 Cathode). The cathode is thus on a positive potential with regard to ground so that no electrons are emitted to the environment. This prevents interference with the Faraday cup of the system and nearby measurement equipment (e.g. ionisation manometer). The cathode voltage determines the acceleration voltage of the electrons and thus the nominal ionisation energy. The ions are then drawn out by the extraction electrode and focused into the mass filter through the ion lens (V3 Focus). The FA voltage (V4 Field Axis) is the potential difference between the ionisation area (IonRef) and the quadrupole mass filter. FA therefore defines the kinetic energy (velocity) of the ions in the rod system. The higher the value, the higher the peaks. However, the resolution is lower and the peak shape deteriorated. Exceedingly high FA values result in frayed peaks. If with the parameter 'Resolution' the resolution is not improved and the peak level is decreased, lower the FA value. The extraction voltage (V5 Extraction) accelerates the ions from the ionisation area towards the rod system. The deflection voltages (DEFI and DEFO) direct the ions through the 90° deflection condensator. For the QMG 422 used in this laboratory the deflectors are automatically

switched to ground potential in Faraday operation. The inner deflection plate is on potential V6 DEFI, the outer deflection plate is on potential V7 DEFO. The Faraday cup is isolated from the deflection plate and connected to the electrometer amplifier EP1. The 90° off-axis arrangement of the secondary electron multiplier has a very low signal background because the electrostatic 90° deflection prevents fast or excited neutrals and photons from hitting the SEM. Faraday cup operation reduces system related conversion errors of the SEM (e.g. mass discrimination). Faraday operation can also be used for error detection. The drawback of Faraday operation is the lower sensitivity, which requires a higher gain and thus limits the response speed.

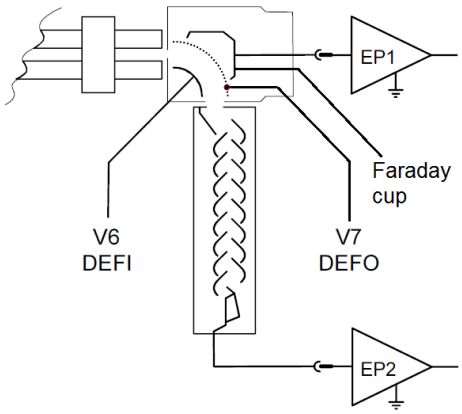

(a) Operating modes overview

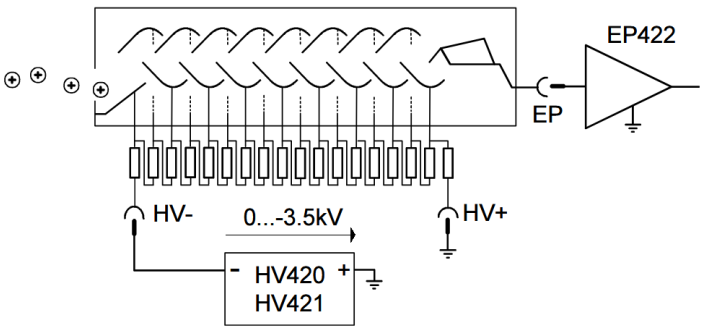

(b) SEM mode eletrometer circuitry

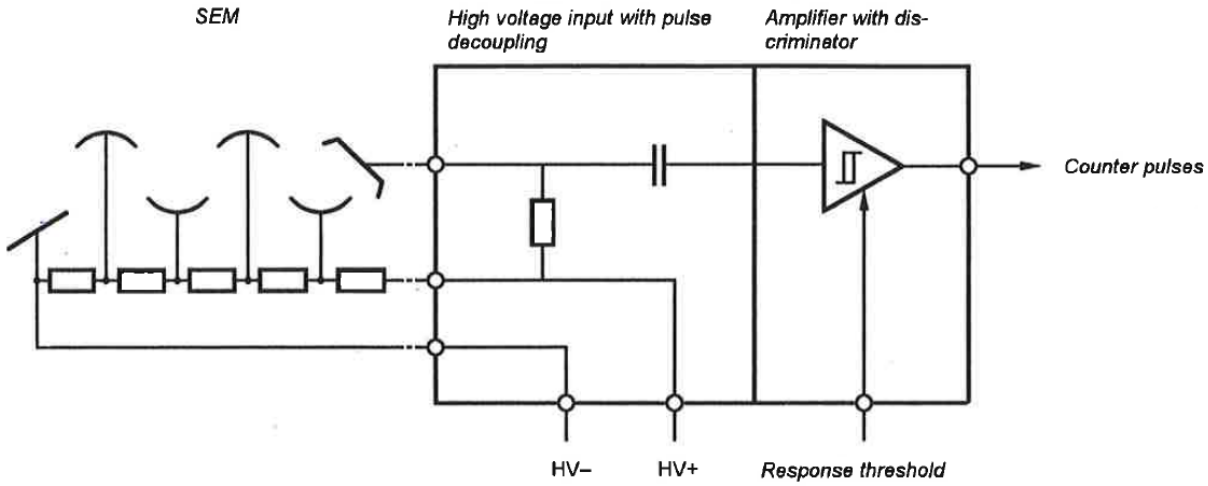

(c) SEM mode counter pulse decoupler

Figure 2.12: QMA circuitry overview. (a) QMA circuitry in SEM-operation (EP2) or Farady-cup-mode (EP1). For the former, either the inner deflector is on a potential and the outer deflector is short-circuited with the Faraday cup and grounded, or both the inner and the outer deflector are on a potential. For the latter, both deflectors are grounded. SEM mode can operate with either an ion current detection scheme using the electrometer (EP) or alternatively with a pulse decoupling scheme using the counter CP400 instead. (b) SEM circuitry with ion current detection (electrometer). (c) SEM circuitry with pulse decoupling (counter)

Table 2.5: Sensitivity of the QMS. p_{min} is the smallest detectable partial pressure.

	Faraday mode	SEM mode
p_{min} / mbar	$< 10E-11$	$< 10E-15$

Table 2.6: QMS rod potentials and their typical values in SEM-mode. Detailed description in text

No.	Name	U / V
V1	IonRef	100
V2	Cathode	70
V3	Focus	15.75
V4	FA (Field Axis)	27
V5	Extraction	300
V6	DEFI (Inner Deflector)	300
V7	DEFO (Outer Deflector)	110
V8	Reserve	-
V9	Wehnelt	-

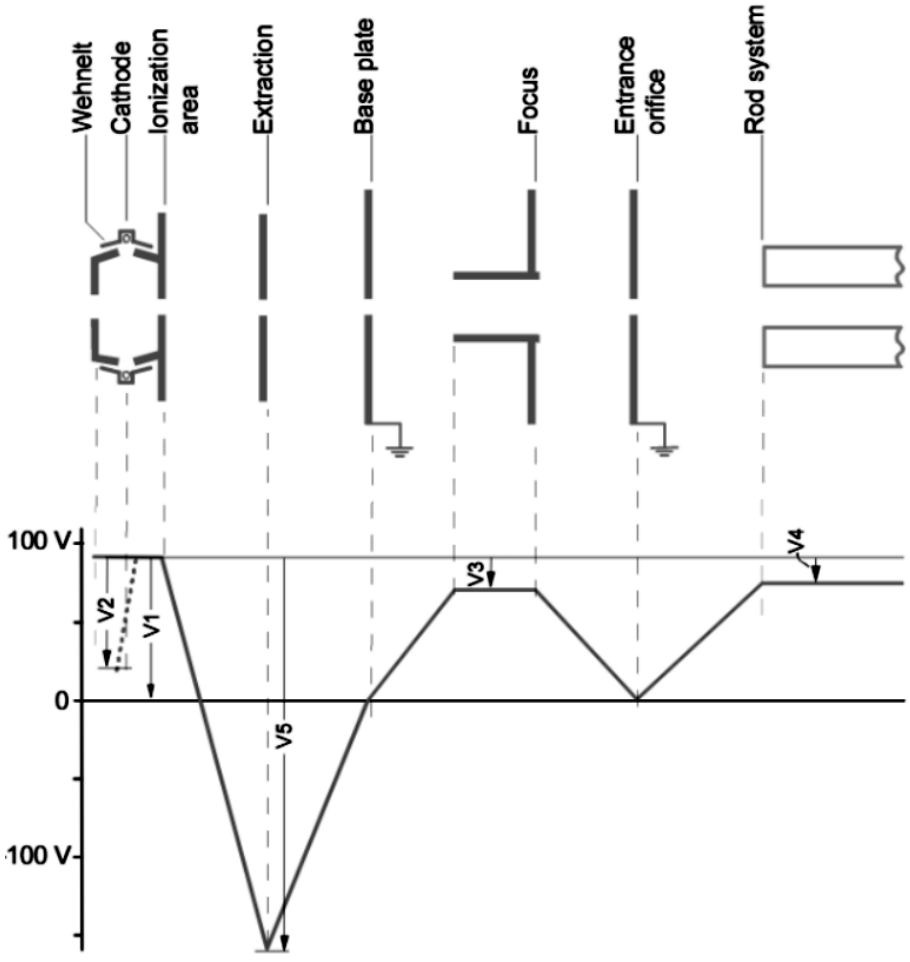

Figure 2.13: Schematic drawing of the potentials of the cross-beam ion source

Controller [27]

For communication of the PC with the QMG using the RS232 standard a handshake protocol is employed. To this end the class *QMS_balzers.m* with basic functions was developed (App. A). The class contains only the basic functions needed for a simple GUI to monitor counter signals live (*QMS_GUI.m*) and two scripts, one monitoring signal over time (*QMS_timescan.m*) and another recording mass spectra (*QMS_massscan.m*). Note that the class is written to be used in the cumbersome work-around configuration with the CP400, the cluster lab 2 (CL2) photon counter, the CL2 chopper serving as trigger for the photon counter, the Stanford counter and its corresponding class. It can easily be adapted to directly read the signals from the QMG controller. To do so in SEM counting mode, one has to first adapt the custom-made counter-to-signal transmission cable, i.e. simply connect the two wires which are detoured from the D-Sub plug to their opposite D-Sub pins. The QMS_balzers class was actually developed in order to offer an alternative to debugging the original software Quadstar 422 with the also custom-made LabView script. For day-to-day business usually the original software Quadstar 422, described in further detail in sec. 2.5.2, is used. The most basic and general function, employing the handshake, is 'communicate' (see lst. 2.1) . Any settings and requests can be transmitted with 'communicate'. The complete and detailed list of all mnemonics can be found in the QMG communication protocol [27]. Note that the destructor (lst. 2.2) employs some safety measures, i.e. turn off the SEM-HV as well as the emission current.

Listing 2.1: Handshake protocol invoked by the function 'communicate'

```
function [value] = communicate(obj, string)
    % Send string
    fprintf(obj.serialConn, string);
    % Receive Acknowledgement
    pause(0.1)
    ack = sprintf(fgetl(obj.serialConn));
    pause(0.1)
    if 6 == ack;
        % Enquire and update value
        fprintf(obj.serialConn,['%s',char(5)]);
        value = sprintf('%s',fscanf(obj.serialConn));
    else
        fprintf('Communication failed,...
          no ACKnowledgement received')
    end
end
```

Listing 2.2: QMS class destructor with safety precautions

```
function delete(obj)
    obj.HV_switch(0);
    obj.current_switch(0);
    fclose(obj.serialConn);
end
```

2.5.2 Operation

This is a comprehensive guide and excerpt from [28].

Booting

After using the mechanical power switch on the QMG controller the RF-generator QMH usually takes 15 minutes to boot. When starting one of the three main programs 'TuneUp', 'Parset' or 'Measure', one first has to establish a connection via the menu item 'Comm'. If the RF-generator has not booted yet, an error message 'RF error' will be prompted, which can safely be ignored. For the filament to reach thermodynamic equilibrium early it is advised to turn on the emission current straight away via the menu item *Setup* → *SEM/emission control*. Do not turn on the HV yet. Before going on to measurements, one has to create a file with the fitting parameter set.

Configuration Setup

The configuration setup documented below in fig. 2.14 holds for SEM operation with electrometer ion current detection. When operating with count pulse decoupling or Faraday mode one has to adapt the configuration accordingly. The system can be configured with the programs *TuneUp* → *Tune Ion Source* and *Parset* → *Configuration*. All settings are stored in a file which will be prompted to choose upon starting a measurement.

Measurement

After the system configuration files are created one can proceed to measuring. First one should turn on the HV and emission current with *Measure* → *Setup* → *SEM/Emission control*. A standard method is **M**ultiple **I**on **D**etection. Upon following *Measure* → *MID* → *Table/Bargraph/vs.Time*, one will be asked to load a configuration file. There are configuration files *AIRSEM.MIP* and *AIRFAR.MIP* delivered with the software which are calibrated to air and to their according detection mode, former for SEM and latter for Farady mode. A new GUI will appear and load the configuration, which takes a few seconds and is indicated by the text 'Zero Equalise' and a red dot on the bottom left. After the dot turns green, one can again choose one of the visualisations (*Display* → *Table/Bargraph/vs.Time*). Check whether all measurement parameters, such as integration time and amplifiers, are set correctly via *Parameters* → *Channel*. The example given below (fig. 2.15) worked quite well for monitoring the pickup statistics during the indium experiments in SEM mode with ion current detection.

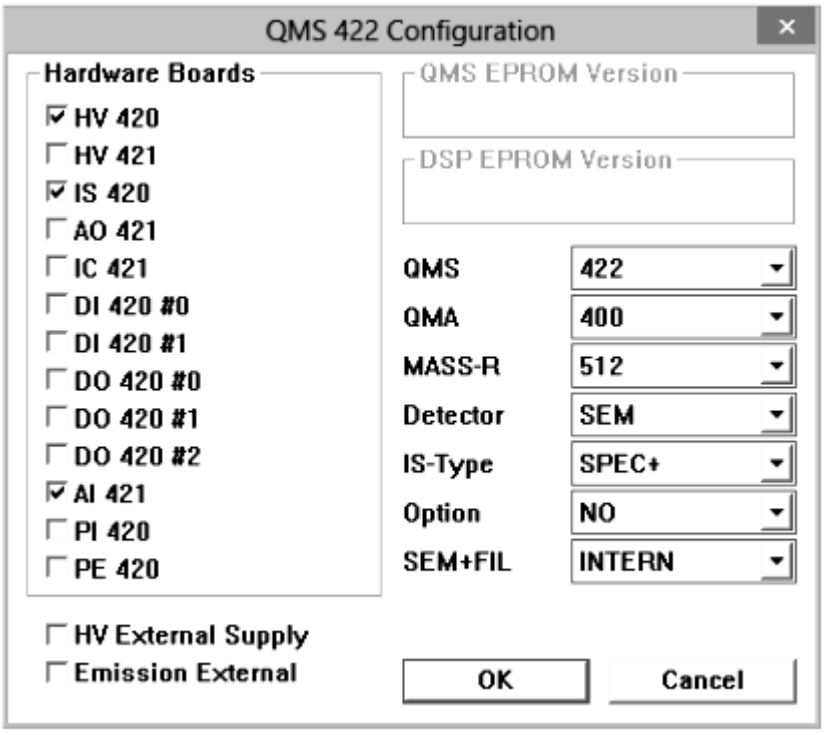

(a)

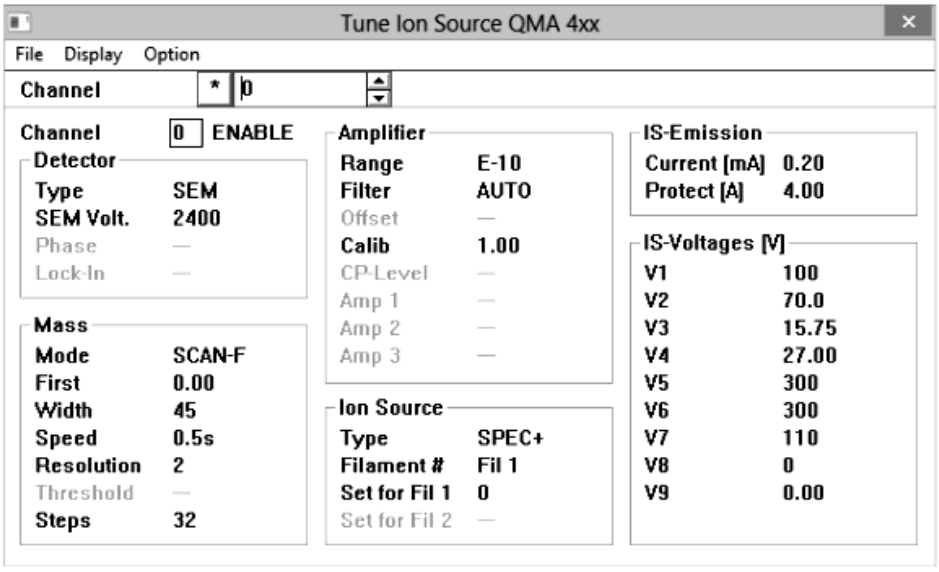

(b)

Figure 2.14: Quadstar configuration setup using the programs (a) 'Parset' and (b) 'TuneUp' for SEM operation and electrometer ion current detection scheme.

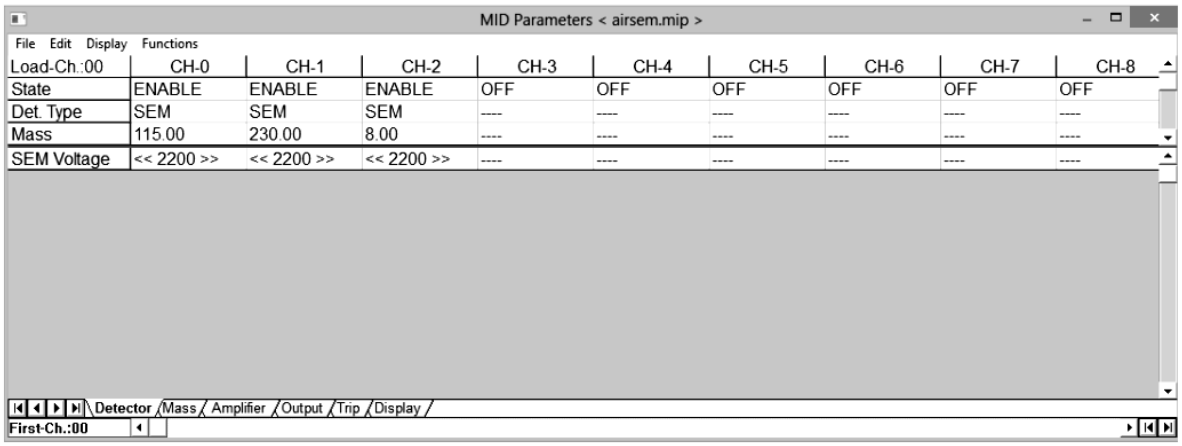

(a) Detector

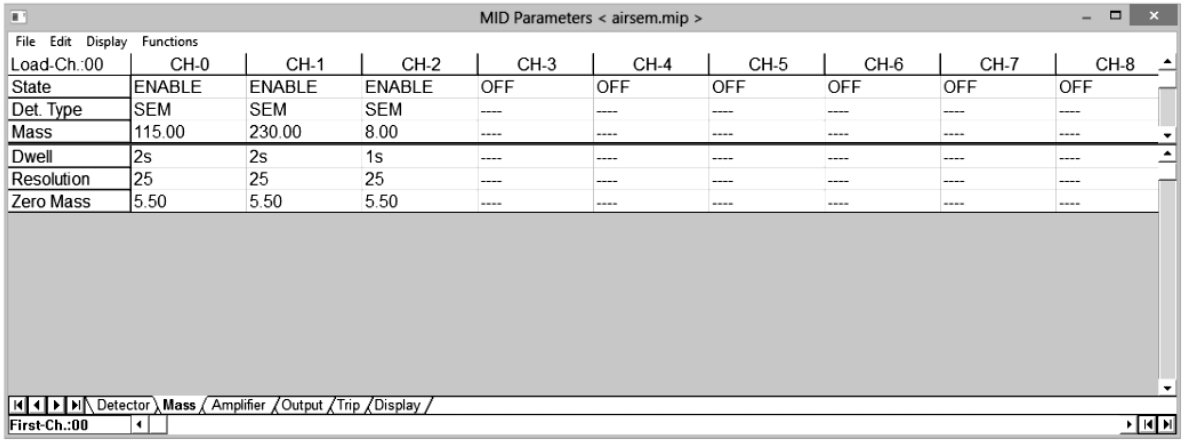

(b) Mass

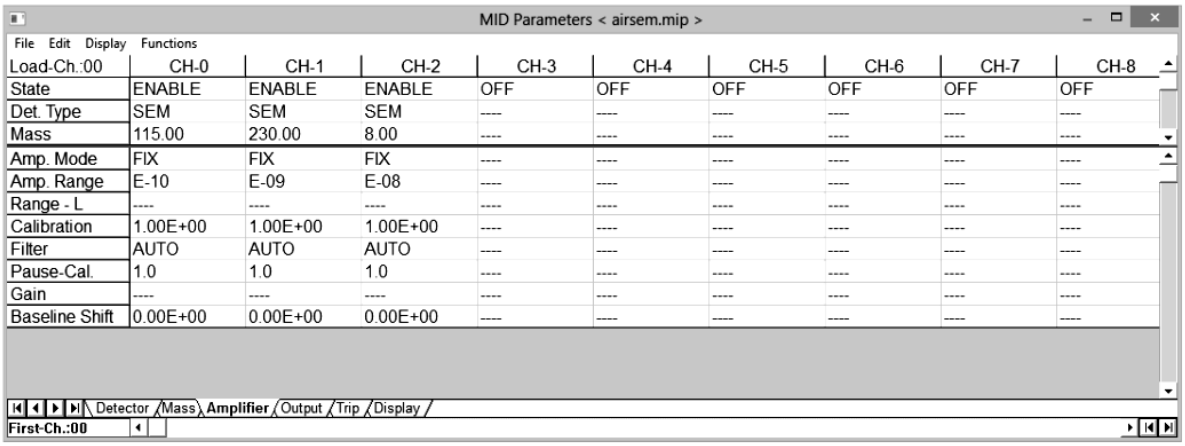

(c) Amplifier

Figure 2.15: Quadstar measurement parameters. Values set are typical for experiments with indium in SEM operation and electrometer ion current detection.

2.5.3 Debugging

Rod potential adjustment [25]

Here a standard procedure for adjusting the rod potentials is presented. This adjustment is typically necessary when spectra look suspicious, e.g. frayed peaks, unfamiliar line broadening or wrong calibration.

1. Start with the values which previously yielded good results, with the values in the manual or otherwise with the values of the above tab. 2.6.
2. Increase the Field Axis value by 1.5 V.
3. Increase the parameter Resolution by ca. 15 % .
4. Alternately adjust Focus and Extraction to the maximum peak level.
5. Decrease Field Axis until the peak level drops by ca. 10 % and assess the peak shape and resolution.
6. Adjust the Resolution so that it just suffices for the intended purpose. If the resolution is set higher than necessary, the sensitivity and stability may be reduced.
7. If the peak shape is unsatisfactory (spikes, tailings), try to improve it by lowering the Field Axis.
8. Try to improve the sensitivity by gradually ajusting the IonRef setting in steps of 5 V. After each step, readjust all other parameters. Proceed systematically and record the parameter settings with the corresponding peak levels and shapes.
9. Repeat the procedure for the second cathode. After activating the cathode, wait until thermal stability is reached. If the sensitivity of the two cathodes is quite different, there might be mechanical deformations.
10. Exchange the RF cable polarity, optimise and compare results for both polarities.

Hardware failure

The modular structure of the system and the fact that other groups in-house have similar systems, such as the helium scattering group (Anton Tamtögl) and the group of Robert Schennach, allows for a systematic approach with the exclusion principle. In this section the systematic exchange of the single components and corresponding tests are suggested.

1. **Software failure:** Before proceeding on to Hardware, better double check the software. One can choose between the original software Quadstar 422, LabView and Matlab scripts (see above in the Description of the Controller) to do so. It is heavily advised to omit the LabView script for the sole purpose of debugging, yet the wiring scheme might provide some basic insight.

2. **Rod potentials:** Check the rod potentials and readjust them according to the procedure described above if necessary.

3. **SEM:** The functionality of the SEM can easily be tested by switching to Faraday mode. In addition one can measure the output voltages (Attention: High Voltage!).

4. **Counter (CP):** Exchange the counter with the electrometer. A detailed description how this is done step by step is provided in the manual.

5. **Electrometer (EP):** Exchange the electrometer with the counter (only in SEM-mode). A detailed description how this is done step by step is provided in the manual.

6. **RF-Generator (QMH):** The RF-generator is a difficult matter. The simplest possibility is to exchange it with another device. Again, comparing set voltages with measured ones might provide some insight. Note that the mass selection in the ion trap is controlled not by the radio frequency on the quadrupole but by the ratio of the DC- to the superposed AC-voltage, and that the operating voltages of the RF-generator must match the specifications of the QMA.

7. **Controller (QMG):** This unit consists of three modules which can be exchanged separately. A test of the output pins is advisable.

8. **Analyser (QMA):** This is the worst case since one has to vent the MC. The rod potential adjustment procedure described above might provide insight whether the cathode is mechanically deformed. It is likely that a solution can only be achieved by the Pfeiffer company.

2.6 Vacuum system

This section provides documentation and characteristics of the vacuum system.

2.6.1 Description

A detailed sketch of the system is drawn in fig. 2.1. Technical data of the pumps and pressure gauges is listed in tab. 2.7 and 2.9.

Table 2.7: Technical data of pressure gauges
abbr. ... abbreviation according to fig. 2.1

abbr.	method	type	controller	Inv. No
$p_{pre,SC}$	pirani / cold cathode	Balzers PKR 250	TPG 362	0147300
$p_{pre,MC+PU}$	pirani / cold cathode	Balzers PKR 250	TPG 362	0147300
p_{SC}	pirani / cold cathode	Balzers PKR 250	TPG 261	-
p_{PU}	pirani / hot cathode	Balzers PBR 260	TPG 261	-
p_{MC}	hot cathode	-	Granville-Phillips 350	-

2.6.2 Vacuum characteristics

Each chamber's base pressure and some characteristic vacuum pressures of the SC during operation are listed below in tab. 2.8 to 2.11. The base pressures have been proven to be quite steady over time as observed with the remote monitoring system (sec. 2.6.4). Upon opening valve V_1 between SC and PU during operation of the SC at $p_{He} = 40$ bar and $T_{CH} = 17$ K the pressure in the PU jumps to some E-07 mbar. During heat-up of the PU up to ca. 600°C the (background) pressure rises steadily up to some E-07 mbar. In the experiment both effects add up. The PU and SC usually do not influence the vacuum of the MC significantly. Typical pressures during bake-out are listed in tab. 2.14.

Table 2.8: Chamber base pressures

Chamber	base pressure / mbar
SC	2E-06
PU	<5E-10
MC	5E-10

Table 2.9: Technical data of vacuum pumps
abbr. ... abbreviation according to fig. 2.1

abbr.	type	name	controller	controller panel	Inv. No
PP_{SC}	rotary vane	Edwards XD535i	-	-	0147337
PP_{MC+PU}	rotary vane	Edwards nXDS15i 100/240V	-	-	-
TP_{SC}	turbo	Adixen ATH 2800M	ATH 2800/3200M	Adixen Mag Power	0147333
TP_{PU}	turbo	HiPace 300	TC 400	DCU 310	-
TP_{DPS}	turbo	TPU 060	-	Balzers TCP 121	-
TP_{MC}	turbo	HiPace 700	TC 400	DCU 400	0147299
TP_{TOF}	turbo	HiPace 80	TC 110	DCU 110	0147303
MP	membrane	Vacuubrand MD4T	-	-	-

Table 2.10: Some characteristic SC pressure gauge values and turbo pump driving current I for different nozzle temperatures T and helium stagnation pressures p_{He}.
[LBE: First six measurements; 20/03/2017, all others: 15/11/2017]

p_{He} / bar	T / K	p_{SC}/ mbar	$p_{pre,\,SC}$/ mbar	I / A
10	12	2.25E-5	2.9E-1	1.20
10	13	2.18E-5	2.9E-1	1.20
10	15	2.12E-5	2.8E-1	1.20
20	12	5.43E-5	5.5E-1	1.60
20	13	4.91E-5	5.1E-1	1.60
20	15	4.35E-5	4.7E-1	1.50
20	16	4.10E-5	3.31E-1	1.40
20	17	3.96E-5	3.21E-1	1.40
20	18	3.76E-5	3.14E-1	1.40
20	19	3.72E-5	3.11E-1	1.40
20	20	3.67E-5	3.08E-1	1.40
40	15	1.24E-4	5.67E-1	1.70
40	16	1.19E-4	5.56E-1	1.70
40	17	1.05E-4	5.35E-1	1.60
40	18	1.07E-4	5.30E-1	1.60
40	19	1.04E-4	5.20E-1	1.60
40	20	1.01E-4	5.11E-1	1.60

Table 2.11: Some characteristic SC pressure gauge values and turbo pump driving current I for different stagnation pressures p_{He} at a constant nozzle temperature of 13 K.
[LBE:20/03/2017]

p_{He} / bar	p_{SC} / mbar	$p_{pre,\,SC}$/ mbar	I / A
10	2.2E-5	2.9E-1	1.2
20	4.9E-5	5.1E-1	1.6
30	1.3E-4	7.3E-1	2.0
40	2.4E-4	9.2E-1	2.4
50	4.3E-4	1.1E-0	2.8

2.6.3 Venting & evacuation procedures

In this chapter step-by-step-procedures for the venting of each chamber are recommended.

Source chamber

1. Make sure the CH is turned off and the nozzle is at room temperature.
2. Close V_1.
3. Turn off turbo TP_{SC}.
4. Wait until turbo is standing still. This might take a while.
5. Shut down PP_{SC}.
6. Access via the side flange opposite of the optical table.
7. Evacuation is straightforward:
8. Seal the chamber.
9. Turn on PP_{SC}. When proper prevacuum is reached, turn on TP_{SC}.

Main chamber

1. Make sure the current or voltage sources for MCP, repeller, magnetic bottle as well as the MC ion gauge and QMS system are turned off.
2. Precautiously set room climate to very low humidity to protect the MCP.
3. Close valve V_2.
4. Turn off turbos TP_{QMS} and TP_{MCP}, be aware that these two pumps are on the same prevacuum line as the PU+DPS. Simultaneously close valves V_{QMS} and V_{MCP}.
5. Wait until turbos are standing still.
6. Untighten the screws of the big flange opposite of the laser entrance window for safety reasons. The pressure difference will prevent uncontrolled venting. This works best with Viton gaskets, but proved applicable with copper gaskets too.
7. Attach the vacuum pipe T-crossing with the two shut-off valves. Attach the membrane pump MP to one arm and an inert gas (Ar, He, N_2) to the other as depicted in fig. 2.1.
8. Flush the pipes: Vent the pipes with the inert gas, then close the valve connecting to the gas. Open the valve to the MP and flush. Close valve to MP and vent with gas again. Repeat twice.
9. $*$ Turn off the ion gauge to prevent an oxidation of the cathode under atmosphere.
10. $*$Slowly vent the MC with the inert gas using the gas inlet. The loose flange will slowly detach and release excess pressure. It is important to not expose the MCP to atmosphere for too long as water adsorption might destroy it. If the TOF is not detached, it will stay filled with gas lighter than air and the MCP won't be exposed to the atmosphere.
11. In case of detaching the TOF is desired, first detach the thermocouple. Don't forget to quickly test its functionality upon reassembly.
12. Conduct your business.
13. Exchange copper gasket ring.
14. Reattach flange, tighten screws.
15. $*$Close valves V_{DPS} and V_{PU}.
16. $*$Open valves V_{QMS} and V_{MCP} while observing pressure.
17. Wait until a prevacuum suitable for the turbos is reached.
18. Turn on turbos TP_{QMS} and TP_{MCP}.
19. $*$Open valves V_{DPS} and V_{PU} while observing pressure.
20. Cover flange in aluminium foil again.
21. Start bake-out procedures as described in sec. 2.6.5. It is sufficient to limit the bake-out to the MC subsystem. Further it turned out to be sufficient to end the bake-out and let start the cool down on the very same evening or during the night using a time switch.
22. The spectrometer is ready again for operation after cool down.

Alternatively one can conduct the venting procedure via the PU with an open valve V_2. Note that in this procedure it is important to open V_2 at the beginning of the procedure.

Pickup chamber

This procedure is described more accurately for the most frequent case of a required oven refill in sec. 2.3.3.

2.6.4 Remote monitoring

All pressure gauge signals are read and transferred to a Raspberry Pi, enabling time traced pressure monitoring via the URL `https://fexphrpifslab.tugraz.at/oversight`. For detailed documentation read the Master's thesis of Stefan Cesnik [19].

2.6.5 Bake-out procedures

The equipment for the bake-out consists of

- 4 variable ratio transformers
- 4 heating bands
- 13 thermocouples for monitoring

and is implemented into the setup as follows shortly.

Attention - possible dangers

Before any bake-out it is important to get familiar with some risks. The repeller's Neodym magnet's Curie temperature is 80°C and must not be exceeded. Further temperature limits apply to the MCP and the solenoid's magnet wire coating as it may evaporate and cause a short-circuit or adsorb to the MCP. Both gas valves' at the PU and the MC and the vacuum valves' V_1 and V_2 gasket rings may become porous and thus leaking if exposed to temperatures above 200°C. The turbo pumps are safe for temperatures of up to 100°C provided they are supplied with sufficient water cooling. The SEV's and QMA's electronics might not be affected for temperatures up to 100°C, nevertheless the QMS should, just like the TOF, generally not be operated during bake-out.

The heating bands are wrapped around the chambers such that a most homogeneous and complete surface covering heating is achieved. To this end the chambers are wrapped in two layers of aluminium foil to create an air buffer, further spreading the heat. A detailed description of the heating band wrapping can be found in fig. 2.16 on p.37 with the corresponding tag name list tab. 2.12. For baking with the recommended transformer settings outlined in tab. 2.13 some typical temperatures (tab. 2.12) and pressure measurements compared to the base pressures (tab. 2.14) are documented.

Apart from the heating bands, 30W halogen lamps inside the PU and the DPS have been installed for additional radiation heating of the inside surface. Unfortunately, no sufficient temperature increase could be measured with the outside TCs nor with the TC attached to the PU cup. Therefore the halogen lamps are obsolete.

Beneath the aluminium foil thermocouples are attached to the chambers in order to monitor the bake-out process. The recommended technique of TC attachment is to stick a strip of kapton to the chamber, and fix the TC with a kink at its end onto the ground strip with another strip of kapton. The kink improves the resilience to mechanical stress of this rather loose attachment and the double kapton prevents body contacts and short circuits. Kapton has the advantage of being suitable for the temperatures desired but eventually will dry up and lose its adhesion.

Objects of special interest are gaskets, turbo pumps, the magnetic bottle and any electric circuitry or measurement device in proximity or attached to the vacuum chambers. Further important indicators are heating band crossings which are expected to be hot spots. Those critical and/or hot spots have been identified and thermocouples attached to them. Any critical point must not exceed the maximum temperature specified for the device in its proximity, though practically a maximum temperature of 100°C is sufficient to get rid of the main pollutant water. Furthermore, in order to reduce risk of heat damage, all turbos have been supplemented with a serial water cooling circuitry. The critical points are further outlined as follows:

The bake-out parameters provided below are well documented and reliable. Using the specified configuration, one can do the bake-out over the weekend with confidence, although it is advised to start the procedure on Friday early afternoon and check for equilibrium. A timer clock can be set to shut down shortly before Sunday midnight, making the machine operational again till Monday morning. Until now, 2.5 days of baking have proved to be sufficient to achieve base pressures of some E-10 mbar in both chambers MC and PU. Nevertheless, the first bake-out after any relevant modification of the system should always be under supervision, i.e. monitoring the TCs.

Finally, some parts of the system are not baked properly. These particularly exposed and poorly pumped regions are the pipe from the PU to the gas inlet valve and the bellow connecting SC and PU. The device of choice is a hot air gun. As there are no permanent TCs attached to these spots, one should do so before. Due to the tremendously high heat flux of the hot air gun, one has to carefully monitor the temperatures as well the pressure gauges in both PU and SC. The gasket in valve V_1 and the gas inlet valve at the PU must not be damaged. Not exclusively but especially at the spot where the gas inlet pipe pierces the PU top flange and at the swagelock screw nut connecting pipe and gas inlet valve, too rapid heating can lead to significant leakage and accidental venting. It is sufficient to observe the pressure gauges and immediately turn off the hot air gun as soon as the pressure increases rapidly.

Table 2.12: Characteristic thermodynamic equilibrium temperatures measured with the thermocouples at the points documented in fig. 2.16 on p.37 during bake-out with parameters set as in tab. 2.13. Spot 13 and any other not listed spots turned out to be neither a hot nor a critical spot.
No. ... Number of the thermocouple as depicted in fig. 2.16
TC tag ... name tag attached to the thermocouple
T ... typical temperature at thermodynamic equilibrium with the bake-out parameters outlined in tab. 2.13

No.	TC tag	T / $°C$
1	Solenoid	113
2	Repeller unten	83
3	TOF MCP	114
4	TOF Turbo	37
5	MC Mitte	110
6	MC Vakuummessröhre	115
7	PU oben	76
8	PU Mitte	92
9	DPS Mitte	100
10	DPS oben	129
11	QMS SEV	79
12	QMS Turbo	62

Table 2.13: Recommended configuration of transformers for the heating bands, tags as documented in fig. 2.16 on p. 37, and the solenoid current I

TOF+Repeller/ %	QMS / %	MC+DPS / %	PU+DPS / %	I / A
50	45	45	45	1.5

Table 2.14: Characteristic base pressures and pressures at equilibrium temperature during bake-out with parameters set as in tab. 2.13. Note that these pressures are expected to be lower in case of baking merely a subsystem (MC or PU).

	p_{MC} / mbar	p_{PU} / mbar	$p_{pre,MC+PU}$ / mbar
base pressure	5.0E-10	<5.0E-10	9.2E-04
bake-out	6.9E-08	4.3E-07	9.7E-03

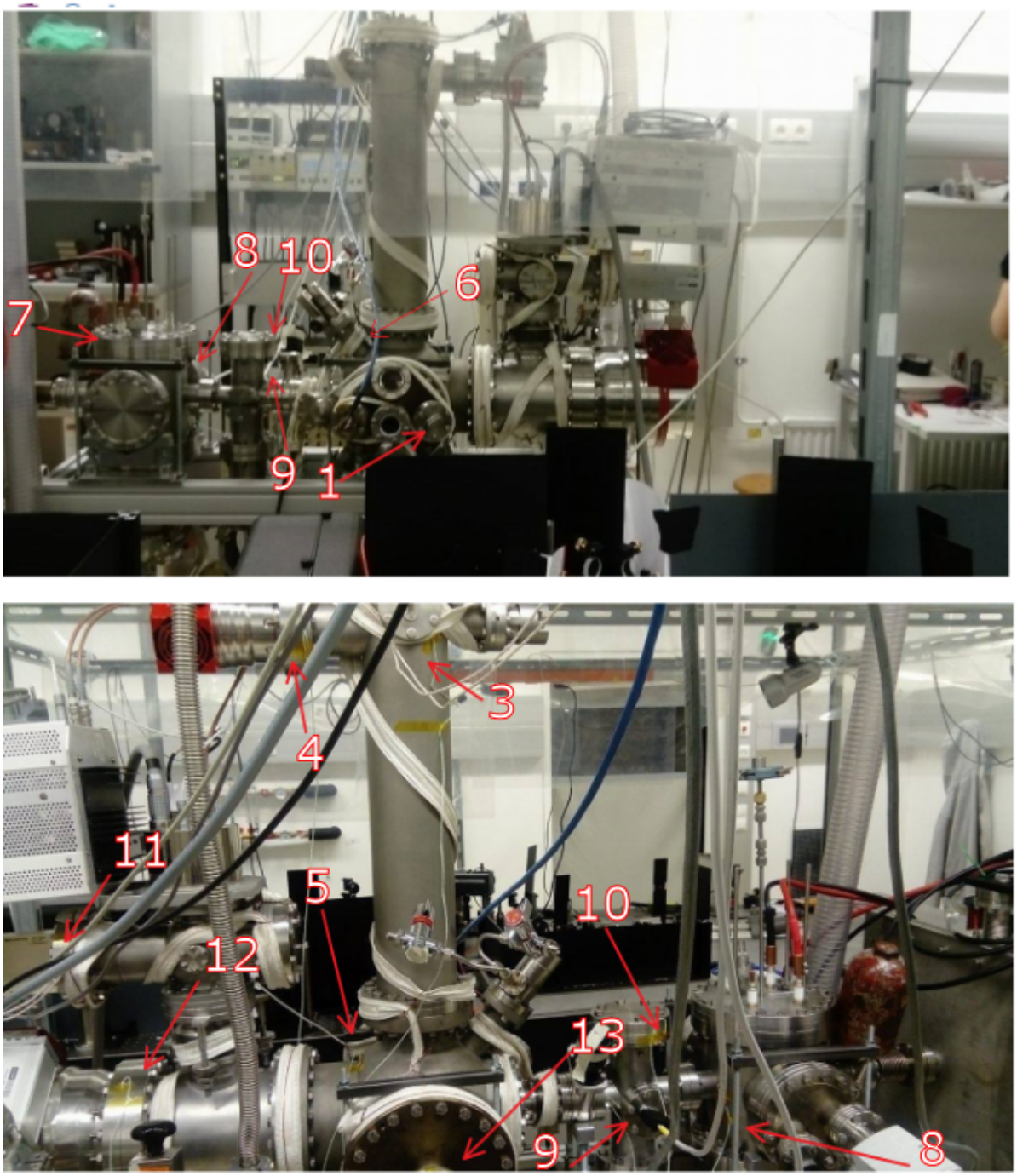

Figure 2.16: Photo-documentation of the attachment of the heating bands and thermocouples to the chambers. Heating band 'TOF+Repeller' starts on the MCP's flange and goes straight down to the repeller's voltage supply flange. Heating band 'QMS' starts at the SEV, wraps the QMS flange and ends at the big flange opposite of the laser beam entrance window. Heating band 'MC+DPS' starts at the flange connecting DPS and MC and wraps the small flanges near the laser beam entrance window. Heating band 'PU+DPS' wraps the PU and the DPS. The locations of the TCs are indicated by the red arrows and their tag names listed in tab. 2.12 on p.36. Not visible is the TC attached to the outside of the repeller onto the flange connecting to the repeller adjustment plate (spot 2) as well as the TC inside the TOF attached to the solenoid right above the repeller. For the latter the access point is indicated instead (spot 1). Spot 13 and any other not listed spots turned out to be neither a hot nor a critical spot.

2.7 Vacuum failure emergency shut-down system

A sudden pressure rise in the SC, e.g. due to a big leak or a prevacuum pump blackout, is a major threat to the setup. First of all, mechanical damage or destruction of the turbo is inevitable, secondly the coldhead nozzle is expected to freeze up and clogg with ice. In order to mitigate the risk, an emergency shut-down system was employed, which simply turns off the turbo in a controlled manner and cuts the power supply of the compressor in case the gauge indicates a pressure rise. Originally the compressor was meant to be turned off in a controlled manner too, but insufficient documentation of the compressor controller's wiring due to its old age made this impossible. The circuitry is documented in fig. 2.17 on p.39 and described in detail in the text below. For the turbo controller Magpower to enable remote control, pins 37 and 38 must be connected, and to enable input the pins 39 and 40 must be connected (fig. 2.17d, fig 2.17b). Pin 32 is the switch 'Turbo ON/OFF', where the pin being grounded corresponds to 'ON'. As soon as Pin 32 is not grounded, e.g. by using the switches EXT or SP1, the controller shuts the turbo down. Additionally, upon loosing ground, the contactor cuts the heavy-power current supply (3F3) of the compressor. EXT is an external mechanical switch, see photograph in fig. 2.17c, with a green light glowing if it is disconnected, i.e. the monitoring being active in the mode 'AUTO'. Connecting EXT to GND, i.e. setting the switch to 'OFF', shuts the whole system down. 'ON' simply bypasses the emergency system. Note that the order of the switches is actually AUTO-OFF-ON as labeled in fig. 2.17c, and hence switching from active monitoring to bypass needs to be done quickly in order to avoid an unintended shut-down. Switch SP1 (Set Point 1) is built in the gauge controller TPG 361 and flips from Pin 4 to Pin 2 as soon as p_{SC} exceeds the threshold parameter 'SP1-Low'. Vice versa, SP1 flips from Pin 2 to Pin 4 as soon as p_{SC} falls below the threshold parameter 'SP1-High' again. The current values of 'SP1-Low' are 1.0E-03 mbar and 1.1E-03 mbar, respectively, and can be set by pressing the buttons on the gauge controller front panel as follows: *Para* (switch to parameter mode) → *Up/Down* (scroll through parameters) → *Para* (edit parameter) → *Up/Down* (increase or decrease value) → *Para* (confirm).

2.8 Assembly & beam alignment

Prior to the final steps of the assembly it is crucial to align the He beam path. The parameters are horizontal and vertical position as well as tilt angles of SC, PU, DPS, TOF and the QMS filament. It proved feasible to detach TP_{QMS} and position a telescope along the extended He beam path, such that it lies exactly on one axis with skimmer and QMS ionisation chamber via iterative translating and rotating. The goal is to align the chambers along one axis such that the telescope's cross hair centres the QMS ionisation chamber and all four apertures as well as the skimmer. The apertures can be made visible by daylight for the last aperture DPS-MC, by two permanent halogen lamps inside the DPS and PU each, and a temporary LED attached to the SC nozzle. To distinguish the apertures more easily, one might drive the halogen lamps with different currents for different brightness. To this end, the PU and the DPS were moved via the stayers such that both apertures in the DPS and PU as well as the cooling shield in the PU were on one axis with the telescope. In order to achieve a sharp focus on the QMS ionisation chamber one might need a focus shortening lens for small distances. Consider that the picture is upside down and flipped, i.e. an aperture appearing to be outmost right needs to be shifted to the right.

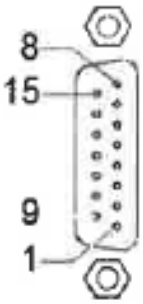

(a) Pin assignment of the female TPG-361 15-pin D-Sub appliance connector.

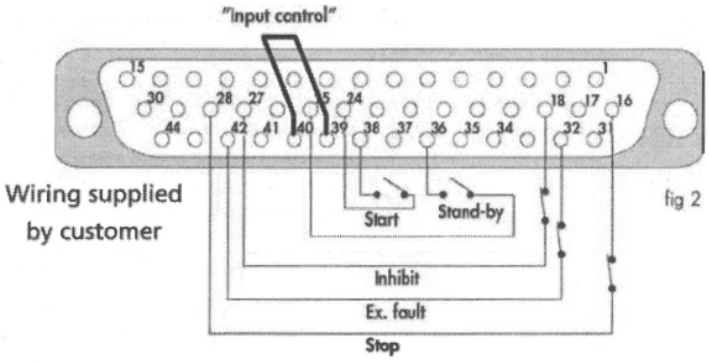

(b) Pin assignment of the female Magpower 44-pin D-Sub appliance connector. Control by dry contacts with 'input control' mode.

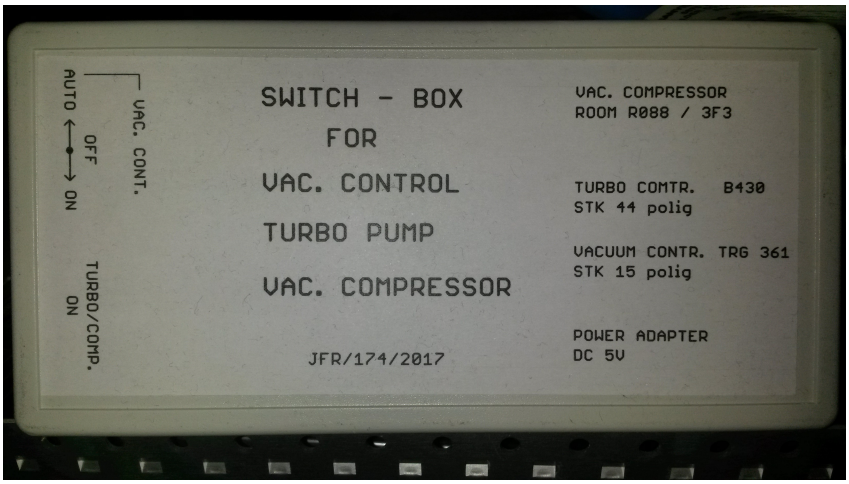

(c) Casing of the switch EXT as described in (b).

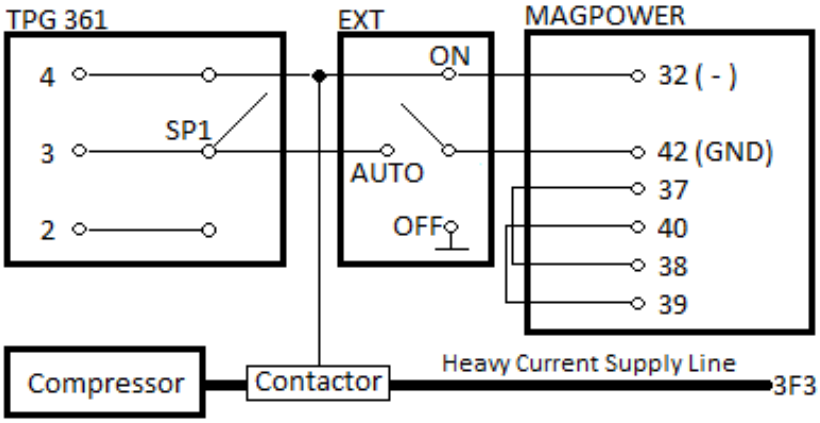

(d) Sketch of the wiring of the emergency shut-down system.

Figure 2.17: Documentation of the emergency shut-down system.

2.9 Characterisations

Subsections 2.9.1-2.9.2 are descriptive measurements of the helium apparatus itself, while subsections 2.9.3-2.9.4 characterise some issues linked to the laser source.

2.9.1 He_N beam diameter

The He beam diameter is of particular interest as it is directly related to the sensitivity of the signal strength with respect to variation of the exact spot of ionisation, i.e. laser alignment. Its characterisation measurement is documented in detail in tab. C.1 in the appendix and the diameter calculated in fig. 2.18 by subtracting the background from the total signal in said table. The result of a 2-3 mm diameter accounts for an insensitivity to small laser beam alignments in z-direction.
The experimental conditions were a stagnation pressure of 40 bar, nozzle temperature of 15 K, the temperature resistively measured was 700°C, 395 nm wavelength achieved with a 5 mm LBO crystal. The laser power was held at 90 mW with a focus diameter (FWHM from beam profiler) of $(70 \pm 10)\ \mu m$. In this early setup, no separation of the second harmonic from the residual fundamental has been conducted. The measurement points were limited to the displayed z-positions by the repeller geometry.

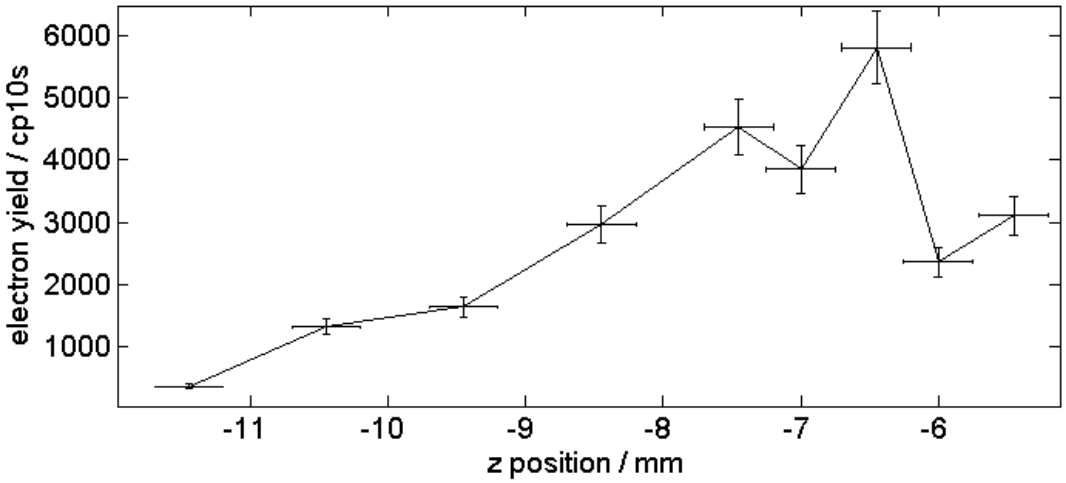

Figure 2.18: Single pulse netto electron yield dependent on the repeller position in z-direction. x- and y- direction have been optimised to signal strength. Data obtained from tab. C.1 by subtraction of effusive background from total yield. [LBE:03/04/2017]

2.9.2 Pickup statistics

The pickup statistics are important in terms of signal strength. The variational parameters are the stagnation pressure, the nozzle temperature and the pickup temperature. The first two parameters control number and size of He droplets, thus the pickup volume. The last parameter controls the indium vapour pressure the He_N pass through and hence the pickup probability. The pickup of k atoms, i.e. the collision of a drop with k In atoms and their subsequent confinement, obeys Poisson statistics. Various simultaneous processes compete and the optimal conditions are a delicate matter. A detailed description of the drop formation and doping process can be read in chapter 1.3 of the Dissertation of Markus Koch, [22] with particularly useful formulae in sec. 1.3.3 for mean droplet sizes dependent on the parameters mentioned above and furthermore measures such as orifice diameter and the speed of sound. Additionally, a list of values characterising the underlying size distributions, such as mean drop size, variance and most probable drop size, each calculated for various nozzle temperatures and stagnation pressures, can be found in the appendix A.1 of the Dissertation of Florian Lackner. [29]

Nozzle temperature

Lower nozzle temperature leads to larger, but consequently also fewer He nanodroplets. The former effect increases the pickup probability because the pickup volume increases. Yet the decreased number of drops leads to a decreased signal strength. Further, larger droplets shift the pickup temperature cutoff, due to droplet destruction, to higher pickup temperatures.

Stagnation pressue

This parameter will not be of interest until larger droplets are desired.

Pickup temperature

This parameter controls the In vapour pressure. The relationship is superexponential (see fig. 2.7) and therefore hypersensitive. The pickup temperature has to be high enough such that a sufficient pickup probability is ensured. With increasing pickup temperature, apart from the single-pickup, also the double-pickup or in general multi-pickup probability is increased. In some regimes the increase of the multi-pickup probability is higher than increase of the single-pickup probability, depending on droplet size. This is specifically a problem if some X_n species do spectrally overlap. In this special case it was found that the most interesting He_NIn ground to 1st excited center state excitation (ca. 365 nm) spectrally overlaps with excitations of He_NIn_2 . Apart from that, it might be advisable to go to higher temperatures at first before cooling down again in order to get rid of oxides on the melt's surface.

Droplet destruction

This effect is due to the total destruction of the droplet by complete He evaporation upon pickup and depends on the actual droplet size distribution and In atom kinetic energy distribution and pressure via the n-pickup probability, as each dopant's thermalisation costs a specific amount of He atoms to desorb. The effect can be observed as a rapidly dropping He_2-signal (see tab. C.2) in the QMS because all droplets are destroyed on their way. Further, the He_NIn electron yield decreases in comparison to the effusive background.

Pickup statistics - characterisation

In fig. 2.19 the netto ion yield at 395 nm excitation and ionisation wavelength is calculated from tab. C.2 in the appendix by subtraction of the effusive background from the signal (yield). The experimental conditions were a stagnation pressure of 40 bar, nozzle temperature of 17 K, 395 nm wavelength with a 5 mm LBO crystal. The laser power was held at 140 mW with a focus diameter (FWHM as measured with the beam profiler) of $(70 \pm 10)\ \mu m$. In this early setup, no separation of the second harmonic from the residual fundamental has been conducted.
Above a certain temperature the signal strength even decreases due to a shift of the Poisson distribution to multiple pickup events and droplet destruction. In this regime most of the material is evaporated. As deduced from the vapour pressure curve (fig. 2.7), every 50°C account for one order of magnitude in pressure. Thus e.g. operating at 640°C ensures 10 times as many operating days before oven refill is required as operating at 690°C, provided the working point delivers sufficient electron yield. Apart from that, the effect of droplet destruction as discussed in sec. 2.9.2 can be observed via the ratio of $He_N In$ electrons to effusive background electrons as well as the dropping number of He_2 observed in the QMS, documented in said tab. C.2 in the appendix. More investigations considering pickup statistics can be found in fig. 3.3 and 3.7.

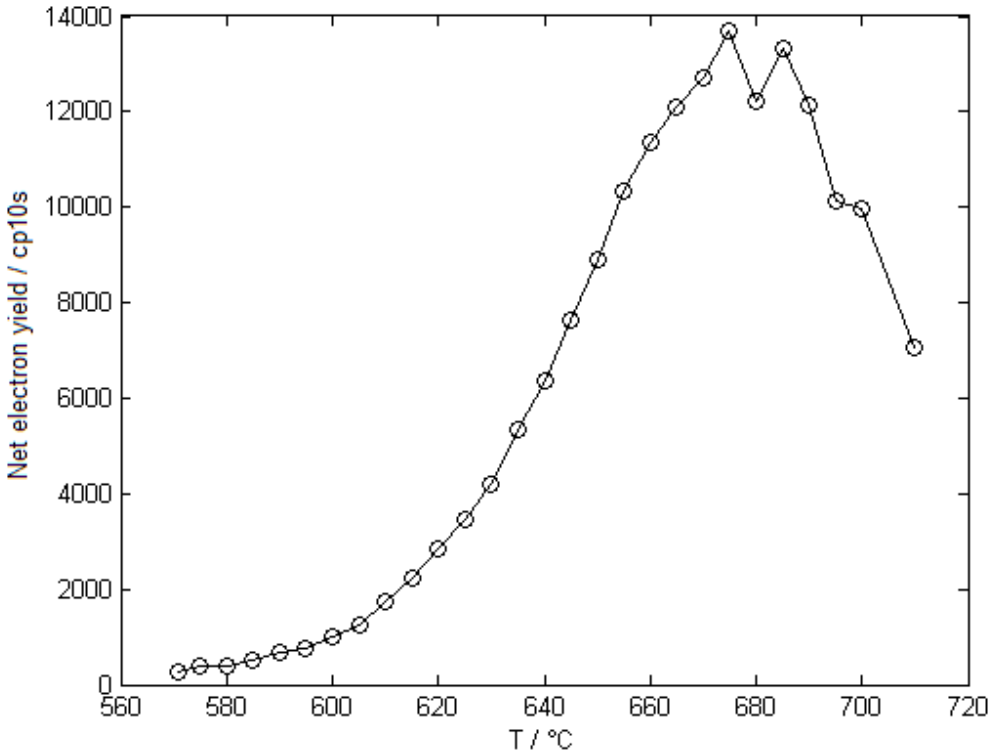

Figure 2.19: Netto electron yield (counts per 10 second) versus the pickup temperature as measured with the thermocouple according to tab. C.2 at 395 nm excitation and ionisation wavelength. The netto yield is calculated by subtracting the effusive background from the total yield in tab C.2. A working point on the left flank is advised as best trade off between signal strength, contrast and material consumption presuming the momomer is of special interest. One might further be interested in fig. 3.3 and 3.7. [LBE:04/04/2017]

2.9.3 Laser power dependency

The major insight is, that at a laser beam diameter of $(70 \pm 10)\ \mu m$ and a wavelength around 395 nm, one does not expect undesired Multi-Photon-Ionisation (MPI) processes. Further, an upper limit of the laser beam diameter, corresponding to the largest ionisation volume limited by the He beam diameter of 2-3 mm (see sec.2.9.1), can be concluded.
One can tackle MPI-processes and gain signal strength by increasing the laser beam diameter up to a larger ionisation volume while simultaneously increasing the laser power. This can be done by shifting the focal point away from or towards the He_N beam, or more sensitively with a telescope. When one implements a telescope before SHG, one also affects the conversion efficiency.
The experimental conditions were a stagnation pressure of 40 bar, nozzle temperature of 17 K, the pickup temperature resistively measured was 650°C, 395 nm wavelength achieved with a 5 mm LBO crystal. The laser power was varied with a focus diameter (FWHM as measured with the beam profiler) of $(70 \pm 10)\ \mu m$. In this early setup no separation of the second harmonic from the residual fundamental has been conducted, the conclusions of this chapter still hold though. This circumstance can mislead to false conclusions especially when conducting pump-probe experiments and is discussed in more detail in sec. 5.2.1 and in fig. 2.21.
In fig. 2.20 the effusive power dependence has a higher slope, therefore the process is of higher order, indicating a direct non-resonant two-photon ionisation, just as expected from comparing the wavelength and the bare atom line. Because the slope of the pickup signal is lower than the effusive signal over the whole power range, it can be concluded that the signal from the In inside the helium is mainly, but not exclusively, due to resonant one-photon excitation, followed by one photon ionisation. The absence of kinks in the lines indicates that this is the case in the whole power regime that was investigated.

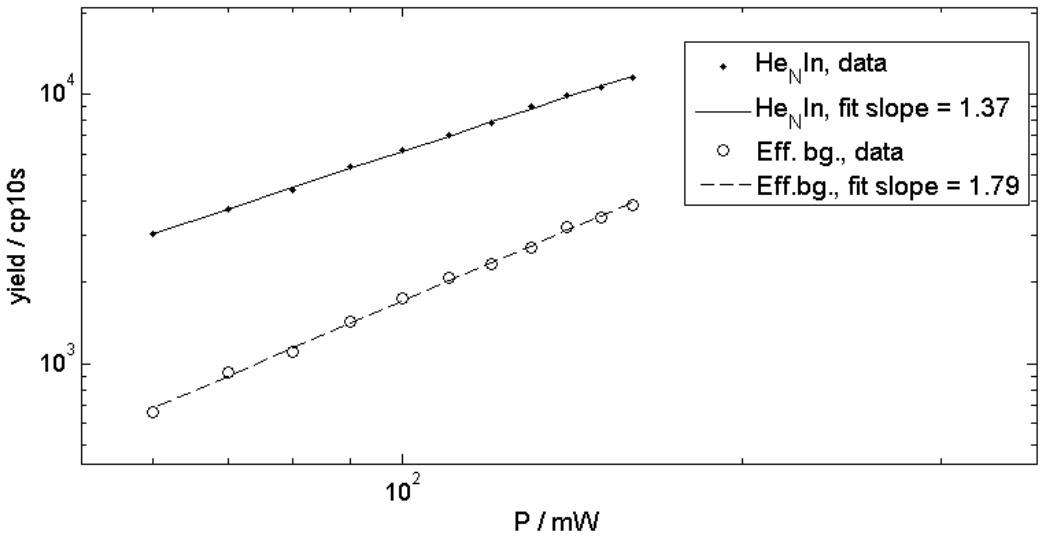

Figure 2.20: Logarithmic total electron yield (counts per 10 second) versus the logarithmic total laser power (mW). Experimental conditions are outlined in the text. [LBE:05/04/2017]

2.9.4 Influence of the fundamental in OPA-SHG pump probe experiments

In the time scan (fig. 2.21 a), apparently two cross-correlation signals appear. These are assigned to the cross-correlations of the pump with the SHG and the residual of the fundamental. According to the group delay dispersion of the 500 μm BBO, the red pulse is expected to be delayed by 1 ps more than the blue pulse, which is verified in the experiment. To characterise possible interferences, PES (b) at the temporal position of the pump-red cross-correlation have been recorded with (red line) and without (blue line) high-pass colour filters. Apparently, the undesired peaks, originating from multi-photon ionisation with 800 nm, are spectrally separated, and furthermore only occur temporally at the pump-red cross-correlation. To avoid possible troublesome future interferences, the problem has been tackled with dichroic mirrors. Further investigations of such ghost cross-correlations are documented in the Master's thesis of Pascal Heim [30].

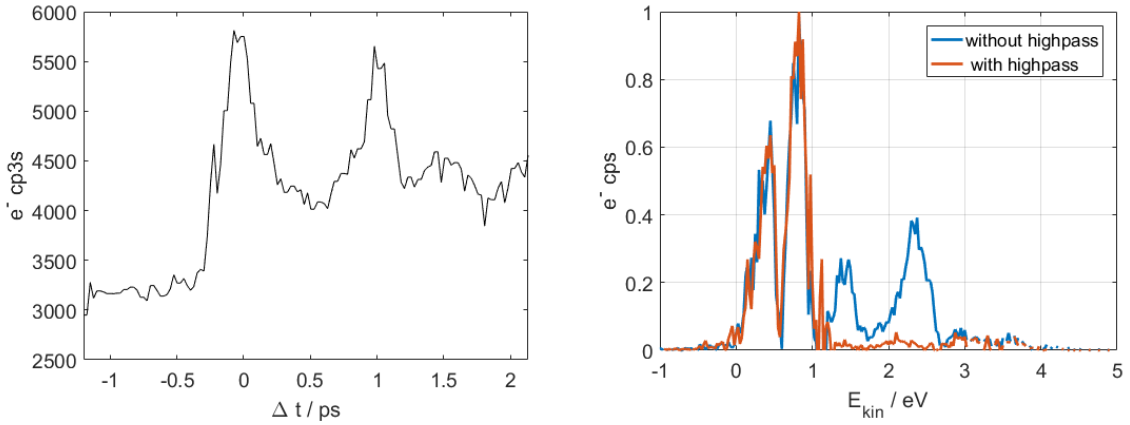

(a) (b)

Figure 2.21: Ghost cross-correlation (a) and characterisation (b) of the influence of residual fundamental laser light. [LBE:18/07/2017]

CHAPTER 3

Results

The findings presented in chapters 3 and 4 will lead to two publications. One will highlight the proof of concept discussed in this very chapter. The second publication will interpret the presented excitation spectrum in the light of the theoretical work contributed by our collaborators. Based upon their work, further calculations are outlined in chapter 4. For a profound comprehension of this chapter fig. 1.2 and fig. 1.3 are crucial.

3.1 OPA-SHG pump-probe experiments

There are several observables available. The most obvious one is the excitation spectrum, i.e. the yield of electrons, integrated over a certain interval of kinetic energy, and ions of different charge-to-mass ratios, being In, In_2 and exciplexes in this case, in pump and pump-probe ionisation experiments. This observable has information about the state of the system prior to excitation, yet none about the temporal evolution. Conclusions about dynamics prior to excitation become apparent when reading chapter 4. Another observable is the yield of electrons of a certain kinetic energy and of ions of a certain charge-to-mass ratio as a function of the time delay between excitation and ionisation pulse. The latter one is not a particularly good observable because ions tend to strongly interact with the helium droplet, invoking possibly undesired dynamics after ionisation, accounting for a difficult or even impossible interpretation of the dynamics after excitation. This becomes apparent in fig. 3.6, from which we conclude and accept that this observable makes us in this case completely blind for dynamics inside the drop, which are on a sub 50 ps timescale which is the timescale actually desired to investigate in this work. The photoelectron spectra (PES) in contrast, being the yield of electrons as a function of their kinetic energy, are the most powerful observable because they allow to determine dynamics happening inside the droplet, a conclusion also made from fig. 3.6. Due to the non-observably weak helium-electron interaction they leave the droplet unperturbed, quite in contrast to ions which tend to get recaptured if the ionisation takes place in proximity to or inside the drop.

This fact is neither trivial nor obvious, but the very milestone of this work. It is a proof of principle that femtosecond time-resolved photoelectron spectroscopy is possible INSIDE the helium confinement, and thus opens the field of femtochemistry inside the cryogenic nano-testbed of helium nanodroplets. Further on, the time scale for photochemistry experiments has been determined for the 1st excited state of indium to 50 ps.

3.1.1 Excitation spectrum disentanglement and the discovery of center & surface states

DFT calculations performed by Ralf Meyer [31] yielded ambivalent predictions whether the captured indium atoms reside inside the drop at the center or in a dimple on the surface of the droplet. The existence of both center and surface states has been proven in the experiment. An OPA wavelength scan was performed with SHG probe, for which the pump-probe total In^+ and $In_2{}^+$ yield as well as photoelectron spectra have been recorded. The pump and pump-probe PES have been integrated in the kinetic energy intervals corresponding to the expected In monomer peaks (fig. 3.2, left peak at 0.4 eV). Examples of these PES for different excitation wavelengths are shown in fig. 3.2. The two major structures at 0.4 eV and 0.6 eV are assigned to In (a, left) and In_2 (a, right) using the PEPICO (b) recorded for 374 nm. The origin of the structure at 0.2 eV is yet unclear. Thus for the excitation spectrum only the left peak has been integrated. Apparently, the dimer band at 363 nm has significant oscillator strength. As shown in fig. 3.2a, the dimer excitation can be mostly avoided by choosing a pump wavelength of 380 nm, which is useful for recording monomer dynamics as outlined in the next section. Still one has to deal with dimer excitations in the excitation spectrum. For sufficient signal strength and contrast, the pickup conditions had to be optimised prior to the experiment. The indicator of choice were PES, and the procedure is documented in fig. 3.3. Starting from the pickup conditions of 17 K and 557°C, first the nozzle temperature was varied, after which the pickup temperature was varied, until the best ratio of monomer peak to dimer peak was found. The best ratio here means a sufficiently strong monomer signal with minimum dimer contributions, i.e. trade off of signal strength and contrast.
The resulting excitation spectrum is shown in fig. 3.1a. The theoretical description of the spectrum follows from the potential energy surfaces in fig. 4.1. The coincidental spectral overlap of the He_NIn center states with some He_NIn_2 states made the recording a challenging task, hence the selective integration intervals in the PES and prior pickup condition optimisation. The different spectral contributions in the excitation spectrum are disentangled as follows. The structure at 370 nm consists of contributions from In_2 on the left flank as well as center states of He_NIn one the right flank, whereas the structure at 397 nm is due to He_NIn surface states. The apparent double structure at 365-380 nm was double checked and is mere noise. Verification of the In_2 contributions is shown in 3.1b-e. The origin of the different blue shifts of center and surface states of He_NIn is discussed in detail in fig. 4.1. The structure at 345 nm can be assigned to In_2 as no In line is expected there, though the origin of the In^+ in 3.1abcde is not entirely clear. They do not result from actual In surely, thus either In_2 or $In_2{}^+$ partially dissociates upon excitation with 345 nm. PEPICO could possibly clarify this in the future. It is further unclear whether both monomers get ejected or one gets re-immersed in the droplet.
Yet there are still some unknown factors in this spectrum. Fragmentation of In_2 after excitation but before ionisation cannot be distinguished from 'original' monomers, neither by looking at ions nor at PES, as fragmented dimers might 'pollute' the monomer assigned PE peak at 0.4 eV. Further investigation with time-resolved PEPICO might shine some light onto this question, provided the fragmentation happens sufficiently far away from the drop.
Latest observations suggested that we might actually deal with a 'collapsing quantum foam', which is currently being further investigated and not discussed in this work.

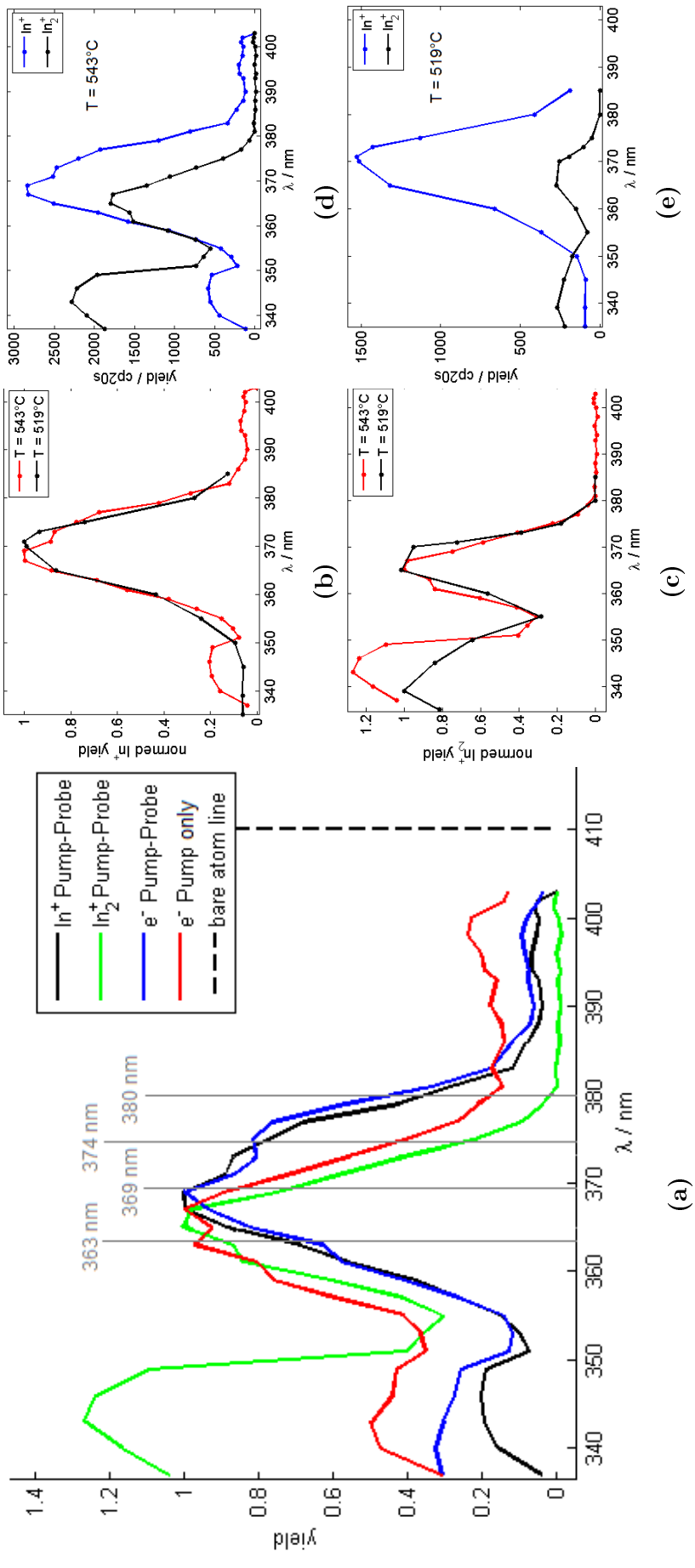

Figure 3.1: Excitation spectrum. Integrated pump-probe ion yield and photoelectron spectra obtained with a 5 mm LBO. Pump and Pump-Probe PES have been integrated selectively over the monomer contributions. Errorbars have been omitted for the sake of clarity. The lines have been drawn to guide the eyes. (a) Integrated pump-probe ion and photoelectron yield spectra. Excitation wavelengths are depicted with black lines for the dimer maximum (365 nm), near the local monomer maximum in electron pump-probe yield (373 nm) and the monomer flank where no dimer contributions occur (380 nm). Comparison of the monomer (b) and dimer (c) for different pickup temperatures and comparison of the pickup temperatures 543°C (d) and 519°C (e) for monomer and dimer. Experimental conditions (a): 18K nozzle temperature, 534°C pickup temperature, SHG Probe with 420 nm, variable OPA pump. Time delay roughly 185 ps. [LBE:(a)13/07/2017,(b-e)17/07/2017]

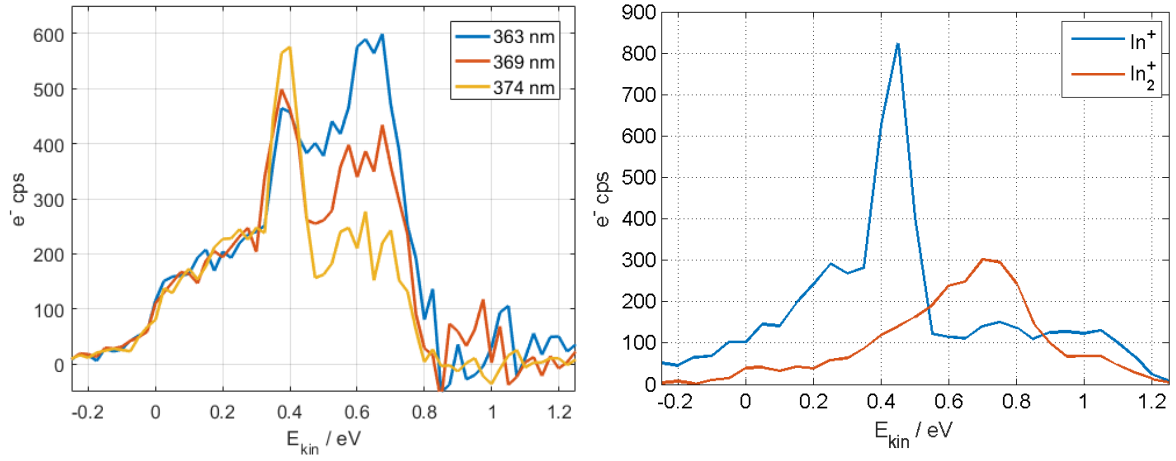

(a) (b)

Figure 3.2: (a) Pump-probe PES for different pump wavelengths probed with 402 nm at time delay of 185 ps. The spectrum is acquired as follows: PES are recorded with both pump and probe path shining into the chamber, then another two PES are recorded with each one of the two paths blocked out. The latter signals are subtracted from the pump+probe signal. (b) PEPICO spectrum entangling the PE contributions from In (blue) and In_2 (red). The acquisition and analysis of pump-probe PES and PEPICO is decribed in more detail in the Master's thesis of Pascal Heim [30] [LBE:14/06/2017]

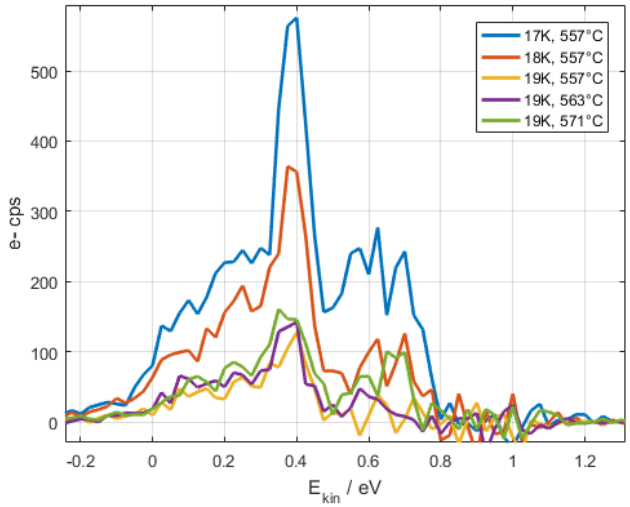

Figure 3.3: Monomer-dimer pickup optimisation PES at a pump wavelength of 374 nm, probed with 401 nm at a time delay of 185 ps. The pump wavelength was chosen according to the peak assignment and ion disentangled electron yield in fig. 3.2a and 3.2b in order to minimise the dimer contributions (0.6 eV) in comparison to the monomer (0.4 eV).[LBE:14/06/2017]

3.1.2 Disentanglement of monomer, dimer and exciplex dynamics

Because special interest is on the monomer dynamics, for now, the different contributions and processes due to the dimer $He_N In_2$, as well as the formation of exciplexes such as InHe, $InHe_2$, $InHe_3$ and so on, have to be disentangled and separated from the monomer dynamics first. This is possible by a systematic variation of the parameter sets of pickup conditions, wavelength variation and time delay and a combined analysis of PES and ion mass spectra.

Fig. 3.4c shows mass spectra at different pickup temperatures. Raising the temperature by just 20°C makes the yields roughly equal, with the monomer yield only slightly higher but doubled dimer yield. At very high temperatures of 604°C, now the dimer outnumbers the monomer. In addition to that, the total signal yield drops, indicating that in this regime a major fraction of droplets is destroyed in the PU already (see sec. 2.9.2 for further explanation). The mass spectra at different time delays in fig. 3.4b show increased exciplex signal at intermediate ionisation times. The time delay of 23 ps in (b, red line) is not d'accord with the signal rise times in (a). This might trace back to the excitation wavelength in (a) being 375 nm and in (b) being 362 nm, which might make the experimental evidence of these considerations obsolete. A more trivial suspicion is that the lab book entry is wrong.
This might be due to a relatively short lifetime of theses exciplexes, meaning they decay shortly after formation and ejection, leading to an intermediate rise and subsequent decrease of signal. Another explanation could be that these increased contributions might actually be no exciplexes but $InHe^+$ ions formed after ionisation of almost ejected In, which is deduced as follows. In the time scan in fig. 3.4a, solely gated to In and He_1In, the intermediate exciplex signal rise at roughly 50 ps combined with its decrease later on to a non-zero value suggests that exciplex forming occurs not only BEFORE ionisation upon In ejection, but there is also another such mechanism AFTER ionisation in a regime where the ion is in a delicate balance between being free or bound to the droplet. Interestingly, according to (b,c), such processes take a minor role involving the dimer, as only the simplest dimer exciplex In_2He might occur. The broad peak structure can partially be assigned to the isotope ^{113}In. ^{113}In with 4.3% and ^{115}In with 95.7% are the only relevant and sufficiently stable isotopes of In. [1]

Ad fig. 3.5, at 345 nm the In_2 band is excited, while no In line is addressed. From this follows that a major part of the In_2 dissociates either in the neutral or in the ion, much in agreement with the conclusions about the excitation spectrum in fig. 3.1a. This fact is further discussed in the last section. At an excitation with 363 nm both monomer and dimer ions appear, the ratio also depending on the pickup conditions, being p_{He} = 40 bar, T_{CH} = 18 K and T_{PU} = 601°C in this experiment. No further conclusions about dimer dissociation can be made solely from this measurement though.

[1] https://en.wikipedia.org/wiki/Isotopes_of_indium

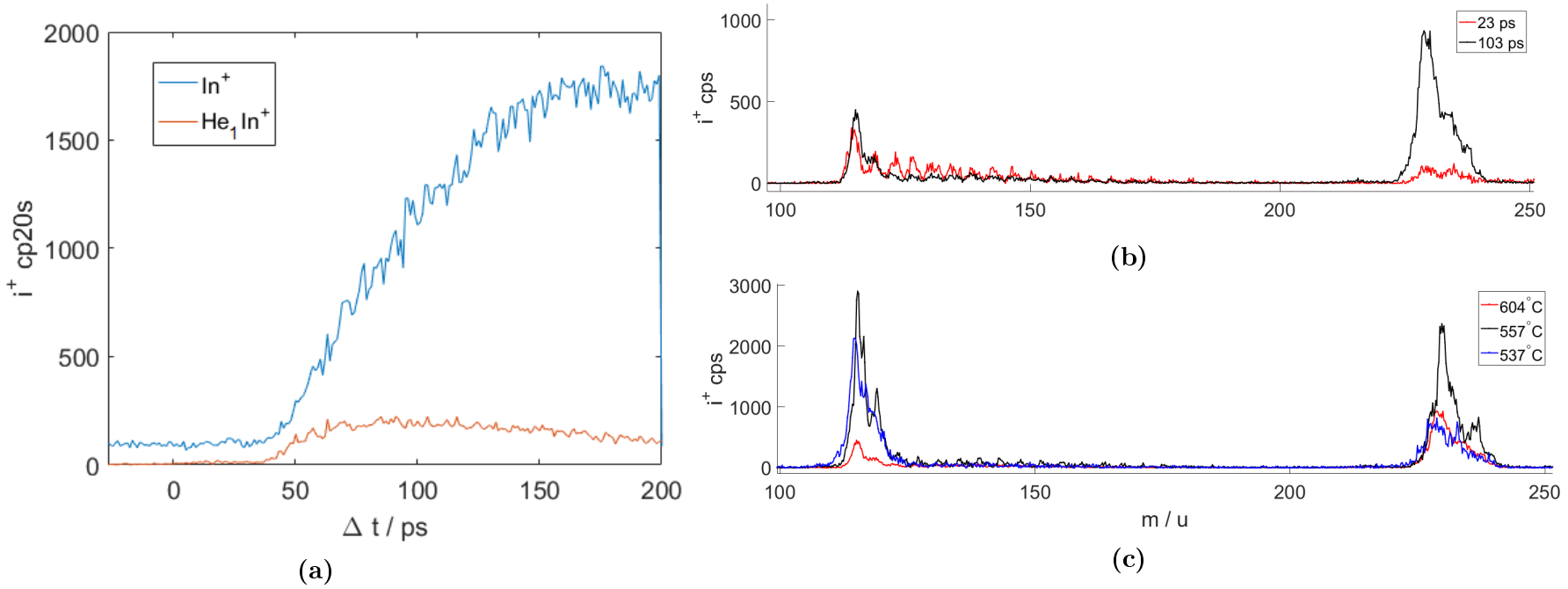

Figure 3.4: (a) Time scan gated for In^+ and the monomer exciplex $HeIn^+$. The gates were determined by using the flight times used to acquire the mass spectra (b,c). Mass spectra are shown for long (103 ps) and intermediate (23 ps) time delays (b) at high temperature (604°C) and for and three representative pickup temperatures (c) at long time delays (103 ps). All temperatures measured with the thermocouple. [LBE:(a)31/07/2017,(b,c)02/06/2017]

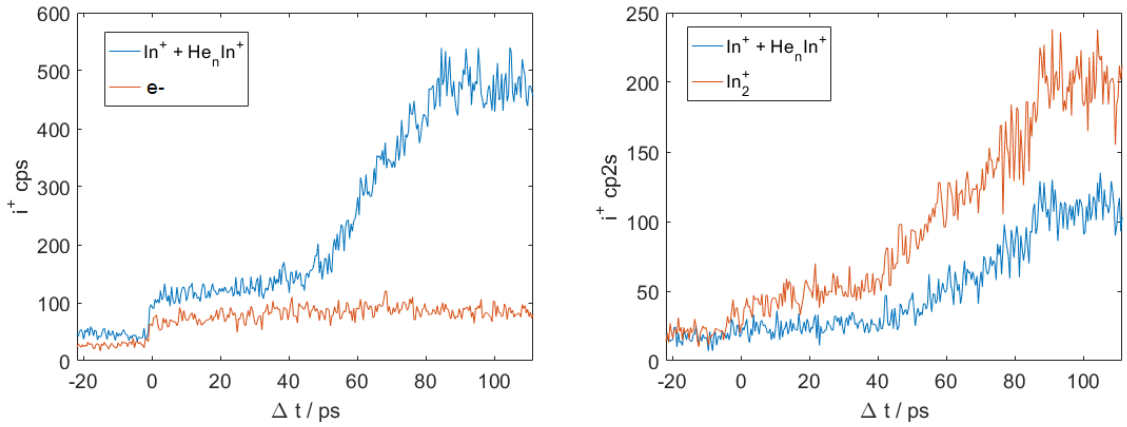

(a) (b)

Figure 3.5: Ion time scans pumped with (a) 345 nm and (b) 363 nm, probed with 396 nm. Pickup conditions: p_{He} = 40 bar, T_{CH} = 18 K and T_{PU} = 601°C.[LBE:(a)31/05/2017,(b)01/06/2017]

3.1.3 Upper temporal limit for photochemistry in He_N

In this section the very first time-resolved PES of dopants inside the He_N are presented. The shift to lower energies of the monomer peak at 0.4 eV with increasing time delay in fig 3.6b, documents not the ion but the atom dynamics, representing the different positions of the excited dopant on its ejection trajectory. The atom ejection time scales (red, turquoise) nicely match the ion time scales (blue, green) in fig. 3.6. The discrepancy stems from the ion recapture mechanism and is further discussed in the next section. The total peak shift is determined to 20 meV. According to the energy difference expected in the PES between the bare atom line (410 nm) and the He_NIn center state (376 nm), one might look at fig. 1.3 for support, the total peak shift is expected to actually be in total 300 meV. This raises the suspicion that the missing energy is deposited into a bubble expansion, i.e. a drop deformation upon the dopant emerging. Whether this is true is still to be verified by investigating the peak shift at very small time delays ($<$ 10 ps). With a thinner SHG crystal, the additional housing of the optical table for long term stability, and the OPA's future post-compressor, the pre-compression trade-off between both optical paths becomes feasible and the observation of the bubble expansion comes within reach. Apart from that, the ion yields quantitatively matches fig. 3.4a.

Experimental conditions were a nozzle temperature of 18 K, i.e. relatively small droplets, a pickup temperature of 540°C, OPA pump of 376.5 nm and SHG probe of 420 nm with the 5 mm LBO for sufficient energy resolution. Not physical peak shifts may occur due to either charge effects on the repeller or a laser beam walk due to temperature fluctuations. As the measured total peak shift is 20 meV, ca. room temperature, these effects need to be treated carefully.

Latest observations and discussions revealed that the kinks in the bare atom peak position in fig. 3.6c at various time delays might not be noise, but real dynamics such as a bubble expansion and subsequent oscillation. These are not discussed in this work and current object of research.

In conclusion, fig. 3.6b proves that femtochemistry is possible inside He_N, and fig. 3.6c determines that any photochemistry experiment in this system is limited to take place within at maximum roughly 50 ps.

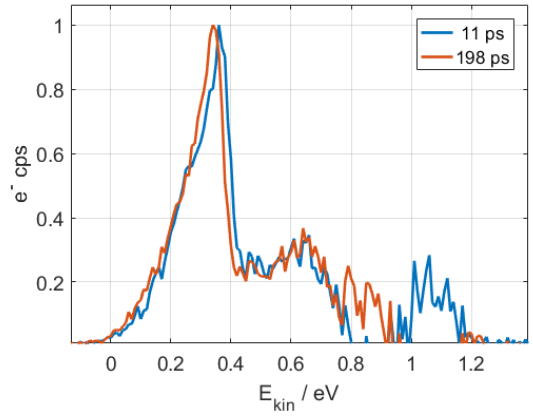

(a) PES for 2 different time delays

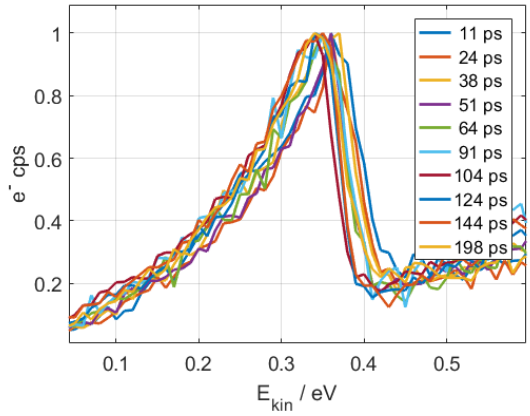

(b) Detail of (a)

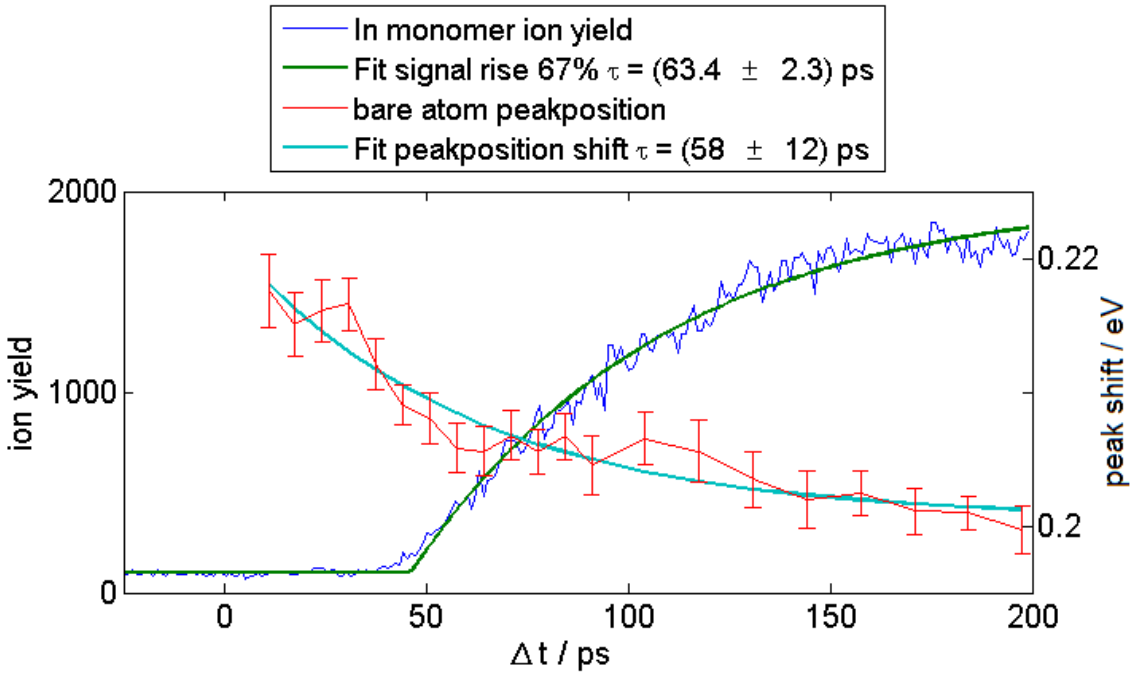

(c) Time dependency of ion yield and photo electron peak shift

Figure 3.6: Time-dependent photoelectron peak shift and ion yield. The peak shift is obtained from the peak positions in (b). [LBE:(a,b)21/07/2017,(c)25/07/2017+31/07/2017]

3.1.4 He_N size dependency of dynamics

To investigate the influence of the droplet size on the dynamics In^+ time scans for five different nozzle temperatures have been recorded in fig. 3.7. Lower nozzle temperatures account (legend) for larger droplets. Surprisingly there is no observable influence although the coldhead temperature regime covers droplet radii from 2 nm to 4 nm, a factor of 2, corresponding to most probable droplet sizes of roughly 1000 to 10000 He atoms (see App A.1 in ref. [29]). This suggests that the critical fallback- or recapture radius, visible via the onset of ion yield at the critical recapture time delay of 50 ps, is much larger than the droplet radius and is current subject of theoretical work. The fallback radius can be estimated from the ionic ground state holding potential in fig. 4.2 in the next section to be at approximately 5 nm for the intermediate droplet size of N=4000. With the mean droplet sizes in the experiment well below this limit the observation becomes more reasonable. Reproducing the result with an intermediate constant pickup temperature to exclude He evaporation effects and with smaller time steps is advisable In analogy, TDDFT-calculations investigating the desorption and fallback dynamics of two different surface state excitations of Rubidium have been carried out in ref. [10].

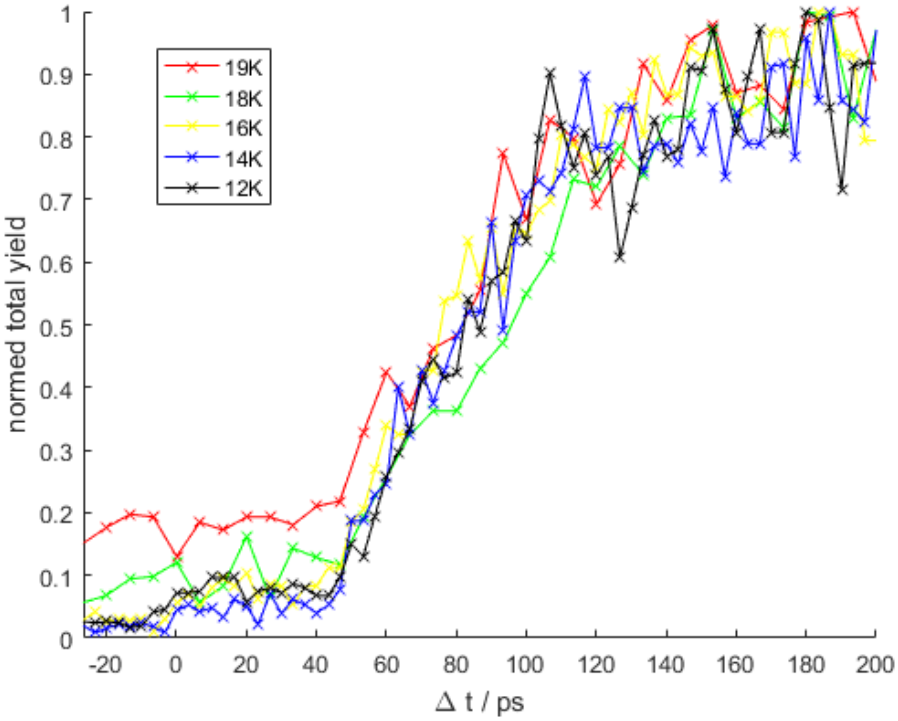

Figure 3.7: In^+ time scans for five different mean droplet sizes. Lower nozzle temperatures account (legend) for larger droplets. Experimental conditions: T_{PU} = 563, 547, 543, 519, 518°C in the same descending order as in the legend in the figure, p_{He} = 40 bar, Pump: 377.5 nm, Probe: 419 nm. The pickup temperatures were adjusted for sufficient signal yield. [LBE:02/08/2017, pre-optimisation:01/08/2017]

CHAPTER 4

Simulations

In this chapter, the usage of the potential energy surfaces of the He_NIn ground state and 1st excited state as well as the ionic ground state for molecular dynamics (MD) simulations is documented and the results compared to the experiment.

4.1 Potential energy surfaces

The theoretical considerations in this section are attributed to Ralf Meyer, Johann Pototschnigg and Andreas Hauser and are crucial for the interpretation of the important result fig. 3.1a and basis for further simulations to reproduce fig. 3.6. The performed DFT- as well as bosonic Helium-DFT-calculations to acquire potential energy surfaces, on which my work builds on. Their theoretical work is documented in detail in the collaborative publication ref. [31] and supported by the experimental findings in this thesis. The following short outline of the calculations might be helpful for a deeper understanding. First, the diatomic potential curves of In-He are calculated. All ab initio calculations are performed with the MOLPRO software package. [32] Two different families of basis sets are used. A first set of curves is calculated using the Aug-CC-pV basis sets and are extrapolated to the basis set limit. [33] In order to quantify the influence of the basis set another set of calculations was employed using the Def2 basis sets [34] and also extrapolated. The two experimentally relevant ab initio potential energy surfaces (PESs), $X^2\Pi_{1/2}$ and $2^2\Sigma_{1/2}$, deviate by 0.1 cm^{-1} depending on the basis set and are further used to calculate the helium density distribution and the free energy of a In-atom-doped He nanodroplet via helium density functional theory (He-DFT) based on the Orsay-Trento density functional. [35]. One-dimensional PES scans of the He_NIn system can be obtained by a minimization of the free energy as a function of the distance of the In atom from the He_N centre of mass. For comparison with the experiment $N = 4000$ was chosen. The results of the ground state and 1st excited state for this droplet size are presented in fig. 4.1 and compared for the two different basis sets. In fig. 4.2 the results are compared for the AugCC basis set for ground state, 1st excited state as well as the ionic ground state. These potential energy surfaces are further used for the classical dynamics model in the next section.

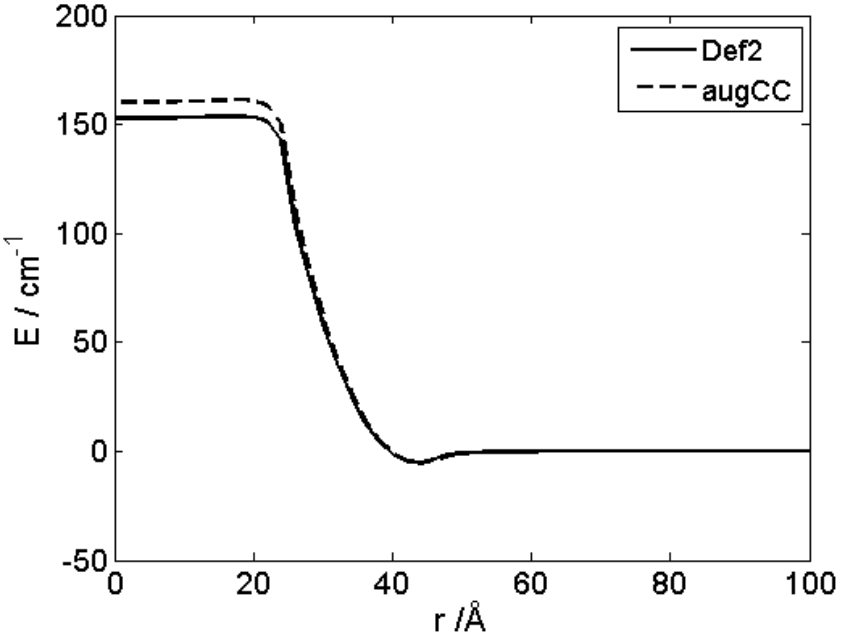

(a) 1st excited state of $He_N In$. A major part of the center states, 25-40 Angström are repulsive, while the surface states at 42 Angström are weakly bound.

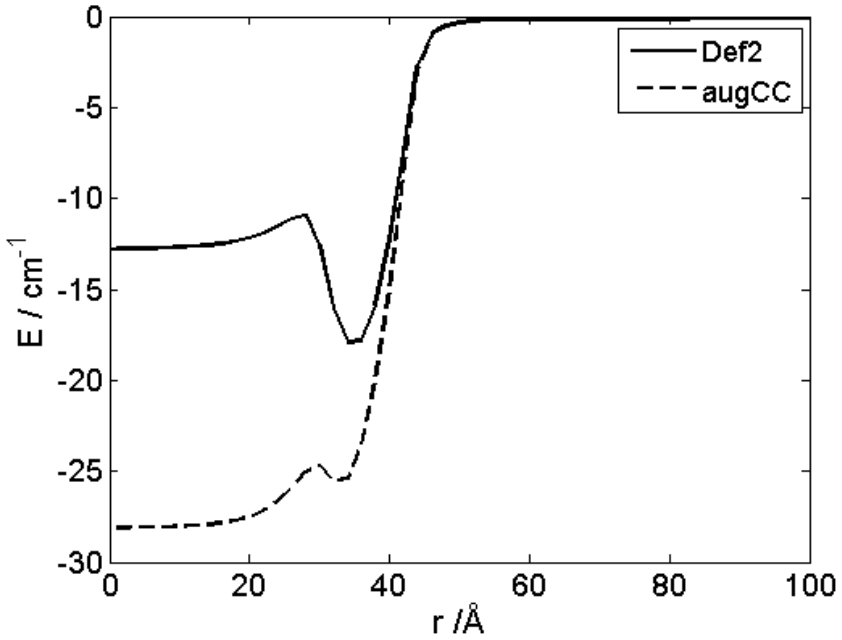

(b) Ground state or holding potential. The experimental findings can be explained with both basis sets, but in an entirely contradicting way.

Figure 4.1: Ground (b) and 1st excited (a) state of $He_N In$. The black lines indicate the result using the pair potential obtained with Def2 basis sets and the dashed lines indicate the result obtained with the AugCC basis sets. The pair potentials for both basis sets deviate from another by only 0.1 cm^{-1}, yet this minor difference within the accuracy of the method has significant influence on the holding potential (b). With kind permission by Ralf Meyer.

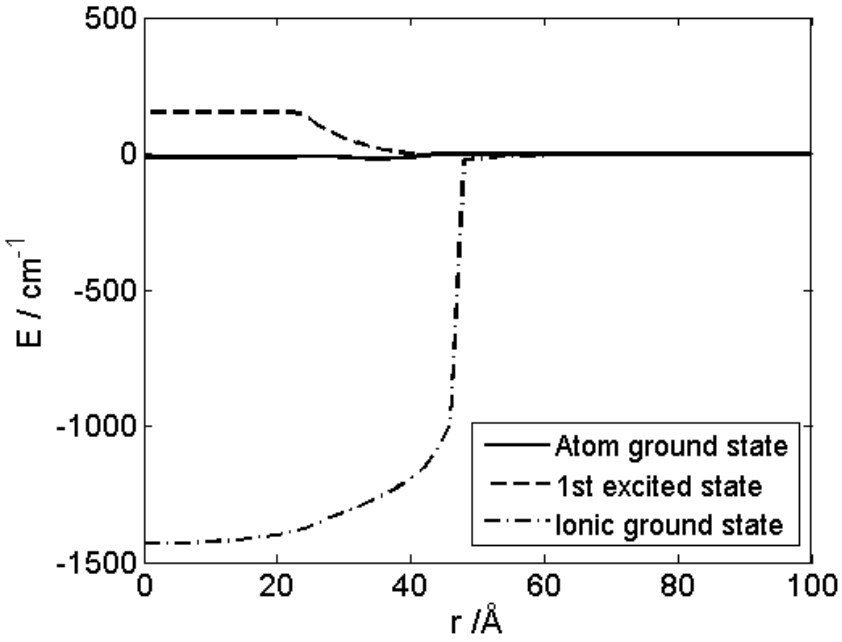

Figure 4.2: Comparison of neutral ground and 1st excited state and ionic ground state of $He_N In$. With kind permission by Ralf Meyer.

4.2 Molecular dynamics

Using the potential energy surfaces from the previous section, the author wrote a Matlab (see lst. D.1) script in an attempt to theoretically describe the shape of the dynamics observed in fig. 3.6, particularly the dynamics in the ion yield time scan. This approach is a purely classical molecular dynamics (MD) simulation and suffices to reproduce some characteristic features from the experiment but lacks of the power for a quantitative agreement for now. Further, some inconsistencies in the model have yet to be corrected and will be discussed shortly. In parallel to the classical approach, Bernhard Thaler conducted quantum mechanical calculations of the dynamics using the BCN-TLS-He-DFT-code of the Barranco group [36].

From considerations about the velocity inside the droplet one can deduce the formula (ref. [31])

$$\rho(r, E) = \frac{1}{Z}\Big(\frac{2}{m}(E - V(r))\Big)^{-1/2} \tag{4.1}$$

with ρ the probability density function, r the radial distance to the center of mass, E the total energy, Z a normalisation constant, m the reduced mass, $V(r)$ the ground state potential. Using the ground state potential derived from the AugCC pair potential (fig. 4.1b) and an assumed Boltzmann factor qith a temperature of 370 mK for the occupancy one can calculate the probability of presence. In this model, the energy levels are degenerate due to angular momentum, thus the Boltzmann factor factorises into one for the translational plus potential energy and the rotational energy. To obtain the probability of presence above expression is integrated with respect to energy and its degenerates. The PDF is then sampled using the open access script *discretesample.m* to obtain a histogram,

each entry in the histogram representing a particle. From the probability of presence one obtains the probability of excitation by multiplying former with the overlap of the laser bandwidth with the spatial solvation or excitation energy shift which is interpreted as a scattering cross section and a probability density function hence. In this simple script, the scattering cross-section was approximated by a Heaviside function, which' quantification is still open to debate. The result of this sampling can be seen in fig. 4.3.

Each particle has a start velocity assigned which is sampled with a gaussian ($\mu = 0$, $\sigma = v_L$, v_L being the Landau speed) in good approximation to a $cos^2(\theta)$-distribution. The latter is deduced from the projection of all momenta onto the radial axis. The photoinduced excitation dynamics is implemented by feeding the particles into a Leapfrog-algorithm [37] where the force according to the excited state potential acts on the atom. Upon ionisation the forces are calculated then from the ion potential. The effect of viscosity above a certain relative velocity in bulk superfluids, the Landau velocity v_L, is implemented with a velocity constraint invoked inside the droplet.

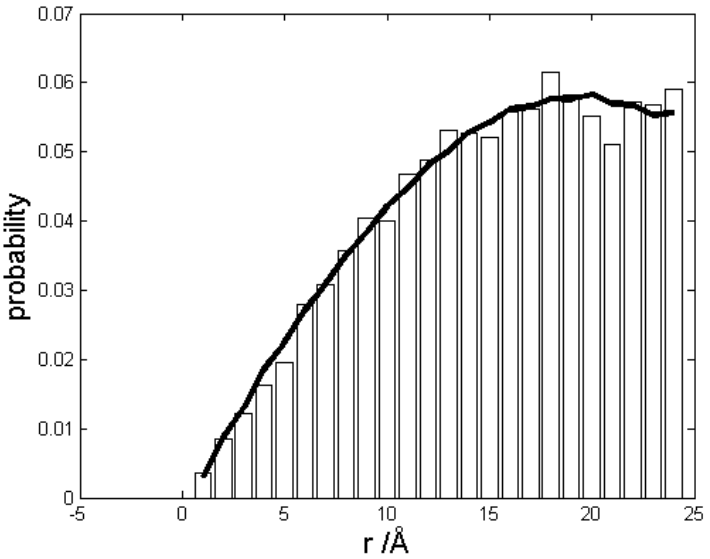

Figure 4.3: Probability of excitation as calculated with the model described in the text and with the parameters documented in the appendix in lst. D.1

The major advantage of the classical approach above the quantum mechanical one is, despite its inconsistencies, the low computational effort. To emphasise this, the force fields were implemented with a coarse description. The potentials were interpolated linearly and a finite list of forces calculated, now being a step function of the position. The forces were indexed in the same manner as the positions. After performing a frog leap, merely the change of the position index is needed to acquire the force acting at the new position. Unfortunately there is a bug in the script regarding the data type of the index which is not reproducible as it seemingly occurs randomly. The atom and ion trajectories are calculated in nested loops. The outer loop calculates the atom trajectories and enters the inner loop at any given ionisation time. The inner loop then calculates the ion trajectories with initial conditions retrieved from the outer loop. Examples of such trajectories are provided in fig. 4.4 on p. 59. In both loops the number of particles beyond a certain distance are recorded, resembling whether the particle is free or bound. In the former case it would be detected by the counter in the experiment. The results are compared to the experimental data in the next section using the custom-made script *ion_yield_dopant_ejection_timescan.m* and the function *indium_peakshift_v2.m*.

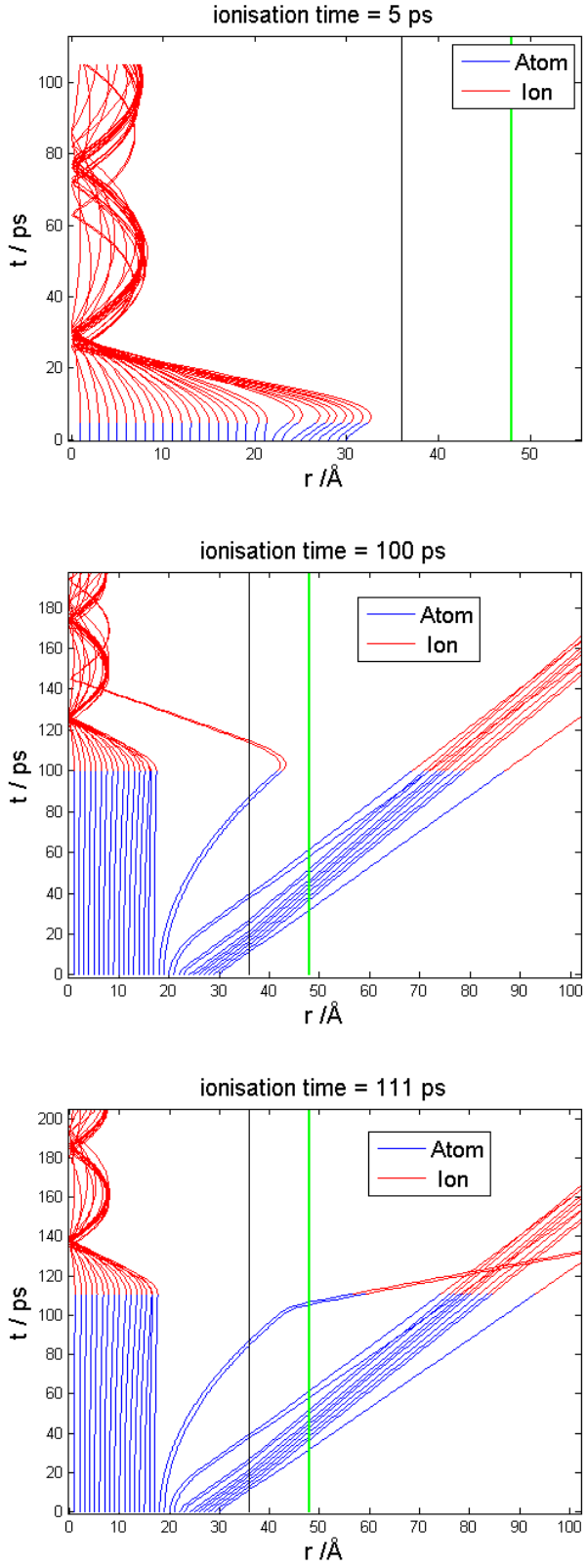

Figure 4.4: Atom and ion trajectories for different time delays. Trajectories are very different for surface and center states and whether the ionisation happens inside (top), or outside (bottom) of the droplet. Comparison of the trajectories with initial conditions r(t=0 ps)= ca. 20 Åin (middle) and (bottom) shows the delicate equilibrium some of the outer center states are in at time delays of roughly 100 ps. The black line indicates the droplet radius, the green line indicates the recapture radius.

4.3 Comparison to the experiment

The center states (1-29 $\mathring{A}$) in fig. 4.1 are blueshifted by ca. 2000 cm^{-1} while the surface states are blueshifted by only 800 cm^{-1} in the experiment (fig. 3.1a). Both theoretical holding potentials in fig. 4.1b are able to qualitatively explain the main feature of the spectrum, i.e. the double peak shift. The line blueshifted by 2000 cm^{-1} originates from the center states due to a higher solvation energy relative to the surface states, yet the origin of the significant line broadening is still unclear. The line blueshifted by 800 cm^{-1} can either be explained by low angular momentum surface states in the global minimum of the Def2 approach (black line, fig. 4.1b) or, contradictory, by high angular momentum surface states outside of the local minimum (40 $\mathring{A}$) of the AugCC approach.

While the ground state is hypersensitive to the pair-potential, the 1st excited state apparently is not, however the dynamics, further investigated in the next section, are hypersensitive to the excited state. The excited states calculated by Ralf Meyer with both basis sets Def2 and AugCC do have a local minimum in the center at $r = 0$ $\mathring{A}$, not visible in the plot (fig. 4.1a) due to the scaling, with a depth of about 1 cm^{-1} or $v_L/3$ respectively. Here v_L is the Landau velocity and denotes the upper limit for frictionless motion in superfluid bulk. [38] The same calculations, conducted by Bernhard Thaler using the Barranco code instead [36], did not show such a local minimum in the excited state. Due to the different implementation, Ralf Meyer fed spline-interpolated pair-potentials into the Orsay-Treno-functional, whereas Bernhard Thaler used an analytic fit instead. Whether the difference in the center 1st excited state originates from the code or minor differences in the pair potential that was used is current matter of investigation. Yet the existence of the local minimum is crucial to the center state dynamics as will be discussed at the end of this section.

The result in fig. 4.5 nicely matches the experimental data but has been achieved with a excitation cross-section cut-off at 25 $\mathring{A}$, an assumption still open to debate. Furthermore the initial velocity sampling and the temperature in the Boltzmann factors are not consistent. Apart from that, the temperatures in the rotational energy Boltzmann factors suppress high angular momentum states, quite in contradiction to the findings in [39]. This would also make it impossible to explain the spectrum fig. 3.1a quantitatively with the AugCC pair-potential which was used until this point. The implementation of the viscosity is heuristic and coarse. Further comparison of trajectories resulting from classical MD with those resulting from Bose-TDDFT is still open. At the very root of the model, the trajectories depend heavily on the exact shape of the excited center states, i.e. whether they have a local minimum or are slightly repulsive. The ion rise constant further slightly depends on the velocity distribution and heavily depends on the probability of excitation and the probability of presence hence, which in turn depends on the holding potential. The latter is very sensitive to differences in the pair potentials within the accuracy of the used basis sets. The existence of the local minimum in the center excited state is yet crucial to their dynamics, i.e. whether atoms at the droplet center with a kinetic energy corresponding to $v_L/3$ or lower do get ejected upon excitation eventually or not. The assumption that the local minimum is not physical but flat in reality would postulate a second ion yield increase at very long time delays, several hundred picoseconds to nanoseconds, in fig. 3.6. An experiment testing this hypothesis would therefore give some insight into the detailed form of the center 1st excited state.

Finally, the atom ejection begins after approximately half the time delay needed for the ion ejection. This onset resembles the fallback- or ion recapture time as discussed earlier in sec. 3.1.4 and in [10]. Assuming similar potential energy surfaces for different droplet sizes, varying the atom number by a factor of ten and the droplet radius by a factor of 2 thus, the critical fallback time would still be longer than the earliest atom ejection time. This conclusion is in agreement with the missing droplet size dependency of the dynamics in fig. 3.7.

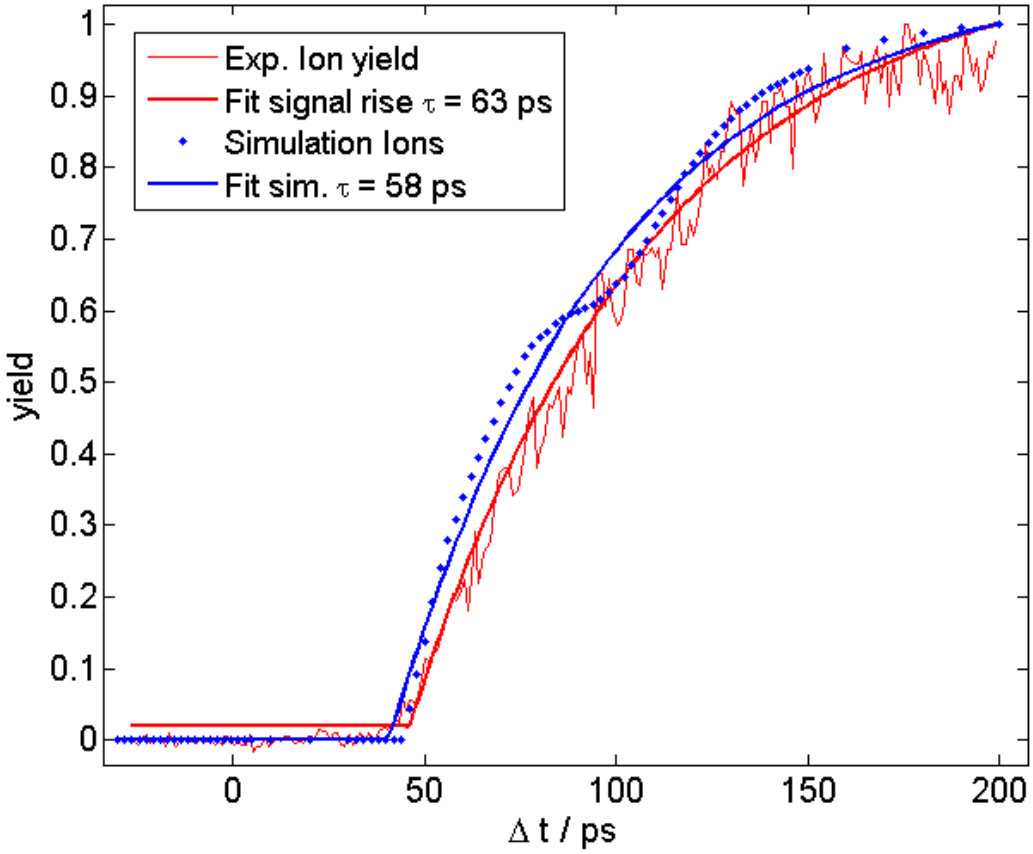

Figure 4.5: Simulated ion yield time scan compared to the experimental data as calculated with the model described above and with the parameters documented in lst. D.1 in the appendix and the sampling in depicted in fig. 4.3.

CHAPTER 5

Open questions & debugging

5.1 Experimental issues and debugging

There are several experimental issues that need to be considered. These are of both physical and technical nature and stem from the droplet source, the laser source and the TOF.

5.1.1 General issues

Obviously one should always monitor the experimental conditions, i.e. vacuum pressures, helium stagnation pressure, nozzle and pickup temperature as well as pickup current and the ratio of the ion currents of monomer to dimer in the QMS. Some general issues are addressed as follows.

Thermodynamic equilibrium of the nozzle and nozzle alignment

After starting the compressor, the coldhead takes about 1.5 hours to cool down from room temperature to the cold regime of 11-19 K. However, the nozzle takes at least 4 hours to achieve thermodynamic equilibrium. During this time mechanic stress causes a misalignment of the nozzle with respect to the skimmer, leading to a rise or fall of the signal over time. Therefore one should optimise the position of the nozzle when one is confident that no further mechanic strain will be induced. A good indicator for the optimisation is the maximum of the ion current of the He dimer (m=8u) in the QMS with respect to the nozzle alignment. Typically quarter or half quarter turns of the screw on the z-axis lead to success. Apart from this, sudden drastic change in nozzle temperature or helium pressure will transiently alter the pickup statistics until equilibrium is reached again. An increase in temperature by 50 % will lead to an increase of pressure by 50 %. This effect can typically be observed in the ultracold regime, e.g. when heating the nozzle from 11 K to 18 K within a couple of minutes. The problem can simply be solved by waiting or using the vent at the pressure reducer.

Pickup conditions

It turned out that some obvious ways of documenting the pickup statistics are actually not suited for that purpose. Neither the electric oven current nor the temperature measured with the electric current nor the thermocouple, but the ratio of the ion current signals in the QMS, In_1/In_2, provide sufficient reproducibility. It seems that the oven's resistance and current slightly depend on the total mass of material deposited in the oven. Over time with more material evaporated, less material remains in the oven respectively, more and more current is needed in order to achieve the same temperature, an effect that can be observed especially well when the oven empties. This may be linked to the decreasing surface of the melt and interface of melt and cup. The interface influences heat exchange, while the surface influences heat radiation. The most important effect though is a decrease in melt surface upon material depletion due to the conical shape of the porcelain cup. At a given temperature, a decreased melt surface accounts for a lower vapour pressure. To compensate this effect, one must increase the temperature or the current respectively to achieve the same pickup conditions realised a few days earlier. It was found that the ion current signals in the QMS provide good indicators for the pickup statistics. Interesting signals are the He dimer (m=8u) in order to check for He droplet generation, the In monomer (m=115u) for the pickup as well as the effusive beam, and the In dimer (m=230u). The ratio of the In monomer, after subtracting the effusive part, to the In dimer is sensitive to temperature and should be chosen in order to set the pickup statistics, e.g. whether one desires In monomers or dimers. Naturally, the ratio decreases with increasing temperature, as higher temperature means higher vapour pressure and hence higher probability for the He droplet to pick up more than one In atom. Undesired species might become a problem if they spectrally overlap with the species of interest. This is the case in the experiments in this work as the first excited center state of He_NIn is coincidentally in vicinity to some excited states of the He_NIn_2 .

Thermodynamic equilibrium of the QMS filament

Furthermore at stable nozzle conditions one can still observe an increase in signal during heating up of the QMS ion source filament (cathode). One should turn on the emission current at least half an hour before the experiment to ensure a proper equilibrium.

Repeated repeller optimisation procedure

In particular for SHG wavelength scans, the beam focus might move with every point of measurement due to the tilt of the SHG crystal. The geometry of the setup defines tilting as rotation in plane of the optical table. As we primarily tilt and do not rotate, the change of the focus position in comparison to the z-position of the repeller is negligible. This is important as a cross section with the helium beam is required. However the x- and y-directions may change (for the definition of the coordinate system see fig. 2.1). The focal length is 1 m and a broad focus in beam direction (= x-direction) is expected, therefore a broad plateau of the signal's maximum regarding the x-position of the repeller. The y-position on the other hand is more sensitive, which is rather linked to the magnetic bottle of the TOF. If the maximum is completely lost, a tiresome but success-oriented strategy to find the signal maximum is to scan the xy-plane with a meandering pattern.

Repeated laser beam realignment

In hope of better optimisation at low count rates, alternatively to the above described repeller optimisation, it was tried to re-align the beam path using two apertures for documentation before and after the main chamber and the two final mirrors in the beam path. Nevertheless poor reproducibility at high effort was found. In the progress even the combined method of laser beam alignment and repeller optimisation was dismissed in favour of repeller optimisation only.

Charge effects on the repeller

At some occasions the electron signal was found to vanish randomly and instantly, an effect that was neither reproducible nor was due to any apparent reason. The reason was linked to a floating potential of the repeller, caused by either a defect voltage supply or a defect cable. The floating repeller charged positively, effectively dragging the electrons away from the spectrometer. The effect could not be observed in ion mode, and can be tackled simply by earthing the repeller where one has to deal with a signal trade-off as count rates should decrease slightly (by a factor of 2 at maximum). A simple method to check for charge effects is to plug in and out the voltage supply of the repeller and compare the signals of ions and electrons, as charge effects might only cause one of the two kinds of signal to vanish.

Multiphoton ionisation processes

At high intensities, multi-photon-ionisation processes may occur. These can be tackled by increasing the ionisation volume by broadening the laser beam and, if necessary for sufficient signal yield, simultaneously increasing the laser power. This is possible because the helium beam is estimated to be of 2-3 mm diameter. One can search for a good point of operation by performing a power scan, i.e. measuring electron counts for different intensities, for a representative wavelength and set of parameters. For further measurements one should choose the intensity such that there is a maximum of signal but still an insignificant amount of multiphoton events. This is the case in the regime where the slope of the double logarithmic yield-vs-power-curve is well below 2.

Influence of the fundamental laser wavelength

When shining red light onto a SHG crystal, only a fraction is converted into blue. Not separating the red and the blue might cause various troubles during measurements, such as follows: In particular for very long pulses, a cross-correlation signal of the red and the blue pulse as both arrive simultaneously, bad reproducibility due to difficult chirp optimisation which can only be done for red and blue equally, undesired excitation events due to red if possible in the first place. In the case of the 5 mm thick LBO used for SHG, the pulses are very long ($>$ 1 ps), which leads to the assumption that the red and the blue pulse may overlap temporally. In addition to that we assume many states of the free atom to be in resonance with a 395 nm (1 nm bandwidth) + 800 nm (80 nm bandwidth) transition, especially because of the high bandwidth of 80nm of the fundamental. Apart from this, the power normalisation, i.e. setting the laser intensity to a specific constant value for an experiment, is easier using the power meter. The power meter always measures the power of red and blue simultaneously. This requires the use of a non-monochromatic source to use a spectrometer for normalisation, as the power meter cannot tell the hight and area below the blue and red peak respectively. For our single pulse measurements simply a prism was used. This has the advantage of separating both colours quite well, but is an improper tool for time-resolved measurements as the pulse width increases drastically due to dispersion. Hence for two pulse measurements one might use dichroic mirrors which do not invoke dispersion upon the pulse. Dichroic mirrors are reflecting for a certain wavelength and transparent for the other. In this case the mirrors are transparent for red. As the reflectivity in the red is not entirely zero, one might use 2 or even 3 dichroic mirrors to minimise the red light's influence. A simple check for an influence of the fundamental is a comparison of the electron or ion yield at a certain blue wavelength for different ratios of the area under the blue and red peak.

5.1.2 SHG wavelengths scans

On the next page a step-by-step recommendation, which avoids above described issues, for SHG wavelength scans is outlined.

Attention - possible dangers

One might avoid too high count rates in order to prevent damage to the MCP. A guide value for maximum count rates is 3000 electron counts per second. The reference to the lab book [LBE:20/04/2017+26/04/2017] documents typical count rates for such experiments, and was further used for evaluation of fig. 5.1.

Step-by-step procedure for a SHG single pulse wavelength scan

1. **Pickup conditions:** Realise desired pickup conditions via nozzle temperature, He pressure and pickup temperature. When interested in the In monomer, one wants a high ratio of In monomer to In dimer. Check with the ion current signal in the QMS. To this end one needs to measure the pickup signal (both valves V1 and V2 open) as well as the effusive signal (valve V1 closed, V2 open) and subtract the latter from the first to determine the amount of signal caused by the He_N beam.

2. **Set wavelength**
   a) Set desired wavelength via tilting the SHG crystal using a spectrometer
   b) Optimise the chirp to acquire maximum conversion efficiency and a neat and narrow spectrum
   c) Repeat steps a and b until satisfied

3. **Optimise repeller position:** First, for optimisation of the z-position read the Master's theses of Paul Maierhofer and Markus Bainschab. [20, 21] Shine into main chamber and turn up the laser power with the halfwave-plate until a nice pickup signal is achieved (both valves V1 and V2 open). High count rates and low integration time (1 sec) allow for an easier repeller optimisation. Set the repeller position to maximum count rate. Scan primarily in y-direction, secondly in x-direction if no signal is found in the first place. One should always try to go past the maximum from both sides and then go to the middle of the two flanks. Proceed in quarter turns until one reaches the left flank. The reference point shall be where the signal drops to half. Then proceed to turn right past the maximum plateau until one reaches the right flank. Again the reference point shall be where the signal drops to half. Now set the repeller to the median position of both flanks. The FWHM is approximately 11/4 turns in y-direction, in between is a broad signal strength plateau.

4. **Normalise the laser power:** In order to obtain comparable count rates for each wavelength, one needs to measure each point with the same intensity. This point should be decided prior to the experiment and can be realised using the power meter. Low intensities avoid multi-photon processes but lead to low count rates. In this experiment one typically changes the laser power for repeller optimisation and then again back to the reference value.

5. **Set integration time of the counter** according to signal. Low signal requires high integration time (suggestion: 10-30 sec)

6. **Integrate**

7. **Repeat steps 2 to 6 for each wavelength while observing the parameters described in step 1**

5.1.3 THG experiments

When using THG one has to deal with further issues apart from those outlined above:

Self phase modulation

Self phase modulation (SP) manifests as 'rainbows' if the focus is in air and coloured (red, orange), seemingly fluorescent dots if the focus is in the entrance window. Furthermore defocusing occurs, which can be observed as schlieren in the fluorescence light of paper held to the window opposite of the entrance window. This defocusing causes further stray light, which' influence is discussed in the next paragraph. SPM in the MC entrance window due to too high laser intensity can be tackled by aligning the focusing lens such that the distance between window and focus increases, or by exchanging the window with a thinner one. Because a thin window doubtfully will withstand the mechanical stress induced by the pressure difference, the entrance hole diameter might have to be decreased.

Stray light

Stray light is troublesome as 266 nm is above the work function of some material(s) in the chamber, e.g. the graphene film or the copper hat on the repeller. These materials and their work function are still to be characterised.

Invisibility of UV

The UV light is invisible to the human eye, the camera and the beam profiler, residual blue and red light from the mixing are visible although and might be highly misleading in regards of the actual position of the UV laser light. Still, using the camera, high pass colour filters and fluorescent paper might be helpful in regard of spatial overlap alignment. The fluorescence light can be detected with the camera, while identifying the different sources (red, blue or UV parts of the laser beam) of the fluorescence is determined with colour filters, e.g. red filter for red, blue filter for blue. UV (THG or higher energies) e.g. transmits quartz glass, but does not transmit BK7 glass.

5.2 Open questions

All of the open questions in this section are addressed in the light of the observations in chapter 3, particularly the excitation spectrum (fig. 3.1a) and the PES (fig. 3.6).

5.2.1 SHG single pulse experiments

The first experiments were conducted with single pulses using SHG. SHG has the advantage that it is simple, easy and stable. For the OPA, the desired wavelengths are in a borderline regime, and the operation is thus tiresome. Hence the obvious decision was to record a first single pulse spectrum using the 5 mm LBO for minimum laser bandwidth. The result is shown in fig. 5.1. To disentangle the origin of the contributions of the left peak the experiment was repeated with different pickup temperatures. Originally the signal at 385 nm was assigned to the In dimer via variation of the pickup conditions. This conclusion has shown to be wrong from its contradiction to fig. 3.1a. The most simple explanation for this is a rapidly increasing noise caused by subtraction of increasing effusive signal. One might think that the raising left flank possibly stems from increasing ratio of the numbers of bulk states to the numbers of surface states. Yet this is in utter contradiction to the reasoning that for single pickup always the same amount of He evaporates, and further with higher pickup temperatures and higher multi-pickup probabilities the droplet size decreases, thus the ratio of surface to center states increases, quite in contradiction to the experimental finding.

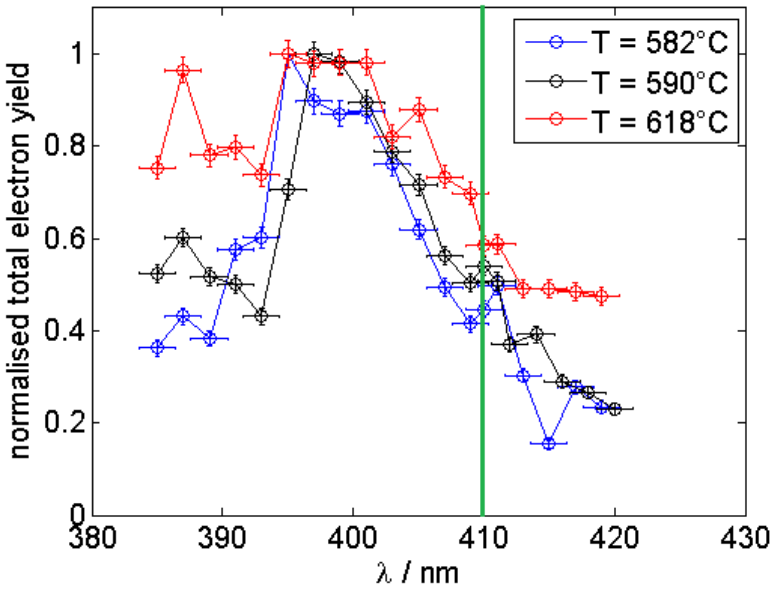

Figure 5.1: Single pulse excitation and ionisation spectrum. Integrated electron spectra for three different pickup temperatures. Depicted is the total electron yield for the 3 chosen pickup conditions, each normalised to its maximum. The green line indicates the transition of the free In atom. The temperatures were measured with the thermocouple. Experimental conditions: Nozzle temperature 17 K, stagnation pressure 40 bar, integration time 30 sec. The excitation wavelength was realised with a 5 mm LBO crystal, which limits the bandwidth to 1.4 nm.[LBE:20/04/2017+26/04/2017]

5.2.2 SHG-SHG pump-probe experiments

After successfully recording the first single pulse spectrum of $He_N In$, first time-resolved experiments were conducted. To this end, a beam splitter was introduced and another SHG path was installed. The experiment was cleverly designed, probing the, what later turned out to be 1st excited surface state at 397 nm with a wavelength of 415 nm, spectrally well distinguishable from both the bare atom line and the addressed state. Different regimes of pickup conditions, pump- and probe mean intensities controlled via laser power and beam focus diameter, pump- and probe peak intensities via trying different SHG crystals and even probing less elegantly with 397 nm was tried. The reasons to switch the probe energy were to test for a Koopman minimum on the one hand, and to improve the time resolution on the other hand. A Koopman minimum means that the Franck-Condon overlap of the addressed state, being the 1st excited one here, with the ionic ground state and the free electron wavefunction is vanishingly small. The latter changes with a change of the probe wavelength, hence the test by varying the probe wavelength. For the latter reason, a thinner SHG crystal was used, limiting the SHG spectrum significantly. E.g. a 200 μm BBO crystal's conversion efficiency at 415 nm is practically zero. Despite all efforts, no signal was visible. Possible explanations are insufficient contrast or signal strength for both ion yield and photoelectron spectra due to either unfavourable laser mean and peak intensities or pickup conditions, not optimal TOF resolution due to too high repeller voltage of -3V, a very low ionisation probability from this state in a spectrally broad range or due to polarisation, and low oscillatory strength due to the broad pump spectrum.

Conclusively, no dynamics, neither in ejected ions nor in photoelectron spectra, could be observed in this experiment. Yet a cross-correlation signal and the long living bare atom line was found and time-zero determined hence. The reasons for the missing success of this experiment are most likely of technical nature, i.e. an unfavourable pickup parameter regime, as proof of surface state dynamics has been provided by the OPA-SHG pump-probe experiments, specifically with fig. 3.1a.

5.2.3 OPA-THG pump-probe experiments

To deal with the bad contrast observed in the SHG-SHG pump-probe experiments, i.e. separate the probe signal from the pump-probe signal spectrally in the photoelectrons, the probe wavelength was changed to 266 nm. This is achieved with THG and the optical setup required is described in the Master's thesis of Paul Maierhofer [20].

In conclusion, probing the 1st excited state of $He_N In$ with THG was not successful. To clarify whether this is due to physical reasons, such as a Koopman minimum (also see sec. 5.2.2) , or technical reasons, e.g. no spatial overlap achieved due to UV invisibility or the latter lost due to bad stage alignment, the following tests in the same setup were considered:

- The different polarisation of the paths seemingly had no influence.
- Probing the 1st excited state of the bare atom with THG was not successful. The same statement holds for the states of $He_N In$ pumped with wavelengths of 380 nm (OPA) and 397 nm (OPA).
- Probing $He_N In_2$ states corresponding to the pump wavelengths 362 nm and 374 nm (acc. to OPA calibration) with THG was successful though. Deduced from the PES (fig. 5.3a and 5.3b) only a structure probably corresponding to $He_N In_2$ was identified, and corresponding time scans yielded ions for 362 nm in fig. 5.2c, none for 374 nm, fig. 5.2b, though. The gates have not been set to disentangle whether these ions are In^+ or $In_2{}^+$. Former signal contributions would probably originate from dissociated In_2 or $In_2{}^+$ as implicated by the missing photoelectron signal. The original point of these experiments was actually an easier optimisation of the spatial overlap.

- Probing the $He_N In$ state corresponding to the $5s^2 5d$ state of In (306 nm) at a time delay of ca. 185 ps with THG was successful, with bad contrast though (see fig. 5.3c).

- The state pumped with 266 nm was successfully probed with wavelengths of 362 nm, 374 nm and 380 nm (OPA-calibration). The time scans are shown in fig. 5.2abc. Additionally, dimer dynamics have been observed in fig. 5.2c.
- No cross-correlation at the desired wavelengths was observed. This makes it impossible to exactly determine time-zero, rough estimates (very long, short or negative time delay) can be made though via previous measurements. It is unclear whether this observation is due to physical reasons or a misalignment of the spatial overlap due to a misalignment of the stage.
- SHG-THG pump-probe experiments to check whether the issue lies with the pump have not been conducted.

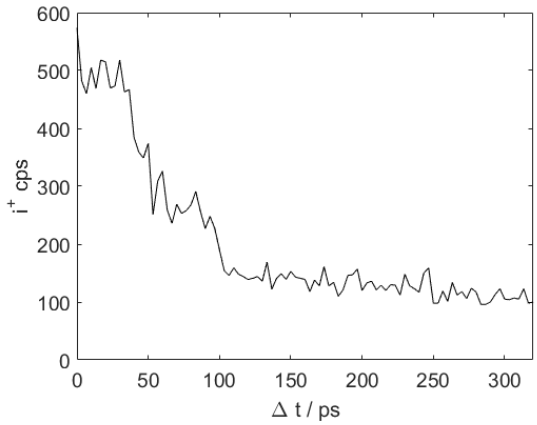

(a) 380 nm

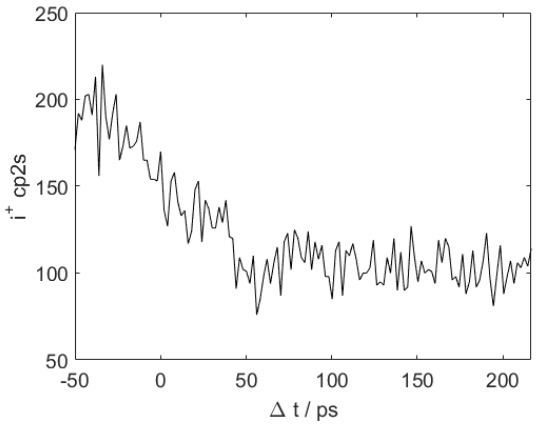

(b) 374 nm

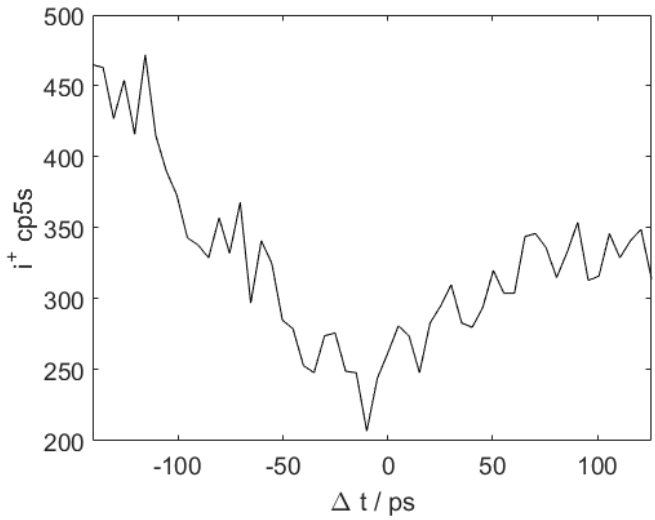

(c) 362 nm

Figure 5.2: Total ion yield depending on the time delay for 380 nm, 374 nm and 362 nm pump respectively. Note that the time delay is not calibrated because it was not possible to find a cross-correlation signal to determine time-zero, due to either a Koopman minimum or loss of spatial overlap due to stage misalignment. Yet (c) gives a mere idea of the position of the time delay as it shows dynamics in both directions. The dynamics on the left side correspond to THG being the pump, while the dynamics on the right side correspond to THG being the probe. As no dynamics on the right side are visible for 380 nm and 374 nm, it is concluded that the dynamics on the right side for 362 nm originate from dimers, in agreement with the conclusions about the monomer and dimer excitations in fig. 3.2a in the next chapter. [LBE:(a)06/07/2017,(b,c)22/06/2017]

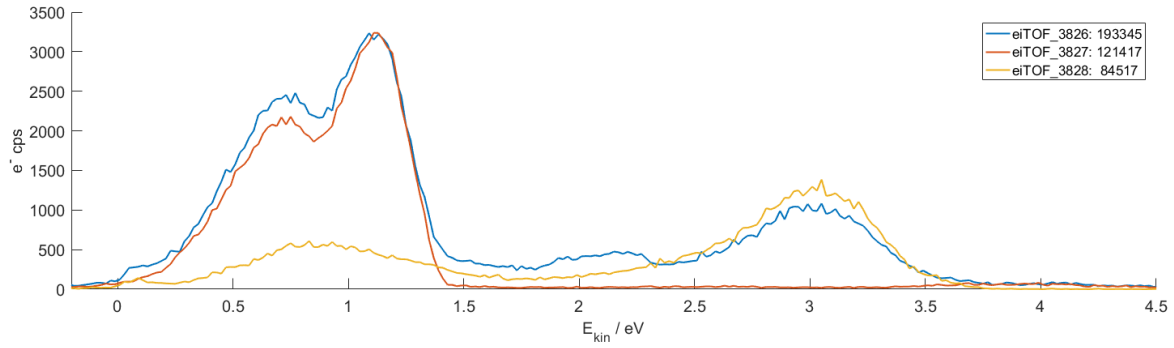

(a) Pump 362 nm, Probe 266 nm, time delay roughly 185 ps

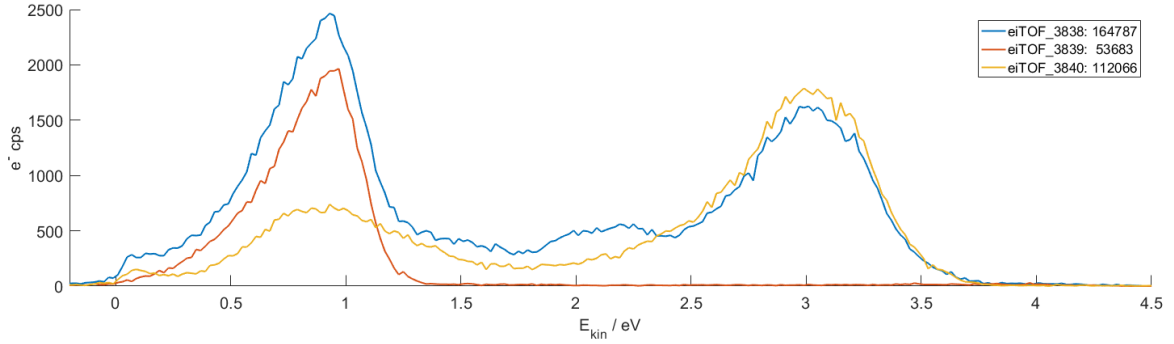

(b) Pump 374 nm, Probe 266 nm, time delay roughly 185 ps

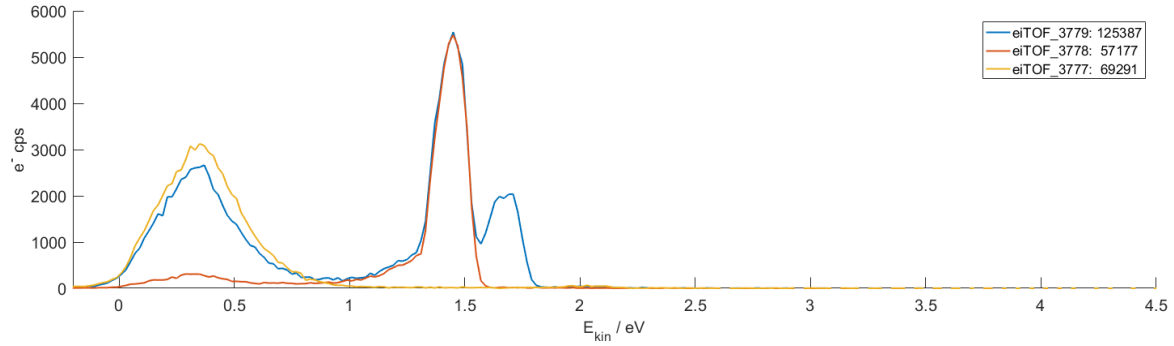

(c) Pump 306 nm, Probe 266 nm, time delay roughly 185 ps

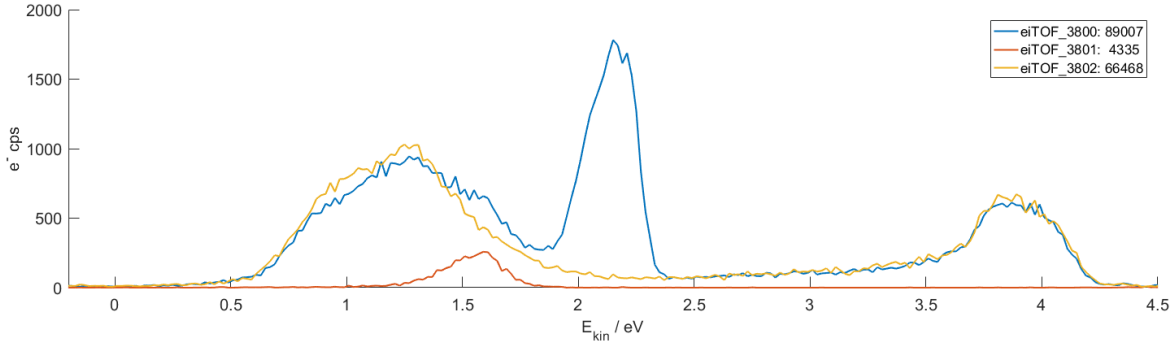

(d) Pump 266 nm, Probe 380 nm, time delay roughly 35 ps. The signal at 2.1 eV is suspected to be corresponding to the In $5s^2 5p \rightarrow 5s^2 7s$ transition.

Figure 5.3: Pump (yellow), Probe (red) and Pump-Probe (blue) PES recorded in various experiments with THG. Since no cross-correlation signal was found, the exact point of time zero could not be determined, still all conclusions hold. Note that the spectra have different calibrations, i.e. effective potentials at the ionisation spot. Further discussions can be found in the text. [LBE:(a,b)10/07/2017,(c)28/06/2017,(d)03/07/2017]

Appendix

A QMS hardware control class

Listing A.1: QMS hardware control class with basic functions

```
classdef QMS_balzers < handle
   % class to operate the QMS Balzers QMA 400 with SEV CP400

    properties
        serialConn
    end

    methods

        function obj = QMS_balzers
            % construtor: configure port and the serial parameters
            obj.serialConn = serial('COM2');
            set(obj.serialConn,'BaudRate',9600);
            set(obj.serialConn,'DataBits',8);
            set(obj.serialConn,'StopBits',1);
            set(obj.serialConn,'Parity','none');
            set(obj.serialConn,'Terminator',{'CR/LF','CR'});
            set(obj.serialConn,'Timeout',1);
            set(obj.serialConn,'FlowControl','none');

            fopen(obj.serialConn);
            communicate(obj, 'CMO, 1');
        end

        function delete(obj)
            obj.HV_switch(0);
            obj.current_switch(0);
            fclose(obj.serialConn);
        end

        function setmass(obj, mass)
            communicate(obj, ['MFM,', num2str(mass)]);
        end

        function mass = getmass(obj)
            mass = communicate(obj, 'MFM');
        end

        function setHV(obj, voltage)
            communicate(obj, ['DSE,', num2str(voltage)]);
        end

```

```
43          function setcurrent(obj, current)
44              communicate(obj, ['EMI,', num2str(current)]);
45          end
46
47          function setrodvoltages(obj, VO_array)
48              if nargin < 2
49                  VO_array_SEM_mode = [100,70,15.75,9,300,300,110,0,0];
50                  VO_array_pintest = [11,12,13,14,16,16,17,18,19];
51                  VO_array = VO_array_SEM_mode;
52              end
53              for k = 1:9
54                  communicate(obj, ['VO',num2str(k),', ', num2str(VO_array(k))]);
55                  pause(0.1);
56              end
57          end
58
59          function HV_switch(obj, string)
60              if string == 1
61                  communicate(obj, 'SEM,1');
62              elseif string == 0
63                  communicate(obj, 'SEM,0');
64              end
65          end
66
67          function current_switch(obj, string)
68              if string == 1
69                  communicate(obj, 'FIE,1');
70              elseif string == 0
71                  communicate(obj, 'FIE,0');
72              end
73          end
74
75          function [value] = communicate(obj, string)
76              % Send string
77              fprintf(obj.serialConn, string);
78              % Receive Acknowledgement
79              pause(0.1)
80              ack = sprintf(fgetl(obj.serialConn));
81              pause(0.1)
82              if 6 == ack;
83                  % Enquire and update value
84                  fprintf(obj.serialConn,['%s',char(5)]);
85                  value = sprintf('%s',fscanf(obj.serialConn));
86              else
87                  fprintf('Communication failed, no ACKnowledgement received')
88              end
89          end
90
91          function getinfo(obj)
92              % Talking ascii
93              communicate(obj, 'CMO, 1');
94              mass = communicate(obj, 'MFM');
95              SEV_voltage = communicate(obj, 'DSE');
96              emission_current = communicate(obj, 'EMI');
97              voltages = str2num([communicate(obj, 'VO1'),...
98                  communicate(obj, 'VO2'),...
99                  communicate(obj, 'VO3'),...
100                 communicate(obj, 'VO4'),...
101                 communicate(obj, 'VO5'),...
```

```
102                 communicate(obj, 'VO6'),...
103                 communicate(obj, 'VO7'),...
104                 communicate(obj, 'VO8'),...
105                 communicate(obj, 'VO9')])
106             vostring = {'VO1', 'VO2', 'VO3', 'VO4', 'VO5', 'VO6',...
107                 'VO7', 'VO8', 'VO9'};
108             Parameter = str2num([mass, SEV_voltage, emission_current]);
109             rowstring = {'Mass: ', 'SEV: ', 'Emission Current: '};
110             tab = table(Parameter,'RowNames',rowstring)
111             tab = table(voltages, 'RowNames', vostring)
112
113         end
114
115         function getstatus(obj)
116             communicate(obj, 'CMO, 1');
117             value = communicate(obj, 'ESQ');
118             value = strsplit(value,',');
119             value = str2double(value{1});
120
121                         statusstrings = {'Cycle halt / run',...
122                 'Mono/Multi',...
123                 'Emission off/on',...
124                 'SEM supply off/on',...
125                 'Waiting for external trigger',...
126                 'Setting halt /run',...
127                 'i-Undergr halt/run',...
128                 'Electrometer/emission-current',...
129                 'degas off / on',...
130                 'adjust off / on',...
131                 'adjust run',...
132                 '(not used1)',...
133                 '(not used2)',...
134                 '(not used3)',...
135                 'ringbuffer empty',...
136                 'ringbuffer overrun'};
137             statusbits = zeros(size(statusstrings));
138             help = fliplr(dec2bin(value));
139             value_bits = zeros(size(help));
140             for n = 1:length(value_bits)
141                 value_bits(n) = str2num(help(n));
142             end
143             statusbits(1:numel(value_bits)) = value_bits;
144             status = table(statusbits,'RowNames',statusstrings)
145         end
146     end
147 end
```

B Resistive heater - additional software and hardware documentation

B.1 FUG PSU remote control with the 12 pin LEMO plug

Beschreibung der externen Programmierung mit 12- poligem LEMO- Stecker (bis Baujahr 1992)

Schalter für Programmierung auf "ANALOG" stellen.
Frontseitige Bedienung außer Betrieb.
Programmierung nur über 12polige Buchse.

ACHTUNG!
Der Bezugspunkt "0V" (Pin 1) für alle externen Programmierspannungen ist unabhängig von der Ausgangspolarität galvanisch mit dem Ausgangsanschluß "0V" verbunden.
Bei aufgetrennter Verbindung "0V"-Erde müssen der Gegenstecker, das Kabel und alle Einrichtungen, die mit dem OV-Potential verbunden sind, die nötige Spannungsfestigkeit von 300V aufweisen. (Ausnahme: Option potentialfreie Programmierung).

Steckerbelegung:
1) 0V
2) +10 V Referenz
3) Ausgang EIN/AUS (Schalter nach 0V)
4) Strommonitor(O-10V)
5) Spannungsmonitor (0-10V)
6) Schleifer U-Pot. intern
7) Usoll (0-10V)
8) Schleifer I-Pot. intern
9) Regelzustandsanzeige Spannung
10) Regelzustandsanzeige Strom
11) Isoll(0-I0V)
12) frei

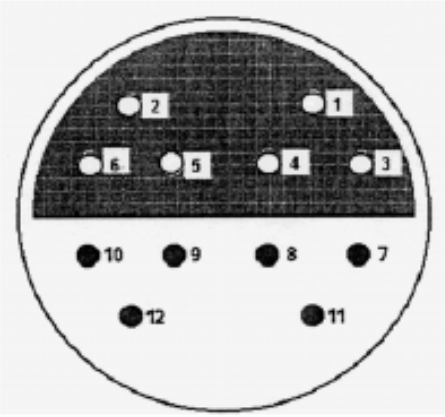

Lötseite Stecker

Hinweise zur Spannungs- bzw. Stromeinstellung:

Eine externe Spannungseinstellung erfordert unbedingt auch eine Beschaltung der Stromregelung. Wenn keine Limitierung unterhalb des Nennstromes gewünscht wird, den Pin 11 mit Pin 2 verbinden, alternativ bei Stromregelung eine Beschaltung von Pin 7 mit Pin 2. Ais Grenzwert können auch die Einstellungen der frontseitigen Potentiometer gewählt werden, dann alternativ eine Verbindung zu Pin 8 bzw. Pin 6 herstellen (Ausnahme: Option potentialfreie Programmierung).

ACHTUNG!
Nach dem Ausschalten des Gerätes wird eine eventuell noch vorhandene Ausgangsspannung nicht angezeigt.

B.2 Code examples: ADC-PC signal translation

Listing B.1: Example of the code for the communication between the ADC and the PC

```
% SET CURRENT, i2machine translates into a datagram (see fig. 2.6)
cmd = cmd.i2machine(I_set,cmd);
cmd_chksum = calc_chksum(cmd.set_i);
fwrite(obj,hex2dec(cmd_chksum),'uint8')
x = fread(obj,24);
if x(4) == 175; disp(['error: ',dec2hex(x(5)),dec2hex(x(6))]);
return ;end
% only hex digits 5 and 6 in the datagram contain signal
out.set_i = x;

% SET VOLTAGE, v2machine translates into a datagram (see fig. 2.6)
cmd = cmd.v2machine(U_max,cmd);
cmd_chksum = calc_chksum(cmd.set_v);
fwrite(obj,hex2dec(cmd_chksum),'uint8')
x = fread(obj,24);
if x(4) == 175; disp(['error: ',dec2hex(x(5)),dec2hex(x(6))]);
return ;end
% only hex digits 5 and 6 in the datagram contain signal
out.set_u = x;

% READ CURRENT
cmd_chksum = calc_chksum(cmd.get_i);
fwrite(obj,hex2dec(cmd_chksum),'uint8')
x = fread(obj,24);
if x(4) == 175; disp(['error: ',dec2hex(x(5)),dec2hex(x(6))]);
return ;end
% only hex digits 5 and 6 in the datagram contain signal
out.get_i = x;

% TRANSLATE CURRENT
hex_out = dec2hex(out.get_i);
hex_value = [hex_out(5,:),hex_out(5,:)];
dec_value = hex2dec(hex_value);
I_act = dec_value/15565*120;

% GET VOLTAGE
cmd_chksum = calc_chksum(cmd.get_v);
fwrite(obj,hex2dec(cmd_chksum),'uint8')
x = fread(obj,24);
if x(4) == 175; disp(['error: ',dec2hex(x(5)),dec2hex(x(6))]);
return ;end
% only hex digits 5 and 6 in the datagram contain signal
out.get_u = x;

% TRANSLATE VOLTAGE
hex_out = dec2hex(out.get_u);
hex_value = [hex_out(5,:),hex_out(6,:)];
dec_value = hex2dec(hex_value);
U_act = dec_value/15590*20;
```

Listing B.2: Example of the script to read the parameters from the ADC needed for the communication outlined in lst. B.1

```
cmd_chksum = calc_chksum(cmd.get_max);
fwrite(obj,hex2dec(cmd_chksum),'uint8');
x = fread(obj,24);
hex_out = dec2hex(x);
max_hex_valueUsoll= [hex_out(5,:), hex_out(6,:)];
max_hex_valueIsoll= [hex_out(7,:), hex_out(8,:)];
max_hex_valueUmon= [hex_out(9,:), hex_out(10,:)];
max_hex_valueImon= [hex_out(11,:), hex_out(12,:)];
max_dec_valueUsoll = hex2dec(max_hex_valueUsoll);
max_dec_valueIsoll = hex2dec(max_hex_valueIsoll);
max_dec_valueUmon = hex2dec(max_hex_valueUmon);
max_dec_valueImon = hex2dec(max_hex_valueImon);
```

B.3 ADC datagram syntax and command & reply lists

The syntax of the data types varies from language to language and has to be adapted acoordingly.
Explanation of the elements:

uint uiHeader = unsigned integer (2 Bytes), header word, always 0xAA55

uchar ucIDnumber = unsigned char (1 Byte), ID number of the UTA
The ID number should be set at least once, it is stored inside the UTA and has to be put into the structure, else any datagram containing a different ID than the one assigned to the interface will be ignored.

uchar ucCommand = unsigned char (1 Byte), contains the command (hex byte, see table)

char ucDatafield[18] = char (18 Bytes), contains parameters or ASCII characters for the related command (see table)

uint uiChecksum = unsigned integer (2 Bytes), checksum of the first 22 Byte of the datagram, serves for a simple security of the data transfer and is calculated as follows:
build a total sum of the first 22 bytes (results in a word), complement this and put this word as the checksum into the last two bytes of the datagram.

Figure of the datagram:

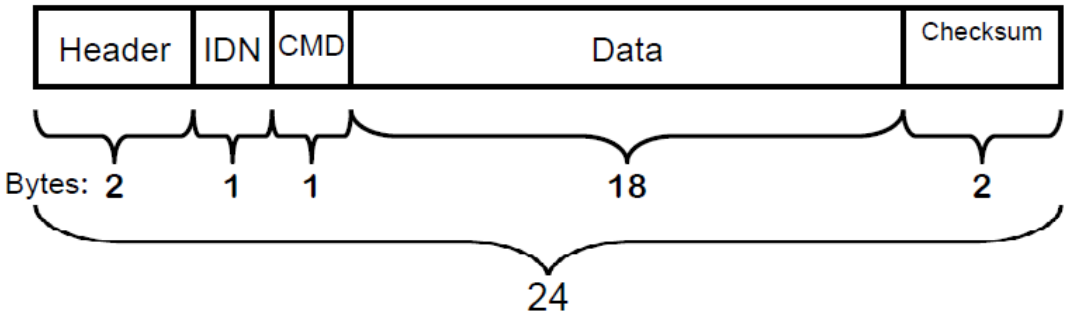

Figure B.1: Explanation of the datagram used to communicate [23]

datagram format sent by PC (command to UTA)

name	hex	header	id	command	value1		value2																check sum	notes
SetVoltage	1F	AA55	xx	1F	xx	xx	00	00	00	00	00	00	00	00	00	00	00	00	00	00	00	00	xxxx	value1 ranges from 0x0000 to 0xffff
GetVoltage	2F	AA55	xx	2F	00	00	00	00	00	00	00	00	00	00	00	00	00	00	00	00	00	00	xxxx	
SetCurrent	3F	AA55	xx	3F	xx	xx	00	00	00	00	00	00	00	00	00	00	00	00	00	00	00	00	xxxx	value1 ranges from 0x0000 to 0xffff
GetCurrent	4F	AA55	xx	4F	00	00	00	00	00	00	00	00	00	00	00	00	00	00	00	00	00	00	xxxx	
SetStatus	5F	AA55	xx	5F	xx	00	00	00	00	00	00	00	00	00	00	00	00	00	00	00	00	00	xxxx	value1 ranges from 0x00 to 0xff
GetStatus	6F	AA55	xx	6F	00	00	00	00	00	00	00	00	00	00	00	00	00	00	00	00	00	00	xxxx	
SetIDString	7F	AA55	xx	7F	xx	xx	xx	xx	xx	xx	xx	xx	xx	xx	xx	xx	xx	xx	xx	xx	xx	xx	xxxx	value1 & value2 MUST contain characters
GetIDString	8F	AA55	xx	8F	00	00	00	00	00	00	00	00	00	00	00	00	00	00	00	00	00	00	xxxx	
Echo	9F	AA55	00	9F	00	00	00	00	00	00	00	00	00	00	00	00	00	00	00	00	00	00	xxxx	without ID
SetIDN	EF	AA55	00	EF	xx	00	00	00	00	00	00	00	00	00	00	00	00	00	00	00	00	00	xxxx	value1 ranges from 0x00 to 0xff
GetIDN	FF	AA55	00	FF	00	00	00	00	00	00	00	00	00	00	00	00	00	00	00	00	00	00	xxxx	without ID
GetMaxValues	48	AA55	xx	48	00	00	00	00	00	00	00	00	00	00	00	00	00	00	00	00	00	00	xxxx	
SetUserText	C8	AA55	xx	C8	xx	xx	xx	xx	xx	xx	xx	xx	xx	xx	xx	xx	xx	xx	xx	xx	xx	xx	xxxx	value1 & value2 MUST contain characters
GetUserText	D8	AA55	xx	D8	00	00	00	00	00	00	00	00	00	00	00	00	00	00	00	00	00	00	xxxx	
Reset	E8	AA55	xx	E8	00	00	00	00	00	00	00	00	00	00	00	00	00	00	00	00	00	00	xxxx	does not cause a reply, only resets the UTA

Error codes of the reply AF:

Hex	Meaning
0x0001:	check sum mismatch
0x0002:	id string empty
0x0003:	header mismatch
0x0004:	eeprom write error

Bit assignment for command SetStatus (5F):
Bit 7: Stby (output off/on), value 0x80
Bit 6: REM (remote control on/off), value 0x40
Attention! The bits can not be set seperately!

Figure B.2: ADC command list [23]

datagram format sent by UTA (answer to PC)

name	hex	header	id	command	value1		value2																check sum	notes
SetVoltage	1F	AA55	xx	1F	00	00	00	00	00	00	00	00	00	00	00	00	00	00	00	00	00	00	xxxx	
GetVoltage	2F	AA55	xx	2F	xx	xx	00	00	00	00	00	00	00	00	00	00	00	00	00	00	00	00	xxxx	
SetCurrent	3F	AA55	xx	3F	00	00	00	00	00	00	00	00	00	00	00	00	00	00	00	00	00	00	xxxx	
GetCurrent	4F	AA55	xx	4F	xx	xx	00	00	00	00	00	00	00	00	00	00	00	00	00	00	00	00	xxxx	
SetStatus	5F	AA55	xx	5F	00	00	00	00	00	00	00	00	00	00	00	00	00	00	00	00	00	00	xxxx	
GetStatus	6F	AA55	xx	6F	xx	00	00	00	00	00	00	00	00	00	00	00	00	00	00	00	00	00	xxxx	
SetIDString	7F	AA55	xx	7F	00	00	00	00	00	00	00	00	00	00	00	00	00	00	00	00	00	00	xxxx	
GetIDString	8F	AA55	xx	8F	xx	xx	xx	xx	xx	xx	xx	xx	xx	xx	xx	xx	xx	xx	xx	xx	xx	xx	xxxx	value2 contains characters
Echo	9F	AA55	xx	9F	9F	9F	00	00	00	00	00	00	00	00	00	00	00	00	00	00	00	00	xxxx	
Error	AF	AA55	xx	AF	xx	xx	00	00	00	00	00	00	00	00	00	00	00	00	00	00	00	00	xxxx	value1 contains error code
SetIDN	EF	AA55	xx	EF	00	00	00	00	00	00	00	00	00	00	00	00	00	00	00	00	00	00	xxxx	
GetIDN	FF	AA55	xx	FF	xx	00	00	00	00	00	00	00	00	00	00	00	00	00	00	00	00	00	xxxx	
GetMaxValues	48	AA55	xx	48	aa	aa	bb	bb	cc	cc	dd	dd	00	00	00	00	00	00	00	00	00	00	xxxx	see legend
SetUserText	C8	AA55	xx	C8	00	00	00	00	00	00	00	00	00	00	00	00	00	00	00	00	00	00	xxxx	
GetUserText	D8	AA55	xx	D8	xx	xx	xx	xx	xx	xx	xx	xx	xx	xx	xx	xx	xx	xx	xx	xx	xx	xx	xxxx	

Notes:

GetIDN is "broadcasted" to id number 00 since you can can't send this command to a certain id before one is given

Error (AF) is a only an answer, which may be caused by any command (instead of the expected answer)

Meaning of the bits of the returned byte of GetStatus corresponding to the inputs of the UTA

Bit	7	6	5	4	3	2	1	0
	Stby	Rem	CC/CV	Error		CP	OT	OVP

legend

a - voltage out (Uset)
b - current out (Iset)
c - voltage in (Umon)
d - current in (Imon)
xx - various

Figure B.3: ADC reply list [23]

C Characterisations

C.1 He_N beam diameter

Table C.1: He_N beam diameter measurement corresponding to fig. 2.18. The result is a diameter of 2-3 mm. The experimental conditions were a stagnation pressure of 40 bar, nozzle temperature of 15 K, the temperature resistively measured was 700°C, 395 nm wavelength achieved with a 5 mm LBO crystal. The laser power was held at 90 mW with a focus diameter (FWHM from beam profiler) of $(70 \pm 10)\ \mu m$. In this early setup, no separation of the second harmonic from the residual fundamental has been conducted. The measurement points were limited to the displayed z-positions by the repeller geometry. [LBE:03/04/2017]
z_{lbp}...laser beam position in z-direction (mm)
z_{rep}...repeller position in z-direction (mm)
yield...total electron yield (counts per 10 seconds) with He-beam enabled
eff. bg. ...total electron yield (counts per 10 seconds) due to effusive beam background

z_{lbp} / mm	z_{rep} / mm	yield / cp10s	eff. bg. / cp10s
-3.45	-5.45	3110	465
-4.00	-6.00	2359	349
-4.45	-6.45	5819	611
-5.00	-7.00	3858	506
-5.45	-7.45	4535	510
-6.45	-8.45	2966	403
-7.45	-9.45	1631	261
-8.45	-10.45	1311	245
-9.45	-11.45	347	98

C.2 Pickup statistics

Table C.2: Total electron yield with respect to variation of the pickup temperature. The effect of droplet destruction as discussed in sec. 2.9.2 can be observed via the ratio of $He_N In$ electrons to effusive background electrons as well as the dropping number of He_2 observed in the QMS. The experimental conditions were a stagnation pressure of 40 bar, nozzle temperature of 17 K, 395 nm wavelength with a 5 mm LBO crystal. The laser power was held at 140 mW with a focus diameter (FWHM as measured with the beam profiler) of $(70 \pm 10)\ \mu m$. In this early setup, no separation of the second harmonic from the residual fundamental has been conducted. A graphical depiction of this table can be found in fig. 2.19 [LBE:04/04/2017]
T_{TC}...pickup temperature as measured with the thermocouple (°C)
yield...total electron yield (counts per 10 seconds) with He-beam enabled
eff. bg. ...total electron yield (counts per 10 seconds) due to effusive beam background
8u...signal of He_2 (8 amu) as measured with the QMS in Faraday mode (nA)

T_{TC} / °C	yield / cp10s	eff. bg. / cp10s	8u / nA
571	368	120	
575	490	120	
580	551	151	
585	754	234	
590	926	231	
595	1017	277	
600	1373	361	
605	1735	479	
610	2406	676	
615	3012	789	
620	3959	1114	
625	4816	1356	0.20
630	5884	1687	
635	7654	2300	
640	8998	2633	0.20
645	11673	4023	0.20
650	13742	4836	
655	17552	7220	
660	19400	8022	0.19
665	23056	10965	0.15
670	25610	12889	
675	29316	15638	0.10
680	33357	21133	0.10
685	39016	25676	0.06
690	42950	30798	0.05
695	49303	39158	0.04
700	53147	43168	0.03
710	65855	58800	

D Classical molecular dynamics script

Listing D.1: Classical molecular dynamics script

```
% PARAMETERS
% Physical constants
J2cm = 5.03445e22;
amu = 1.66053886e-27;
mass_He = 4.002602;
mass_In = 114.818;
reduced_mass = ((4000*mass_He*mass_In)/(4000*mass_He+mass_In))*amu;
sig_calc = 172.5074719;
sig_exp = 550./(2*sqrt(2*log(2)));
sig = sqrt(sig_calc^2+sig_exp^2);

% Physical parameters
kbT = 0.25716/1;% 0.37 K in cm^-1
mu =-28.1;  % chemical potential
samplesize = 100;
v_landau =   56e-2; % Landau speed
v_start = randn([1,samplesize]) * v_landau /1 ; % Initial velocity
timestepsize = 1e-0;
He_density_cutoff = 36; % Defines size of droplet
pot_cutoff = 100; % Defines whether particles is free or bound
critical_radius = pot_cutoff;
% Ionisation time: timedelay until ionisation after excitation
ionisation_time = ...
    [5,10,20,[30:2:150],160,170,180,190,200]/timestepsize;
sampling_subset = @(radius) radius >= 0 & radius < 25;


% Numerical parameters
numberoftimesteps_ion = 100/timestepsize;
hLength =1;
radius_datapointnumber = 100;
spacequantum_MDdiff = .05;
E_steps_pdf = 20;
L_steps_pdf = 200;

% Plot parameters
markersize = 10;


% LOAD & CUBIC SPLINE INTERPOLATE POTENTIAL
dataV = importdata('holding_potential_augcc.txt');
dataV = dataV.data;
pot_ground = real(dataV(:,2));
pot_ground = [pot_ground; zeros(26,1)];
dataV = importdata('holding_potential.txt');
dataV = dataV.data;
pot_ion = real(dataV(:,4));
radius_o = real(dataV(:,1));
pot_exc = real(dataV(:,3));
%pot_exc(1:9) = pot_exc(1:9) + (max(pot_exc)-pot_exc(1:9))*1.1;


% INTERPOLATE POTENTIALS LINEARLY AND CALCULATE FORCES
pot_ground = pot_ground - pot_ground(end);
pot_exc = pot_exc-pot_exc(end);
```

```
pot_ion = pot_ion-pot_ion(end);

radius = [1:max(radius_o)/radius_datapointnumber:48];
pot_ground_interp1 = ...
    ppval(interp1(radius_o, pot_ground, 'linear','pp'), radius);

pot_exc_interp0 = interp1(radius_o, pot_exc, 'linear','pp');
pot_exc_interp1 = @(radius) ppval(pot_exc_interp0, radius);

pot_ion_interp0 = interp1(radius_o, pot_ion, 'linear', 'pp');
pot_ion_interp1 = @(radius) ppval(pot_ion_interp0, radius);

xforce_atom_p = @(radius) pot_exc_interp1(radius)...
     - pot_exc_interp1(radius+spacequantum_MDdiff);
xforce_atom_pp = interp1(radius, xforce_atom_p(radius), 'linear','pp');
Xcoef = xforce_atom_pp.coefs;
Xlevel = Xcoef(:,2); Xlevel = [Xlevel; 0];
xforce_atom = @(current_position)...
    Xlevel(find(abs(current_position-radius)<0.25));

yforce_ion_p = @(radius) pot_ion_interp1(radius) - ...
    pot_ion_interp1(radius+spacequantum_MDdiff);
yforce_ion_pp = interp1(radius, yforce_ion_p(radius), 'linear','pp');
Ycoef = yforce_ion_pp.coefs;
Ylevel = Ycoef(:,2); Ylevel = [Ylevel; 0];
yforce_ion = @(current_position)...
    Ylevel(find(abs(current_position-radius)<0.25));

if true
    % Plot empirical and fitted ion potential
    figure;
    plot(radius_o, pot_ion); hold on
    plot(radius,pot_ion_interp1(radius), 'r');

    % Plot atom and ion forces
    figure;
    plot(radius, xforce_atom(radius)); hold on
    plot(radius, yforce_ion(radius), 'r');

    % Plot atom ground and excited state as well as ion ground state
    figure;
    plot(radius_o, pot_ground); hold on
    plot(radius, pot_ground_interp1); hold on
    plot(radius, pot_exc_interp1(radius), 'r');
    plot(radius, pot_ion_interp1(radius), 'k');

    % Plot forces
    figure;
    plot(radius, Xlevel); hold on
    plot(radius, Ylevel,'r');
end


% CALCULATE CLASSICAL PDFs
if true
    total_prob = zeros(size(radius(sampling_subset(radius))));
    norm = 0;
    V_min = min(pot_ground_interp1);
    V_min = pot_ground(1);
```

```
115     r_min = 0; radius(pot_ground_interp1==V_min);
116     pot = pot_ground_interp1;
117
118     % Integrate wrt energy
119     for E = linspace(V_min,0,E_steps_pdf)
120         L_max = sqrt( (E-V_min)/J2cm*2*reduced_mass*(r_min*1e10)^2);
121         % Integrate wrt angular momentum
122         for L = linspace(0,L_max,L_steps_pdf)
123             v_squared = 1.* ((E-pot(sampling_subset(radius)))- L.^2./...
124                 (2.*reduced_mass.*(radius(sampling_subset(radius)).....
125                     *1e10).^2).*J2cm);
126             prob = radius(sampling_subset(radius)).^2...
127             .*(1./ sqrt(abs(v_squared)+1e-60));
128             prob = prob./(sum(prob+0));
129             %boltz_factor =  exp(-(E-mu).^2/(2*sig^2)).*exp(-(L.^2./...
130                 %(2*reduced_mass*(radius(sampling_subset(radius))*1e10)
131                     .^2*J2cm)/(kbT)));
132             boltz_factor =  exp(-(E-mu)./(kbT))...
133                 .*exp(-(L.^2./(2*reduced_mass*(radius(sampling_subset(...
134                     radius))*1e10).^2)*J2cm/(kbT)));
135             total_prob = total_prob + prob.*boltz_factor;
136             norm = norm + boltz_factor;
137         end
138     end
139     total_prob = total_prob ./ norm;
140
141     % SAMPLING
142     if true
143       % Defining length of bins for histogram
144         xmin = 0; xmax = max(radius(sampling_subset(radius)));
145         hVector = [xmin:hLength:xmax];
146         norm = hLength * samplesize;
147         radius_norm = radius;
148         p = total_prob;
149         xrand = discretesample(p, samplesize);
150         [particle_distribution, center] = hist(xrand, hVector);
151         particle_distribution=particle_distribution/(samplesize*hLength);
152
153         if true
154             % Plot probability density function and histogram
155             figure; bar(center, particle_distribution); hold on
156             plot(radius(sampling_subset(radius)), total_prob,'r');
157         end
158     end
159 end
160
161 energy = [];
162 if true
163
164     % ---------INITIALISATION-----------------------------------------------
165     ejected_ions = [];
166     ejected_atoms = [];
167     findindex_max = find(radius==max(radius));
168
169     X = xrand;
170     %X = [1:30];
171     %v_start = randn(size(X)) * v_landau *0;
172     %v_start = ones(size(X))*v_landau;
173     vx = v_start.*ones(size(X));
```

```
174
175     xhelp = X(end,:);
176     vhelp = vx;
177     findindex = zeros(size(xhelp));
178     % Find start position index of each particle
179     for w = 1:length(xhelp)
180         findindex_help =...
181          (find(abs(xhelp(w)-radius)<(max(radius)/radius_datapointnumber)/0.5));
182         findindex(w) = findindex_help(1);
183     end
184
185     %-----------------------------------------
186     %------ LEAPFROG-ALGORITHM ------------------------------------------------
187     % ------ LEAPFROG FOR THE ATOM ---------------------------------------------
188     numberoftimesteps_atom = max(ionisation_time);
189     for t = timestepsize:timestepsize:numberoftimesteps_atom*timestepsize
190
191         energy = [energy, vhelp.^2 + pot_exc_interp1(xhelp)];
192
193         % Employ the leapfrog calculation of force, velocity and position
194         xhelp = X(end,:);
195         xforce_help = Xlevel(findindex);
196         vhelp =  vx(end,:)' + timestepsize/2*xforce_help;
197       % Invoke v_Landau constraint inside the droplet:
198         vhelp(xhelp<=He_density_cutoff) =...
199          min(vhelp(xhelp<=He_density_cutoff), v_landau);
200         vhelp = vhelp';
201         vx = [vx;vhelp];
202         X = [X; xhelp + timestepsize*vhelp];
203
204         % Implement radial symmetry
205         L1 = X<0;
206         vx(L1) = -vx(L1);
207         X(L1) = -X(L1);
208
209         % From the new positions, find the new force acting upon the
210         % particle. To do this, the latest position index change is
211         % calculated, added to the latest position index and the
212         % corresponding value from the force list is chosen
213         indexstep = (X(end,:) - X(end-1,:));
214         indexstep = indexstep/(max(radius)/radius_datapointnumber) ...
215             -  rem(indexstep/(max(radius)/radius_datapointnumber),...
216                max(radius)/radius_datapointnumber);
217         indexstep = indexstep/(max(radius)/radius_datapointnumber);
218         findindex = findindex + indexstep;
219         findindex(findindex<0) = -findindex(findindex<0);
220         findindex(findindex>findindex_max) = findindex_max;
221         findindex(findindex == 0) = 1;
222
223         % Count how many atoms are outside the dropled
224         ejected_atoms = [ejected_atoms, sum(X(end,:)> He_density_cutoff )];
225
226         % Enter inner loop and calculate ion trajectories starting from the
227         % latest atom position. This loop again is a leapfrog algorithm of
228         % the very same structure as for the atom
229         if any(t==ionisation_time)
230             t
231             % ---------- LEAPFROG FOR THE ION ----------------
232
```

```
233             % 'Initialisation' done by taking the latest value of the atom.
234             Y = X(end,:);
235             vy = vx(end,:);
236             findindex_ion = findindex;
237             for t_ion =...
238                 timestepsize:timestepsize:numberoftimesteps_ion*timestepsize
239                 yhelp = Y(end,:);
240                 yforce_help = Ylevel(findindex_ion);
241                 vhelp =  vy(end,:)' + timestepsize/2*yforce_help;
242                 vhelp(yhelp<=He_density_cutoff) =...
243                    min(vhelp(yhelp<=He_density_cutoff), v_landau);
244                 vhelp = vhelp';
245                 vy = [vy;vhelp];
246                 Y = [Y; yhelp + timestepsize*vhelp];
247
248                 L1 = Y<0;
249                 vy(L1) = -vy(L1);
250                 Y(L1) = -Y(L1);
251
252                 indexstep = (Y(end,:) - Y(end-1,:));
253                 indexstep = ...
254                   indexstep/(max(radius)/radius_datapointnumber) ...
255                     -  rem(indexstep/(max(radius)/radius_datapointnumber),...
256                      max(radius)/radius_datapointnumber);
257                 indexstep = indexstep/(max(radius)/radius_datapointnumber);
258                 findindex_ion = findindex_ion + indexstep;
259                 findindex_ion(findindex_ion<0) =...
260                    -findindex_ion(findindex_ion<0);
261                 findindex_ion = round(findindex_ion);
262                 findindex_ion(findindex_ion>findindex_max) = findindex_max;
263                 findindex_ion(findindex_ion == 0) = 1;
264             end
265
266             % Count how many ions are outside the dropled
267             ejected_ions = [ejected_ions, sum(Y(end,:)> pot_cutoff)];
268
269             if true
270                 figure; % Plot trajectories
271                 for k = 1:1:length(X)-1
272                     plot(X(:,k)', 0:timestepsize:t ); hold on
273                     plot(Y(:,k)',t*timestepsize+...
274                       [0:timestepsize:numberoftimesteps_ion*...
275                          timestepsize],'r');
276                 end
277                 xlabel('position r / Angstroem');
278                 ylabel('time / ps');
279                 %xlim([0,critical_radius*1.5]);
280                 plot([critical_radius,critical_radius],...
281                 [0,timestepsize*numberoftimesteps_atom], 'g');
282                 legend(['ionisation time = ', num2str(t)])
283             end
284
285             if true
286                 figure; % Plot trajectories
287                 for k = 1:1:length(X)-1
288                     plot(X(:,k), vx(:,k)); hold on
289                     plot(Y(:,k), vy(:,k),'r');
290                     plot([critical_radius,critical_radius],...
```

```
                end
                ylabel('velocity  [ps / Angstroem]');
                xlabel('position r / Angstroem');
                legend(['ionisation time = ', num2str(t)])
            end
        end
    end
end
% ---------- END TRAJECTORY CALCULATIONS ----------

% ---------- COMPARISON TO EXPERIMENT ----------
if true

    % Load experimental data of ion timescan and perform fit

    % Custom made data analysis script, may make use of
    % another custom made function called 'indium_peakshift_v2.m'
    afit = ion_yield_dopant_ejection_timescan;
    hold on

    ejected_ions = (ejected_ions)/max(ejected_ions);
    ejected_ions = [zeros(1,20),ejected_ions];

    ejected_atoms = (ejected_atoms)/max(ejected_atoms);
    %ejected_atoms = [zeros(1,20),ejected_atoms];

    ionisation_time = [linspace(-30,min(ionisation_time),20),ionisation_time];
    timedelay_ions = ionisation_time*timestepsize;
    timedelay_atoms = timestepsize:timestepsize:...
      numberoftimesteps_atom*timestepsize;

    % DATA FIT ROUTINE (from lab)
    erfc_rise = @(a,t) a(1)+a(2).*erfc((a(3)-t)./a(4));
    exp_rise = @(a,t) a(1)+a(2)*(1-exp(-(t-a(3))/a(4))).*heaviside(t-a(3));
    bfit_erfc = [113.58, 991.413, 65.7853, 37.2159 ]
    cfit_erfc = [113.58, 991.413, 65.7853, 37.2159 ]
    fit_func = @(a,t) exp_rise(a,t);

    [bfit,R,J,~] = nlinfit(timedelay_ions,ejected_ions,fit_func,bfit_erfc);
    [cfit,~,~,~] = nlinfit(timedelay_atoms,ejected_atoms,fit_func,cfit_erfc);

    bfit
    cfit

    plot(timedelay_ions, ejected_ions,'b.'); hold on
    plot(timedelay_ions,fit_func(bfit,timedelay_ions)/...
      max(fit_func(bfit,timedelay_ions)),'b','LineWidth',2);
    plot(timedelay_atoms, ejected_atoms, 'k.');
    plot(timedelay_atoms,fit_func(cfit,timedelay_atoms)/...
      max(fit_func(bfit,timedelay_atoms)),'k','LineWidth',2);
    xlabel('timedelay / ps');
    ylabel('yield');
    legend('Exp. Ion yield',['Fit signal rise \tau = ',...
      num2str(afit(4)),' ps'],'Simulation Ions', ['Sim fit \tau = ',...
          num2str(bfit(4))], 'Simulation Atoms',...
           ['Sim fit \tau = ', num2str(cfit(4))],...
             'Location','SouthEast')
end
```

Bibliography

[1] J. P. Toennies and A. F. Vilesov. Superfluid helium droplets: A uniquely cold nanomatrix for molecules and molecular complexes. *Angewandte Chemie International Edition*, 43(20):2622, 2004.

[2] C. Callegari and W. E. Ernst. *Handbook of High- Resolution Spectroscopy*, volume 3. John Wiley and Sons, Chichester, 2011.

[3] M. Hartmann, R. Miller, J. Toennies, and A. Vilesov. Rotationally resolved spectroscopy of SF6 in liquid helium clusters: A molecular probe of cluster temperature. *Physical Review Letters*, 75(8):1566, 1995.

[4] Zewail, Ahmed H. The new age of structural dynamics. *Acta Crystallographica Section A: Foundations of Crystallography*, 66(2):135–136, 2010.

[5] Koch, Markus and Auböck, Gerald and Callegari, Carlo and Ernst, Wolfgang E. Coherent spin manipulation and ESR on superfluid helium nanodroplets. *Physical Review Letters*, 103(3):035302–1–4, July 2009.

[6] M. Mudrich and F. Stienkemeier. Photoionisaton of pure and doped helium nanodroplets. *International Reviews in Physical Chemistry*, 33(3):301–339, July 2014.

[7] F. Stienkemeier, F. Meier, A. Hägele, H. O. Lutz, E. Schreiber, C. P. Schulz, and I. V. Hertel. Coherence and relaxation in potassium-doped helium droplets studied by femtosecond pump-probe spectroscopy. *Physical Review Letters*, 83(12):2320–2323, 1999.

[8] Auböck, Gerald and Nagl, Johann and Callegari, Carlo and Ernst, Wolfgang E. Electron spin pumping of Rb atoms on He nanodroplets via nondestructive optical excitation. *Physical Review Letters*, 101(3):035301 1–4, Jul 2008.

[9] Theisen, Moritz and Lackner, Florian and Ernst, Wolfgang E. Cs atoms on helium nanodroplets and the immersion of Cs^+ into the nanodroplet. *The Journal of Chemical Physics*, 135(7):074306, 2011.

[10] von Vangerow, Johannes and Coppens, François and Leal, Antonio and Pi, Martí and Barranco, Manuel and Halberstadt, Nadine and Stienkemeier, Frank and Mudrich, Marcel. Imaging excited-state dynamics of doped He nanodroplets in real-time. *The Journal of Physical Chemistry Letters*, 8(1):307–312, 2017. PMID: 27996261.

[11] Steven L. Fiedler, David Mateo, Tatevik Aleksanyan, and Jussi Eloranta. Theoretical modeling of ion mobility in superfluid ^{4}He. *Physical Review B*, 86(14):144522, Oct 2012.

[12] Evgeniy Loginov and Marcel Drabbels. Excited state dynamics of Ag atoms in helium nanodroplets. *The Journal of Physical Chemistry A*, 111(31):7504–7515, 2007. PMID: 17569515.

[13] Friedrich Lindebner, Andreas Kautsch, Markus Koch, and Wolfgang E. Ernst. Laser ionization and spectroscopy of Cu in superfluid helium nanodroplets. *International Journal of Mass Spectrometry*, 365-366(0):255–259, 2014.

[14] Alberto Hernando, Manuel Barranco, Ricardo Mayol, Martí Pi, and Francesco Ancilotto. Density functional theory of the structure of magnesium-doped helium nanodroplets. *Physical Review B*, 78(18):184515, Nov 2008.

[15] Michael P. Ziemkiewicz, Daniel M. Neumark, and Oliver Gessner. Ultrafast electronic dynamics in helium nanodroplets. *International Reviews in Physical Chemistry*, 34(2):239–267, April 2015.

[16] Albert Stolow, Arthur E Bragg, and Daniel M. Neumark. Femtosecond time-resolved photoelectron spectroscopy. *Chemical reviews*, 104(4):1719–1758, 2004.

[17] IV Hertel and W Radloff. Ultrafast dynamics in isolated molecules and molecular clusters. *Reports on Progress in Physics*, 69(6):1897, 2006.

[18] Bernhard Thaler. Ultrafast molecular photodissociation dynamics studied with single-pulse femtosecond photoelectron-photoion-coincidence spectroscopy. Master's thesis, TU Graz, 2017.

[19] Stefan Cesnik. Femtosecond Dynamics in Isolated Molecules. Master's thesis, TU Graz, 2018.

[20] Paul Maierhofer. Femtosecond Photodissociation Dynamics in Molecules studied by Time-Resolved Phtoelectron-Photoion-Coincidence Spectroscopy. Master's thesis, TU Graz, 2016.

[21] Markus Bainschab. Multiphoton Ionization Channels in Molecules Investigated by Photoelectron-Photoion-Coincidence Spectroscopy. Master's thesis, TU Graz, 2016.

[22] Markus Koch. *Magnetic Resonance Spectroscopy of Single Alkali-Metal Atoms Isolated in Superfluid Helium Nanodroplets*. PhD thesis, TU Graz, 2009.

[23] EA Elektroautomatik GmbH. *User's guide UTA12 Interface*, 20/01/2011 edition. `http://www.elektroautomatik.de/files/eautomatik/treiber/uta12/33100209_EN.pdf`.

[24] O. Kubaschewsky, E. L. L. Evans and C. B. Alcock,. *Metallurgical Thermochemistry*. Pergamon Press, Oxford U.K, 1967.

[25] Balzers Instruments (Pfeiffer Vakuum GmbH). *QMA 400-410-430 operating manual*, bg800453be (0001) edition.

[26] Balzers Instruments (Pfeiffer Vakuum GmbH). *QMG 422 operating manual*, bg800451bd (9801) edition.

[27] Balzers Instruments (Pfeiffer Vakuum GmbH). *QMG 422 communication protocol*, bg805986bd (0108) edition.

[28] Balzers Instruments AG. *Balzers Quadstar 422 user manual*, 6th, bg 803222bd/a (9801) edition.

[29] Florian Lackner. *Rydberg States of Alkali-Metal Atoms on Superfluid Helium Nanodroplets*. PhD thesis, TU Graz, 2012.

[30] Pascal Heim. Analysis of molecular Rydberg state relaxation dynamcs applying Bayesian probability theory. Master's thesis, TU Graz, 2017.

[31] Ralf Meyer, Bernhard Thaler, Pascal Heim, Stefan Cesnik, Sascha Ranftl, Johann V. Pototschnig, Wolfgang E. Ernst, Markus Koch, and Andreas W. Hauser. Large amplitude oscillations in a superfluid confinement: Classical and quantum approaches. unpublished.

[32] H.-J. Werner, P. J. Knowles, G. Knizia, F. R. Manby, M. Schütz, P. Celani, T. Korona, R. Lindh, A. Mitrushenkov, G. Rauhut, K. R. Shamasundar, T. B. Adler, R. D. Amos, A. Bernhardsson, A. Berning, D. L. Cooper, M. J. O. Deegan, A. J. Dobbyn, F. Eckert, E. Goll, C. Hampel, A. Hesselmann, G. Hetzer, T. Hrenar, G. Jansen, C. Köppl, Y. Liu, A. W. Lloyd, R. A. Mata, A. J. May, S. J. McNicholas, W. Meyer, M. E. Mura, A. Nicklass, D. P. O'Neill, P. Palmieri, D. Peng, K. Pflüger, R. Pitzer, M. Reiher, T. Shiozaki, H. Stoll, A. J. Stone, R. Tarroni, T. Thorsteinsson, and M. Wang. Molpro, version 2012.1, a package of ab initio programs, 2012. see http://www.molpro.net.

[33] Bernhard Metz, Hermann Stoll, and Michael Dolg. Small-core multiconfiguration-dirac–hartree–fock-adjusted pseudopotentials for post-d main group elements: Application to Pbh and Pbo. *The Journal of Chemical Physics*, 113(7):2563–2569, Aug 2000.

[34] Dmitrij Rappoport and Filipp Furche. Property-optimized Gaussian basis sets for molecular response calculations. *The Journal of Chemical Physics*, 133(13):134105, Oct 2010.

[35] F. Dalfovo, A. Lastri, L. Pricaupenko, S. Stringari, and J. Treiner. Structural and dynamical properties of superfluid helium: A density-functional approach. *Physical Review B*, 52(2):1193–1209, Jul 1995.

[36] Francesco Ancilotto, Manuel Barranco, François Coppens, Jussi Eloranta, Nadine Halberstadt, Alberto Hernando, David Mateo, and Martí Pi. Density functional theory of doped superfluid liquid helium and nanodroplets. *International Reviews in Physical Chemistry*, 36(4):621–707, 2017.

[37] HG Evertz. Computer Simulations, `http://itp.tugraz.at/~{}evertz/Computersimulationen/cs.html`. 2009.

[38] Nils B. Brauer, Szymon Smolarek, Evgeniy Loginov, David Mateo, Alberto Hernando, Marti Pi, Manuel Barranco, Wybren J. Buma, and Marcel Drabbels. Critical landau velocity in helium nanodroplets. *Physical Review Letters*, 111(15):153002–1–5, 2013.

[39] Kevin K. Lehmann and Adriaan M. Dokter. Evaporative cooling of helium nanodroplets with angular momentum conservation. *Physical Review Letters*, 92(17):173401–1 – 173401–4, 2004.

Danksagung

Zum Finale meines Studiums der Physik, von der ich schon als Kind fasziniert war, sollte ich die Möglichkeit bekommen in einer waschechten Forschungsgruppe mitzuarbeiten, ja selbst zu forschen. Das letzte Jahr stellte damit alles in den Schatten, was ich mir an beruflichen Möglichkeiten bis dahin vorstellen konnte.

Dafür möchte ich mich zuallererst bei meinem Betreuer Ass.Prof. Dr. Markus Koch bedanken, auch für seine Wertschätzung, seinen inspirierenden Ehrgeiz und seine motivierenden Worte wenn die Laborgeister spuken, denn "wenn's einfach wär, dann hätt's schon wer gemacht". Aber am meisten danken möchte ich für sein Vertrauen. Ich habe es stets als Herausforderung, aber auch als Privileg und Auszeichnung verstanden, bei dir zu lernen und unter deiner Anleitung Experimente durchzuführen, die so noch nie ein Mensch gemacht hat. Das gibt mir heute das Selbstbewusstsein jede erdenkliche Karriere eines Physikers einzuschlagen.

Damit möchte ich mich bei Bernhard Thaler und Pascal Heim für die Einschulung im Labor bedanken. Ersterem möchte ich neben Stefan Cesnik, Leonhard Treiber und Gigi d'Agostino auch noch ganz besonders für die erfolgreiche Laborpartnerschaft danken. Die Arbeit mit euch hat wirklich Spaß gemacht und gemeinsam konnten wir fantastische Naturphänomene beobachten. Weiters möchte ich Miriam Meyer für das angenehme Klima im Büro sowie das Korrekturlesen dieser Arbeit danken .

Den Mitarbeitern vom Institut für Experimentalphysik möchte ich für die unkomplizierte und kollegiale Zusammenarbeit danken, sei es durch technischen, kulinarischen oder theoretischen Support. Damit möchte ich namentlich unseren Theoretikern Ralf Meyer, Johann Pototschnig und Ass. Prof. DDr. Andreas Hauser für die synergetische Zusammenarbeit danken. Ihre Beiträge waren von immenser Bedeutung für die Interpretation unserer Beobachtungen. Eines Tages wird die Welt eure sensationelle Arbeit verstehen und anerkennen.

Für die Möglichkeit am Institut für Experimentalphysik meine Masterarbeit zu verfassen, aber auch für die verständnis- und vertrauensvolle Zusammenarbeit in meiner Rolle als Studienvertreter, bedanke ich mich bei Dekan Univ. Prof. Dr. Wolfgang E. Ernst.

Meine langjährigen Studienkollegen, darunter Bernhard Thaler und Stefan Cesnik, sowie Arthur Fuchs, Florian Kappe, Andreas Jeindl und Lukas Hörmann möchte ich mittlerweile auch gute Freunde nennen. Ohne euch wäre mein Studium sicher nicht so erfolgreich und angenehm gewesen. Danke auch dafür, dass ihr mich immer wieder aus meinen Motivationslöchern gezogen habt.

Auch meinen Mitstreitern in der Basisgruppe und der Hochschülerschaft gilt mein Dank. Auf die vielen Weisen, wie wir den Studienalltag gestalten und die vielen Ideen, die wir gemeinsam verwirklichen konnten, und auf die unzähligen Freundschaften die dabei entstanden sind.

Danke auch meinem Mitbewohner Dominik Rabl für das friedvolle Zusammenleben und dass es in sechs Jahren Wohngemeinschaft keinen einzigen Streit gab.

Meinen Freunden in meiner Heimat Weinberg und meinen Feuerwehrkameraden danke ich für ihr Verständnis, ihre Loyalität und ihre Anerkennung.

Auf diesen Weg brachten mich nicht nur meine Förderer in meiner alten Schule, sondern auch mein Bruder René. Danke dafür, ich habe heute keine Zweifel mehr daran.

Danke für die wunderschönen Erlebnisse an die Menschen die ein Stück ihres Weges mit mir gemeinsam gingen.

Mein größter Dank gilt jedoch meiner Familie, meinen Großeltern, Onkel Gerald und Tante Anita, meinen Freunden aus Kindheitstagen Gabriel und Bernhard für ihre immerwährende Freundschaft, meinem Bruder René für die Inspiration, sein Vorbild, seinen Rat und seinen Rückhalt, und meinen Eltern Hans-Peter und Angelika, die es mir ermöglichten meinen Weg zu gehen, frei von Ängsten, mit voller Unterstützung
und bedingungsloser Liebe.

Graz, November 2017